ՀՀ ԳԱԱ Վ. ՀԱՄԲԱՐՁՈՒՄՅԱՆԻ ԱՆՎԱՆ ԲՅՈՒՐԱԿԱՆԻ
ԱՍՏՂԱԴԻՏԱՐԱՆ

ԽԱՉԱՏՐՅԱՆ ՄՀԵՐ ՀՐԱՉՅԱԻ

ՄԵՔԵՆԱՅԱԿԱՆ ՈՒՍՈՒՑՄԱՆ ԱԼԳՈՐԻԹՄՆԵՐԻ ԿԻՐԱՌՈՒՄ ԲԼԱԶԱՐՆԵՐԻ ԴԱՍԱԿԱՐԳՄԱՆ ԵՎ ԴՐԱՆՑ ՃԱՌԱԳԱՅԹՄԱՆ ՄՈԴԵԼԱՎՈՐՄԱՆ ՀԱՄԱՐ

Ատենախոսություն

Ա.03.02 - «Աստղաֆիզիկա, ռադիոաստղագիտություն» մասնագիտությամբ

Ֆիզիկամաթեմատիկական գիտությունների թեկնածուի գիտական աստիճանի համար

Գիտական ղեկավար՝
ֆ.մ.գ.դ. Նարեկ Սահակյան

ԵՐԵՎԱՆ-2026

BYURAKAN ASTROPHYSICAL OBSERVATORY AFTER V. AMBARTSUMIAN

MHER HRACHYA KHACHATRYAN

APPLICATION OF MACHINE LEARNING ALGORITHMS TO CLASSIFY BLAZARS AND MODEL THEIR RADIATION

DOCTORAL THESIS

For the degree of candidate in physical and mathematical sciences in the specialization A.03.02 – “Astrophysics, radioastronomy”

Supervisor:
Dr. Narek Sahakyan

Yerevan–2026

Table of Contents

INTRODUCTION

Recent progress in observational astronomy and astrophysics has transformed the way we study the Universe. Modern ground-based and space-based observatories provide data from radio to very-high-energy (VHE) γ-rays, while neutrino and gravitational-wave observatories provide information that is independent of electromagnetic observations. As a result, multiwavelength and multimessenger observations have become essential for understanding astrophysical objects and for having a deeper view of the processes taking place in them. Among these objects, Active Galactic Nuclei (AGNs) and, in particular, blazars occupy a special place because of their extreme luminosities, rapid variability, and broad-band non-thermal emission [1–3].

AGNs represent one of the most energetic and diverse classes of extragalactic objects. The modern view of these objects developed from early spectroscopic observations of unusually bright galactic centers which was connected with the discovery of quasars, revealing that the central engine of some galaxies can outshine the entire host galaxy. Today, AGNs are understood as compact regions powered by accretion onto supermassive black holes (SMBHs), producing enormous luminosities across the electromagnetic spectrum. Their emission can include both thermal and non-thermal components, and despite their observational diversity, most AGNs can be described within a unified framework consisting of a central black hole, an accretion disk, broad and narrow line regions, surrounding dusty material, and, in some cases, relativistic jets [1, 2, 4].

A primary method to classify AGNs is based on their radio emission, typically quantified by the ratio of radio to optical flux. Sources with a ratio above a threshold value (usually $R > 10$) are classified as radio-loud, while those below this limit are considered radio-quiet. Radio-quiet AGNs include Seyfert galaxies and quasars, whereas radio-loud systems comprise Fanaroff-Riley type I and II radio galaxies, as well as blazars. Only a small fraction (about 10%) of AGNs

are radio-loud. However, these sources are particularly important because a significant portion of their accretion power is transferred to relativistic, collimated jets that can carry energy to distances far beyond the central nucleus. These jets host highly energetic particles accelerated to near-light speeds, which interact with magnetic and radiation fields along the jet, producing strong non-thermal emission across the electromagnetic spectrum.

Another key classification depends on the orientation following the unified model [5]. In this framework, the observed properties of AGNs depend strongly on the viewing angle relative to the dusty torus and jet axis. When the system is observed close to the plane of the torus, the central engine and broad-line region (BLR) are obscured, leading to the classification of Seyfert II galaxies or narrow-line radio galaxies. At intermediate viewing angles, the BLR becomes visible, resulting in Seyfert I galaxies or broad-line radio galaxies. In radio-loud AGNs, the orientation of the jet introduces an additional changes: sources observed at large angles to the line of sight are identified as radio galaxies, while sources observed at small angles are classified as blazars. This orientation-driven picture, illustrated in Figure 1, explains why objects with broadly similar intrinsic structures can appear very different observationally, and why blazars occupy such a special place among AGNs [1, 4].

The observational features of blazars depend on the geometry of the emission region. When an emission region inside the relativistic jet moves with Lorentz factor Γ and it makes a small angle θ to the line of sight, its emission is strongly Doppler boosted, with a Doppler factor given by

$$\delta = \frac{1}{\Gamma(1 - \beta \cos\theta)}, \tag{0.1}$$

where $\beta = v/c$. For sufficiently small viewing angles, this boosting can dramatically enhance the observed flux, shorten apparent variability timescales, and cause the jet emission to dominate over the thermal radiation from the accretion flow. As a result, blazars appear as the most extreme class of

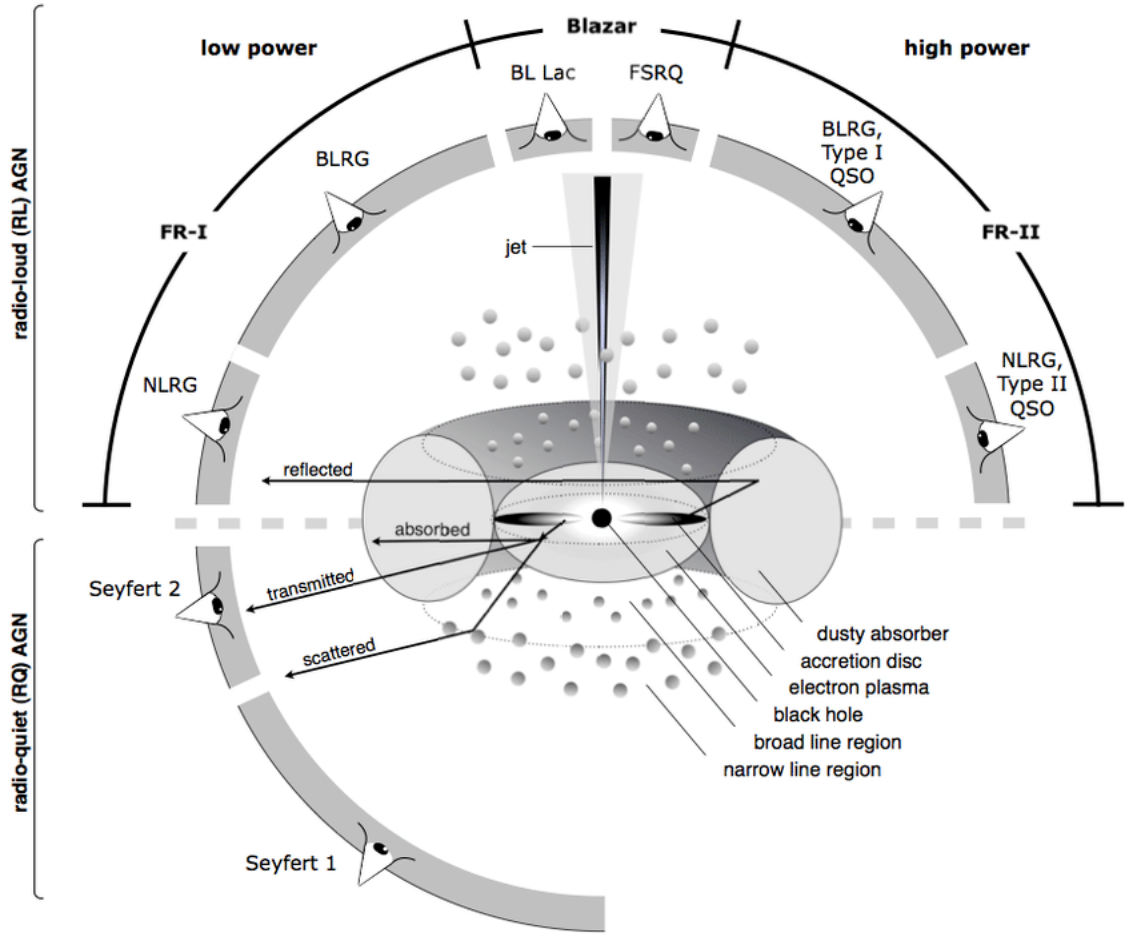

Figure 1: Standard orientation-based Unified model of AGN, showing the central supermassive black hole, accretion disk, broad-line region, dusty torus, narrow-line region, relativistic jet, and the dependence of the observed AGN class on the viewing angle. Adapted from [6].

AGNs, exhibiting exceptionally high apparent luminosities, rapid variability, and broad-band non-thermal spectra.

Blazars are scientifically important for several reasons. First, they probe physics near accreting SMBHs and inside relativistic jets, where particle acceleration, magnetized plasma dynamics, and radiative transfer operate under extreme conditions. Second, their emission extends over a very wide energy range, from radio frequencies to high-energy (HE; $E > 100$ MeV) and sometimes VHE ($E > 100$ GeV) γ-rays, which makes them natural targets for multiwavelength studies. Third, they often show strong and variable polarization, especially in radio and optical bands, indicating ordered magnetic fields and non-thermal radiation processes. Fourth, the shortest observed flares can occur on timescales of days, hours, and in some cases even minutes,

implying that at least part of the emission is produced in compact regions. Finally, blazars are now central objects in multimessenger astrophysics because some of them have been linked to high-energy neutrino events, which opened the possibility that relativistic jets may accelerate hadrons [7–9].

At the same time, blazars are rare objects. Present-day surveys identify only a few thousand confirmed or likely blazars, a very small number compared with the overall galaxy population of the observable Universe. This rarity is partly physical and partly observational: AGN to be identified as a blazar, should have relativistic jet viewed at a small angle, and such alignment is uncommon. In addition, reliable subclass identification often requires optical spectroscopy and coordinated multiwavelength information, both of which are expensive to obtain for large samples. As a result, even though blazars are dominant among the identified extragalactic populations in the HE γ-ray sky, many sources remain poorly characterized [10, 11].

The broad-band spectral energy distribution (SED) of a blazar usually shows two broad components. The low-energy component extends from radio to optical, ultraviolet, or X-ray bands and is commonly attributed to synchrotron radiation from relativistic electrons in the jet. The HE component extends from X-rays to HE and sometimes VHE γ-rays, but its origin is still debated. In leptonic models, this component is produced through inverse Compton scattering, either on synchrotron photons generated in the jet itself in the synchrotron self-Compton (SSC) scenario, or on external radiation fields from the accretion disk, BLR, or dusty torus in external inverse Compton (EIC) scenario [12–22]. In hadronic and lepto-hadronic models, HE emission can instead arise from proton synchrotron radiation or from secondary particles created in photo-hadronic interactions. These scenarios are attractive because they provide a natural connection between electromagnetic emission and neutrino production, but they also generally require more demanding energetics and more complex modeling [23–27].

Blazars are usually divided into two major subclasses according to their

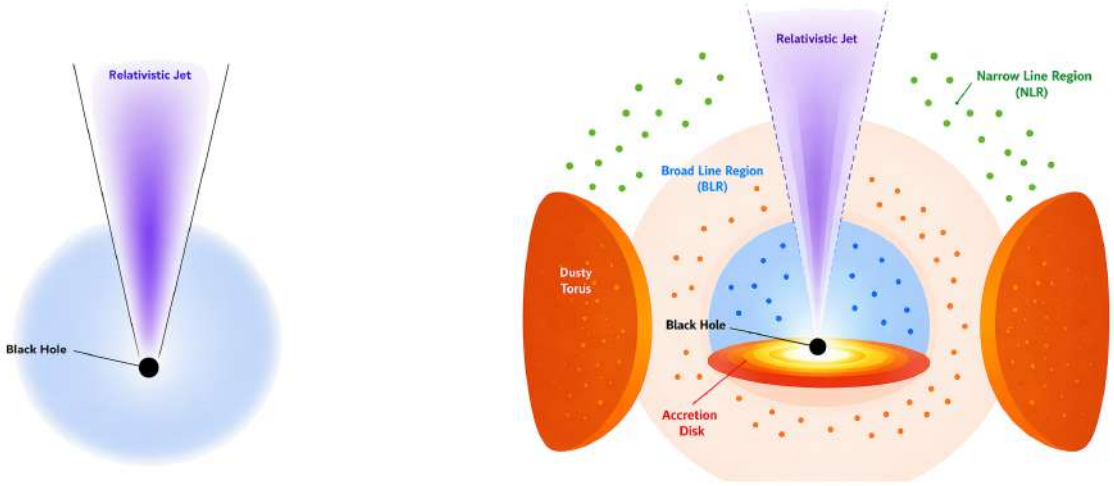

Figure 2: Schematic comparison of the two main blazar subclasses. The left panel shows a BL Lac object. The right panel shows an FSRQ, where the luminous accretion disk, broad-line region, and dusty torus provide strong external photon fields that can power the EIC component. Adapted from Tavecchio (XVIII International Workshop on Neutrino Telescopes presentation, 2018).

optical spectra. Flat-spectrum radio quasars (FSRQs) show strong, broad emission lines and generally host luminous accretion disks, bright BLRs, and intense external photon fields. BL Lacertae objects (BL Lacs) show weak or absent emission lines and usually have less prominent thermal and line-emitting environments. The structural differences between these two subclasses are illustrated in Figure 2. This separation is important because it reflects a physical difference in the radiative environment of the jet. In BL Lacs, the emission is often well described by synchrotron and SSC processes, while in FSRQs the HE component is frequently dominated by scattering of external photons. A second and complementary classification is based on the location of the synchrotron peak frequency, dividing blazars into low, intermediate, and high-synchrotron-peaked sources (LSPs, ISPs, and HSPs). Their characteristic SEDs are shown in Figure 3. In this scheme, FSRQs are mostly LSP objects, while BL Lacs occupy a much broader range and include the most extreme HSP systems [2, 28, 29].

Despite decades of blazar studies, many key problems remain open. The launching, collimation, and long-distance propagation of relativistic jets are not fully understood yet. The jet composition, in particular the relative role of magnetic fields, electrons, positrons, and protons, remains uncertain.

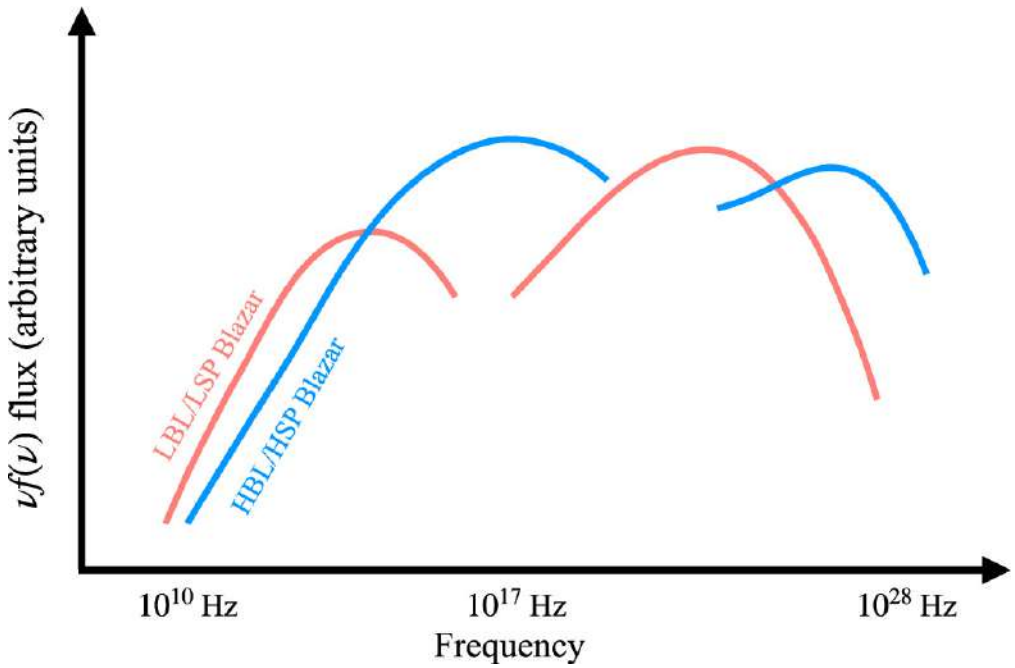

Figure 3: Representative spectral energy distributions of blazar subclasses by synchrotron peak placement. The red curve corresponds to LSP blazars, while the light-blue curve represents HSPs [30].

The structure and evolution of the magnetic field are still under debate, as are the dominant acceleration mechanisms responsible for producing ultra-relativistic particles. The physical origin of flares, especially the fastest ones, is also not fully understood. Even more fundamentally, the dominant origin of the HE emission in many blazars is still unclear: in some sources, leptonic scenarios appear sufficient, while in others hadronic or hybrid processes are also highly possible. In addition, large modern catalogs include many sources that are blazar-like but not accurately classified, which limits population studies and source selection for follow-up campaigns. To address these unresolved issues, both improved observations and better data-analysis methods are needed.

In recent years, machine learning has become an important tool in astronomy and astrophysics because it can extract hidden patterns from large datasets and can also be used for computationally expensive physical models. In the context of blazar studies, these two methods are especially useful. First, machine learning methods can be used to classify blazars that lack clear optical classifications based on their observed spectral and temporal properties. Second, neural network models can approximate expensive radiative solvers,

allowing large numbers of SEDs to be modeled much faster than by direct repeated numerical computation. This accelerates physical modeling rather than replacing it, making large-scale studies feasible. In this thesis, both aspects of machine learning are explored [3, 27, 31–34].

The structure of the thesis is as follows.

- Section 1 provides a general overview of AGNs and blazars, their radiation mechanisms, the main data sources used in this work, and the machine learning methods relevant to the thesis.
- Section 2 investigates the classification of blazar candidates of uncertain type in the fourth *Fermi*-LAT catalog using gradient-boosted decision trees.
- Section 3 presents a Convolutional Neural Network (CNN) surrogate for one-zone SSC modeling and tests its use for broadband SED inference.
- Section 4 applies the trained modeling framework to a long-term, multi-epoch study of PKS 2155-304, with emphasis on changes in jet parameters across different activity states.
- Section 5 studies the origin of the multiwavelength emission from PKS 1441+25 and investigates how the location and physical state of the emitting region evolve during different phases of the flare.

1 BLAZARS, RADIATION MECHANISMS, AND MACHINE LEARNING METHODS

1.1 WHY BLAZARS ARE ESPECIALLY IMPORTANT

Blazars are interesting laboratories for exploring nonthermal processes in relativistic outflows. Their jets probe relativistic outflows launched close to supermassive black holes, which makes them relevant for accretion physics, magnetized plasma dynamics, and particle acceleration. Their emission often spans more than twenty orders of magnitude in frequency, from radio to VHE γ-rays. In many sources, the radiation is polarized in the radio and optical bands, and in some cases also in X-rays, indicating synchrotron emission and a complex magnetic-field structure. Their strongest flares can evolve on very short timescales, which implies compact emission zones and efficient dissipation.

A simple argument shows why is important for blazar studies. If a source at redshift z varies on an observed timescale $t_{\rm var}$, then it is required that the characteristic size of the emission region satisfies

$$R \lesssim \frac{c\, t_{\rm var}\, \delta}{1+z}. \tag{1.1}$$

Thus, hour or minute-scale variability immediately constrains the physical size of the zone in which the radiation is produced. In blazars this becomes especially important because the inferred size is much smaller than the overall scale of the jet, indicating that only a small part of the outflow is responsible for a given flare.

Blazars are also the dominant class of identified extragalactic sources in the HE γ-ray sky. Observations with *Fermi*-LAT have shown that they form the majority of detected sources in this band, and the most recent Fermi catalogs provide large samples with well-characterized spectral and variability properties [10]. At VHEs, detections by imaging atmospheric Cherenkov telescopes probe the most energetic particle populations and provide insight into the transparency of the source environment. Multimessenger observations have

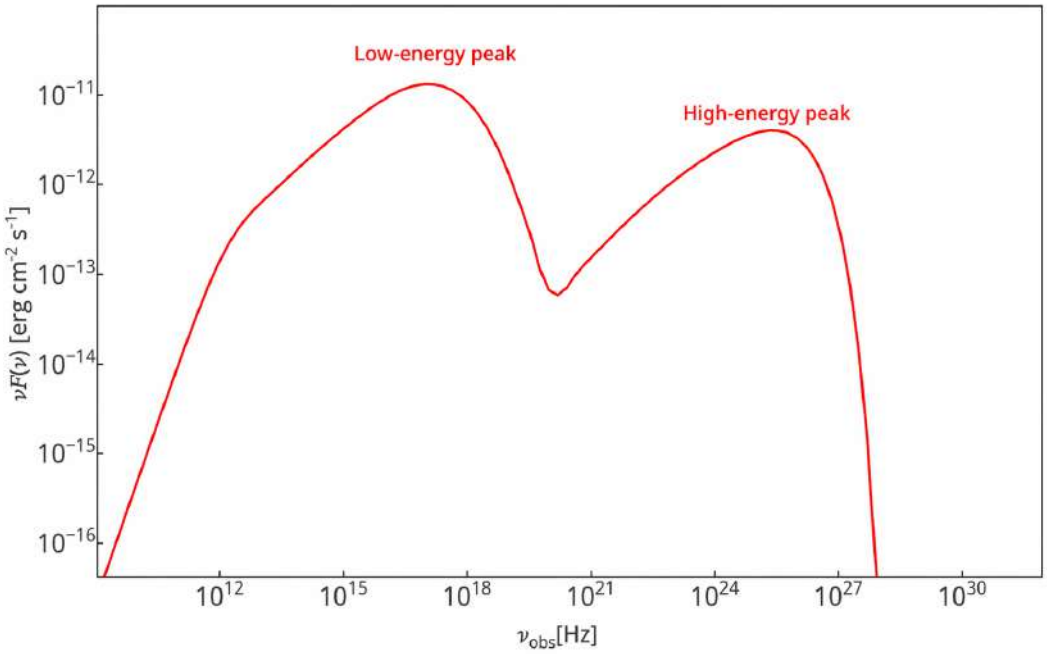

Figure 1.1: Representative schematic blazar SED showing the two broad components: the low-energy synchrotron bump and the high-energy bump.

further increased interest in blazars. The temporal and directional association of the blazar TXS 0506+056 with the neutrino event IceCube-170922A, together with an archival neutrino excess from the same direction, has established blazars as leading candidates for at least a fraction of the observed astrophysical neutrino flux [7–9]. While these results do not imply that all blazars are efficient neutrino emitters, they provide strong evidence that hadronic processes operate in at least some relativistic jets.

1.2 BROADBAND SPECTRAL ENERGY DISTRIBUTIONS OF BLAZARS

The broadband emission of blazars is usually represented through the SED νF_ν, which for most sources shows a characteristic two-bump structure (Figure 1.1). The first bump extends from radio to optical, ultraviolet, or X-ray bands depending on source type. The second bump extends from X-rays to HE and sometimes VHE γ-rays. The location, width, and luminosity of these two components vary strongly from one source to another and also change with activity state.

This two-bump shape which shows that blazar emission extends from radio to

VHE γ-ray band is one of the main reasons why blazars are challenging and attractive sources for theoretical studies. A successful model must explain the relative luminosities, peak frequencies, spectral curvature, variability, and cross-band correlations of both components. In some sources, the low-energy and high-energy components vary together, suggesting a close physical connection. In others, different bands show partially decoupled behavior, indicating multiple zones, multiple particle populations, or changing external conditions.

The observed SED also provides direct clues on the jet environment. For example, in many FSRQs the HE bump is much more luminous than the synchrotron bump, which shows presence of strong external photon fields. In contrast, many BL Lacs, especially HSPs, are successfully modeled with synchrotron and SSC emission only. The SED is therefore a central observational tool for testing radiation models.

1.2.1 SYNCHROTRON RADIATION AND THE LOW-ENERGY COMPONENT

The low-energy component of the SED is usually explained as synchrotron radiation from relativistic electrons moving in the jet magnetic field. When a relativistic electron, characterized by a Lorentz factor γ, spirals in a magnetic field B, it emits synchrotron radiation with a characteristic observed frequency.

$$\nu_{\rm syn} \simeq \frac{3eB}{4\pi m_e c}\,\gamma^2\,\frac{\delta}{1+z}. \tag{1.2}$$

This relation shows immediately why synchrotron radiation is so useful diagnostically: the observed peak depends on both the electron energy and the magnetic field. A shift of the synchrotron peak to higher frequencies may indicate larger γ, a stronger B, a larger Doppler factor, or some combination of these changes.

Synchrotron radiation explains several characteristic features of blazars. It naturally produces broad non-thermal spectra. It is also consistent with

the observed polarization in radio and optical bands. In addition, if the same electrons cool rapidly, synchrotron losses can contribute strongly to the variability pattern. In many blazars, the low-energy component therefore provides important information on the relativistic electron population and magnetic field inside the jet.

The shape of the synchrotron bump therefore constrains the basic plasma properties of the emitting region, most importantly the characteristic electron energies, the magnetic-field strength, and the amount of Doppler boosting. These constraints are essential because the same electron population is also expected to generate the HE component in leptonic models. For this reason, the synchrotron spectrum provides the natural starting point for interpreting the inverse-Compton bump discussed in the next subsection.

1.2.2 HIGH-ENERGY EMISSION: LEPTONIC SCENARIOS

In the leptonic scenarios, the HE component in blazar SED is explained as inverse Compton scattering. In this process, relativistic electrons transfer part of their energy to lower-energy photons. In the Thomson regime, the characteristic energy of the scattered photon scales approximately as

$$E_{\mathrm{IC}} \sim \gamma^2 E_{\mathrm{seed}}, \tag{1.3}$$

where E_{seed} is the energy of the seed photon. This simple relation shows how optical, ultraviolet, or infrared photons can be shifted into the X-ray or γ-ray band by electrons with sufficiently large Lorentz factors.

In the SSC scenario, the seed photons are the synchrotron photons produced within the emitting region itself [12–15]. The same electron population is therefore responsible for both SED peaks. This makes the SSC model especially attractive for BL Lacs, where strong external photon fields are often absent or weak. Because the synchrotron and SSC components are physically linked, changes in the electron distribution or magnetic field often affect both bumps in a correlated way.

In a one-zone leptonic description, this electron population is represented by a distribution function rather than by a single characteristic energy. A commonly used parametrization which is also supported by acceleartion theoreies is a power-law injection with an exponential cutoff,

$$Q_e = \begin{cases} Q_{e,0}\gamma^{-p}\exp\left(-\dfrac{\gamma}{\gamma_{\max}}\right) & \gamma \geq \gamma_{\min}, \\ 0 & \text{otherwise}, \end{cases} \tag{1.4}$$

where $\gamma_{\min}$ and $\gamma_{\max}$ are the characteristic energy range of the injected electrons, and p is the spectral index. The normalization $Q_{e,0}$ is related to the electron power through

$$L_e = \pi R^2 \delta^2 m_e c^3 \int_1^\infty \gamma Q_e d\gamma. \tag{1.5}$$

After injection, cooling and escape reshape this distribution, and the resulting electron population determines both the synchrotron spectrum and its SSC upscattering. This is why SSC modeling naturally links the low and high-energy SED components through the same set of particle and magnetic-field parameters.

In EIC models, the same electron distribution is remained, but the seed photons are dominated by radiation fields external to the emitting region. The main candidates are the direct disk radiation, photons from the BLR, and infrared photons from the dusty torus [16–22]. These models are often favored for FSRQs because such sources have luminous disks and dense external radiation fields. In this case, the jet does not need to generate the seed photons internally, and the Compton component can become strongly dominant over the synchrotron component. The basic geometry of the SSC and EIC scenarios is illustrated in Figure 1.2.

A useful physical distinction between SSC and EIC-dominated regimes is that the latter depends strongly on the location of the emitting region along the jet. If the dissipation occurs close to the black hole, the emitting electrons may interact mainly with disk and BLR photons. If the emitting region is farther away, the

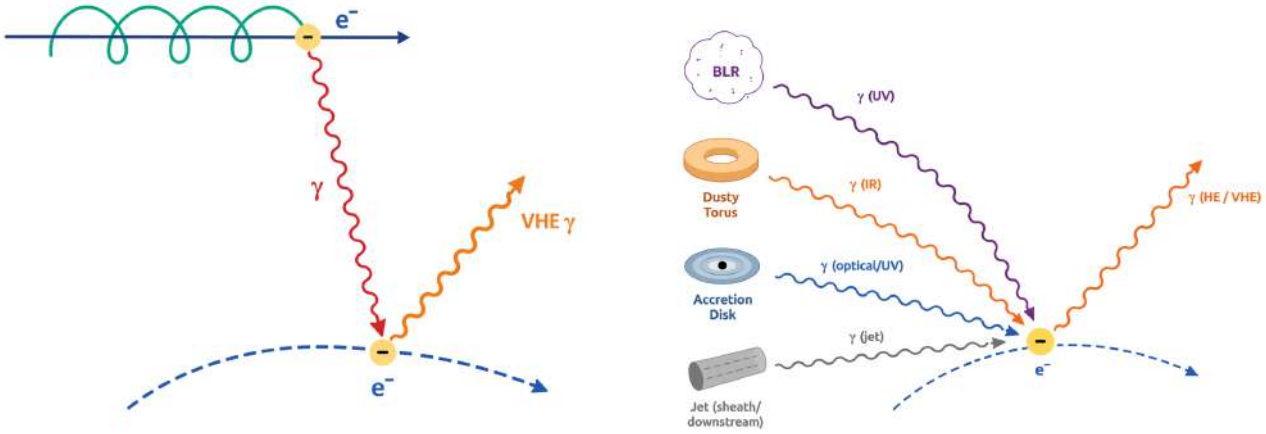

Figure 1.2: Schematic illustration of the two main leptonic emission scenarios commonly used to model blazar SEDs. *Left*: SSC scenario. *Right*: EIC scenario

torus field may dominate instead.

1.2.3 HIGH-ENERGY EMISSION: HADRONIC AND HYBRID SCENARIOS

Hadronic models offer an alternative interpretation of the HE component. In these models, relativistic protons carry a significant fraction of the jet power and contribute either directly or indirectly to the observed radiation. One possible mechanism is proton synchrotron emission, where ultra-relativistic protons radiate in strong magnetic fields. Another possibility is that ultra-high-energy protons interact with ambient photons through photo-hadronic processes, producing pions and secondary electrons, positrons, and neutrinos. The decay chain can be written schematically as

$$p + \gamma \to \pi^0 + X, \qquad \pi^0 \to 2\gamma, \tag{1.6}$$

$$p + \gamma \to \pi^\pm + X, \qquad \pi^\pm \to \mu^\pm + \nu_\mu/\bar{\nu}_\mu, \tag{1.7}$$

$$\mu^\pm \to e^\pm + \nu_e/\bar{\nu}_e + \bar{\nu}_\mu/\nu_\mu. \tag{1.8}$$

These channels make hadronic models especially interesting in the multimessenger context, because neutrino production follows naturally from the same interactions that produce part of the electromagnetic emission

[7–9, 23–25, 27].

Hadronic interpretations are attractive because they connect jet emission to the acceleration of the highest-energy particles and to neutrino production. However, they often require strong magnetic fields, very energetic protons, or large jet powers. In many sources, these requirements make the models more demanding than purely leptonic alternatives. For this reason, the current picture in blazar physics is not that one family of models has replaced the other. Rather, different sources and different epochs may favor different scenarios, and in some cases hybrid models may be required.

1.3 MULTIWAVELENGTH DATA SOURCES

Because blazars emit across such a wide energy range, progress in understanding the origin of their emission depends on observations at multiple wavelengths. Measuring the full SED requires combining data from multiple data sources, often requiring careful treatment of calibration, simultaneity, and variability.

In this thesis, the observational data from individual missions, archives, and the Markarian Multiwavelength Data Center (MMDC)[1] are used. MMDC is an open-access platform that provides uniformly processed light curves and time-resolved SEDs for blazars by combining newly analyzed and archival data in the γ-ray, X-ray, optical/UV, and other bands [30]. This data infrastructure is used directly in the source-oriented studies presented later for PKS 2155-304 (Section 4) and PKS 1441+25 (Section 5), where data from MMDC are downloaded to investigate the temporal and spectral properties of the sources as well as to construct quasi-simultaneous multiwavelength datasets. In addition, the MMDC platform makes available the CNN-based radiative-modeling framework developed in this thesis and in the associated modeling papers, including the SSC and EIC implementations [3, 34].

In this thesis, the date from two observatories play a central role in addition to archival and ground-based data: the Neil Gehrels Swift Observatory (*SWIFT*)

[1] https://mmdc.am

and the *Fermi* Large Area γ-ray Space Telescope (*Fermi*-LAT).

The *SWIFT* mission was launched in 2004 and provides rapid-response multi-band observations. Although it was designed primarily for γ-ray bursts, it is also a key instrument for blazar studies because it offers quasi-simultaneous coverage in the optical/UV and X-ray bands [35]. X-Ray Telescope (XRT) is especially important for probing the blazar SED in the X-ray band, while the Ultraviolet/Optical Telescope (UVOT) constrains the synchrotron tail and, in some cases, the thermal emission from the accretion disk.

The *Fermi*-LAT, launched in 2008, is a pair-conversion γ-ray telescope operating from tens of MeV to hundreds of GeV and surveying the whole sky approximately every three hours [36]. For blazar research, the *Fermi*-LAT provides long-term light curves, spectra, and source catalogs that are essential for studying both population properties and individual flares. In particular, the fourth *Fermi*-LAT source catalog (4FGL) and its later data releases provide a homogeneous description of γ-ray sources through spectral parameters, variability information, and source associations [10, 37].

The classification studies in this thesis is based on observed properties from 4FGL-DR3, while the source-specific studies of PKS 2155-304 and PKS 1441+25 use γ-ray data from *Fermi*-LAT observations.

A key practical challenge in blazar studies is the difficulty of achieving strict simultaneity across different wavebands. Because many blazars exhibit strong variability, observations separated by even a few days may correspond to different physical states. This significantly complicates time-resolved SED modeling, which requires not only broad spectral coverage but also careful selection of time intervals during which the source can be reasonably assumed to be in a consistent or well-characterized state.

1.4 MACHINE LEARNING METHODS AND APPLICATIONS

Machine learning is a set of methods that learn useful relations directly from data [38]. In supervised learning, one starts from input-output pairs and trains a model to predict the target quantity from the measured features. In astronomy,

the target may be a class label, a physical parameter, a probability, or a full spectrum. The strength of machine learning is that it can represent complicated nonlinear relations that are difficult to capture with simple analytic cuts.

In the thesis, two different machine learning methods are used.

First, it is used for **classification**. In supervised classification, the model is trained on examples for which both the input features and the correct class labels are known. It then learns how measured properties are related to class membership and applies this rule to new objects [39]. In this thesis, the inputs are observed blazar properties, while the target is the subclass label, BL Lac or FSRQ. The task is therefore to use the properties of already classified sources to predict the most likely type of blazars of uncertain type.

Second, machine learning is used for **surrogate modeling**. A surrogate model, also called an emulator, is a fast approximation to a physical model that is computationally expenisve. Here, the training set is not built from observations, but from synthetic spectra produced by a radiative code across a wide range of physical parameters. The network is trained to learn the mapping from model parameters to the corresponding SED. From a machine learning point of view, this is a supervised regression problem with a structured one-dimensional output: the target is a full ordered spectrum, so neighboring bins are correlated and the global shape must be reconstructed consistently. Once trained, the surrogate can replace repeated expensive solver calls with a fast network evaluation, which makes likelihood calculations and Bayesian inference practical for large samples and multi-epoch studies.

In summary, in this thesis machine learning is used in two complementary ways: to classify blazars from observed data, and to accelerate physical modeling by learning a fast approximation of the radiation solver. The first problem is a classification task on tabular observables, while the second is a regression task in which the model reconstructs a full spectrum from physical input parameters.

1.4.1 ALGORITHMS USED IN THIS THESIS

The machine-learning methods used here were selected according to the structure of the data and the scientific goal.

Gradient-boosted decision trees. For the problem of BCU classification, the input data are tabular and contain missing values. For such data, algorithms based on gradient-boosted decision trees are especially effective. The predictive model is written as a sum of weak learners,

$$\hat{y}(\mathbf{x}) = \sum_{m=1}^{M} f_m(\mathbf{x}), \tag{1.9}$$

where each f_m is a decision tree and $\mathbf{x}$ is the vector of input observables. The trees are added sequentially by minimizing a regularized objective,

$$\mathcal{L} = \sum_{i=1}^{N} l(y_i, \hat{y}_i) + \sum_{m=1}^{M} \Omega(f_m), \tag{1.10}$$

where l is the training loss and Ω penalizes overly complex trees. Thus, at iteration m, the new tree is trained to reduce the residual errors left by the previous ensemble. Two implementations are used in this thesis: XGBoost and LightGBM [32, 33]. They are good choices for catalog-like data because they handle nonlinear relations well, are robust to mixed feature importance, and can cope naturally with missing entries.

Artificial Neural Networks. ANNs apply successive nonlinear transformations to the input data through layers of connected units [31]. For a hidden layer l, the basic operation is

$$\mathbf{h}^{(l+1)} = \sigma\left(\mathbf{W}^{(l)}\mathbf{h}^{(l)} + \mathbf{b}^{(l)}\right), \tag{1.11}$$

where $\mathbf{W}^{(l)}$ and $\mathbf{b}^{(l)}$ are the trainable weights and biases, and σ is a nonlinear activation function. For classification, the final layer produces class

probabilities, typically through a softmax function,

$$P(c \mid \mathbf{x}) = \frac{\exp(z_c)}{\sum_j \exp(z_j)}. \tag{1.12}$$

ANNs are powerful general-purpose function approximators and are widely used in classification and regression problems. However, for small or sparse tabular datasets they may be less efficient than boosted-tree methods, especially when missing values are common.

Convolutional Neural Networks (CNNs). A CNN is designed to process data with an ordered structure, where nearby elements are related to each other. CNN applies a set of small learnable filters (or kernels) that slide across the input (in one dimensional case it is input sequence). Each filter examines only a local region at a time and produces a *feature map*, highlighting where a certain pattern is present. In practice, different filters can learn to respond to different local structures, such as rising or falling slopes, curvature changes, narrow features, or the edges of broad peaks. Because the same filter is reused over the whole sequence, CNNs need far fewer parameters than fully connected networks and can detect similar patterns regardless of where they appear [40]. Figure 1.3 shows a schematic overview of the same idea in the case of two-dimensional convolution.

Formally, for a one-dimensional convolutional layer,

$$h_j^{(l+1)}(i) = \sigma\left(\sum_m \sum_{u=0}^{k-1} w_{jmu}^{(l)}\, h_m^{(l)}(i+u) + b_j^{(l)}\right), \tag{1.13}$$

where $h_m^{(l)}$ is the input from channel m in layer l, $w_{jmu}^{(l)}$ are the filter weights, k is the kernel size, $b_j^{(l)}$ is a bias term, and σ is a nonlinear activation function. Stacking several convolutional layers allows the network to build a hierarchy of features: early layers extract simple local patterns, while deeper layers combine them into more global structures. In the case of broadband spectra, this means that the network can move from identifying local slopes and curvatures to capturing the

overall shape of the synchrotron and inverse-Compton bumps.

In this thesis, CNNs are used for *surrogate modeling* of radiative calculations. The goal is to learn the mapping

$$\hat{\mathbf{S}}(\nu) = g_\phi(\boldsymbol{\theta}), \tag{1.14}$$

where $\boldsymbol{\theta}$ denotes the physical SSC model parameters and $\hat{\mathbf{S}}(\nu)$ is the predicted SED sampled on a frequency grid. This is a suitable application for CNNs because an SED is not just a collection of independent values: neighboring frequency bins are strongly correlated, and the physically meaningful information is encoded in features such as peak position, width, curvature, and relative bump amplitudes. By using convolutional filters, the network can efficiently learn these structured spectral patterns and reproduce smooth model spectra much faster than the original numerical solver. The training is performed by minimizing the difference between the predicted and numerically computed spectra, usually through a mean-squared error loss,

$$\mathcal{L}_{\text{MSE}} = \frac{1}{N}\sum_{i=1}^{N} \left\| \mathbf{S}_i - \hat{\mathbf{S}}_i \right\|^2. \tag{1.15}$$

This makes CNNs a natural and efficient tool for emulating SSC and related radiative models [3, 27, 34].

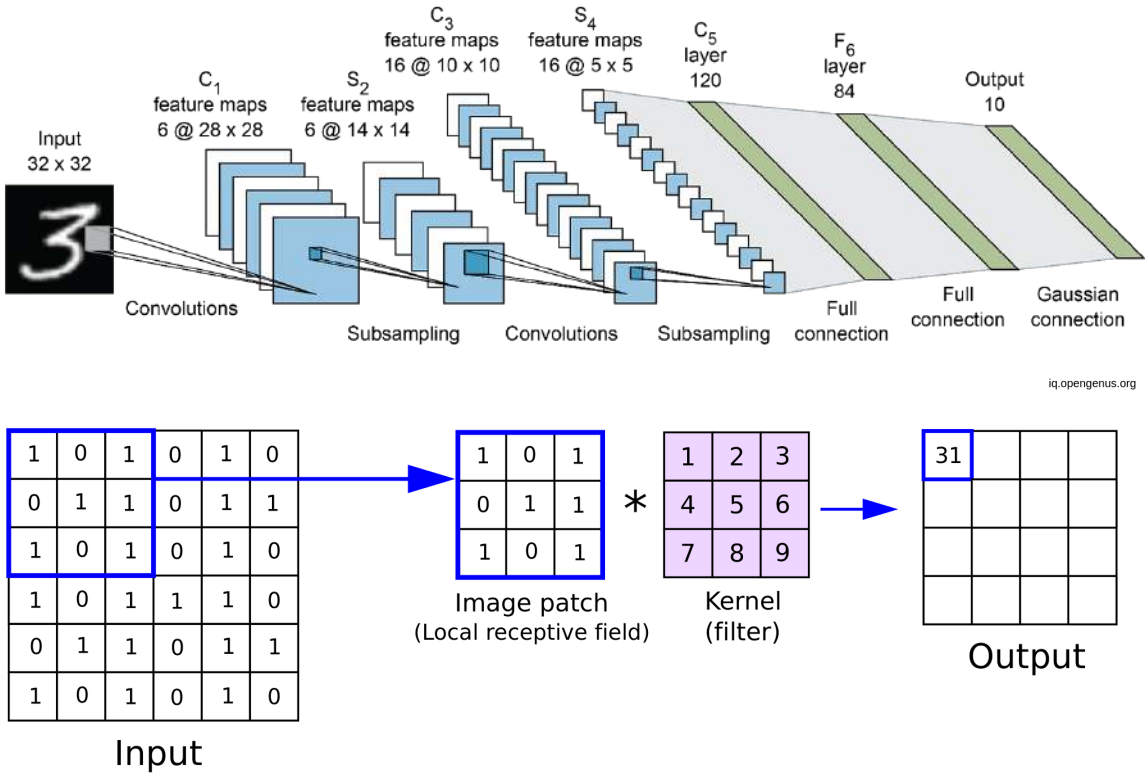

Figure 1.3: Illustrative example of a two-dimensional convolution. The top panel shows how sliding convolutional filters extract feature maps from the input source image. The bottom panel shows how the convolution operation is performed on a local image patch using a kernel.

2 GRADIENT BOOSTING DECISION TREES CLASSIFICATION OF BLAZARS OF UNCERTAIN TYPE IN THE FOURTH FERMI-LAT CATALOG

2.1 INTRODUCTION

Blazar candidates of uncertain type (BCUs) form a large fraction of the blazar population reported in the fourth *Fermi*-LAT source catalog. In 4FGL-DR3, BCUs account for 39.9% of all cataloged blazars [10], so the lack of a firm subclass assignment is limiting the population studies. The same limitation appears when targets are selected for dedicated follow-up observations, because the scientific priority for observing a source depends on its subclass. Constraining the nature of BCUs is therefore essential for using all blazar samples observed in the γ-ray band with *Fermi*-LAT.

The importance of blazar association has increased even more in the era of multi-messenger astrophysics. The reported associations between blazars and HE neutrino events detected by IceCube renewed interest in identifying the most promising sources for VHE neutrino emission and their theoretical studies [7–9].

Although optical monitoring and spectroscopy remain the most direct way for a firm classification of blazars, they are difficult to apply uniformly to the full BCU population because of the large number of targets, which makes the task time-consuming. Another approach is to use statistical and machine learning methods to find patterns in the observational data in the *Fermi*-LAT catalog. In the past, several studies have shown that the measured γ-ray and multiwavelength properties of blazars contain enough information to support a statistical separation between BL Lacs and FSRQs. Previous works used ANNs, Bayesian neural networks, deep-learning approaches, and other machine-learning classifiers to study blazar properties, classify unassociated γ-ray sources, or assign subclasses to BCUs [41–46]. These results show that machine learning methods can help to classify the sources using observational properties, while also indicating that the quality of the classification depends strongly on the completeness of the training sample and on the choice of the

methodology.

In addition to the previous studies, this work is motivated by the availability of new a large, uniform γ-ray dataset from blazars observations that is included in the 4FGL-DR3 catalog [10]. At the time of this work, this release represented one of the most complete datasets, based on 12 years of *Fermi*-LAT observations. It includes both spectral measurements and flux histories for a large and homogeneous sample of BL Lacs and FSRQs. The size and scope of such a dataset make it possible to classify BCUs, because it already contains enough classified sources to use as a learning reference.

The scientific goal of this section is to use the spectral and temporal γ-ray properties reported in 4FGL-DR3 for already classified BL Lacs and FSRQs to train a neural network, which can then be used to classify BCUs based on their γ-ray properties. In this work, we use ANN [31] as a baseline classifier, together with two state-of-the-art implementations of gradient-boosting decision trees, namely XGBoost and LightGBM [32, 33]. The goal is to build the classification in the same observational space for all three models and then test whether the predicted BCU subclasses are robust across both the ANN baseline and the specific boosting framework that is used. This comparison is scientifically useful because agreement between independent models from different algorithmic families strengthens confidence that the assigned classes show structure in the data rather than details of a single methodological realization.

The goal of this section is to provide a statistically grounded classification of the BCU population in 4FGL-DR3 and to assess how the predicted subclasses compare with the known BL Lac and FSRQ samples. This will not replace future spectroscopic identification, but it substantially improves the practical value of the *Fermi*-LAT catalog by extending subclass information to sources that would otherwise remain excluded from many analyses. In this sense, the section has two related purposes: it provides an updated catalog-level classification of BCUs based on the available γ-ray data and establishes a well-defined reference sample for the broader discussion of blazar populations and source selection

presented later in the thesis.

2.2 THE SOURCE SAMPLE FROM 4FGL-DR3

The incremental version of the fourth *Fermi*-LAT catalog (4FGL Data Release 3 [DR3]) contains 6659 sources and for each individual source together with the coordinates, various spectral properties are provided, such as flux, detection significance, spectral parameters when fitting with different models, etc. For our study, from 4FGL DR3 we selected all sources with BLL, FSRQ and bll, fsrq designations where in capital letters are firm identifications whereas lower case letters indicate associations [see 10]. This amounted to 2250 sources (1456 BL Lacs and 794 FSRQs) to train our models. Then those models are applied to classify 1493 blazar candidates.

Among the features and measurements presented in 4FGL, we are interested in the energy spectra and fluxes measured in different periods; the first correspond to the sources' fluxes measured in different energy bands (*nuFnu_band* column) while the second one represent the sources' flux as a function of time (*Flux_History* column). These two measurements well characterize different blazar sub-classes and are used as input parameters for our models.

2.2.1 γ-RAY LIGHT CURVES

4FGL contains information on the γ-ray flux of the considered sources in different time bins (light curve) which is an essential information on the blazars emission features observed in the initial 12 years of *Fermi*-LAT operation. These light curves were computed by dividing the whole time period into twelve intervals (one year each) and the fluxes in each sub-interval were estimated by applying binned (up to 10 GeV) and unbinned (10-100 GeV) likelihood analysis. These fluxes were estimated by freezing the spectral parameters to those obtained in the fit over the full range and by adjusting the normalization. The photon fluxes estimated in the energy range 0.1-100 GeV in the units of photon $\mathrm{cm}^{-2}\ \mathrm{s}^{-1}$ are reported for each year.

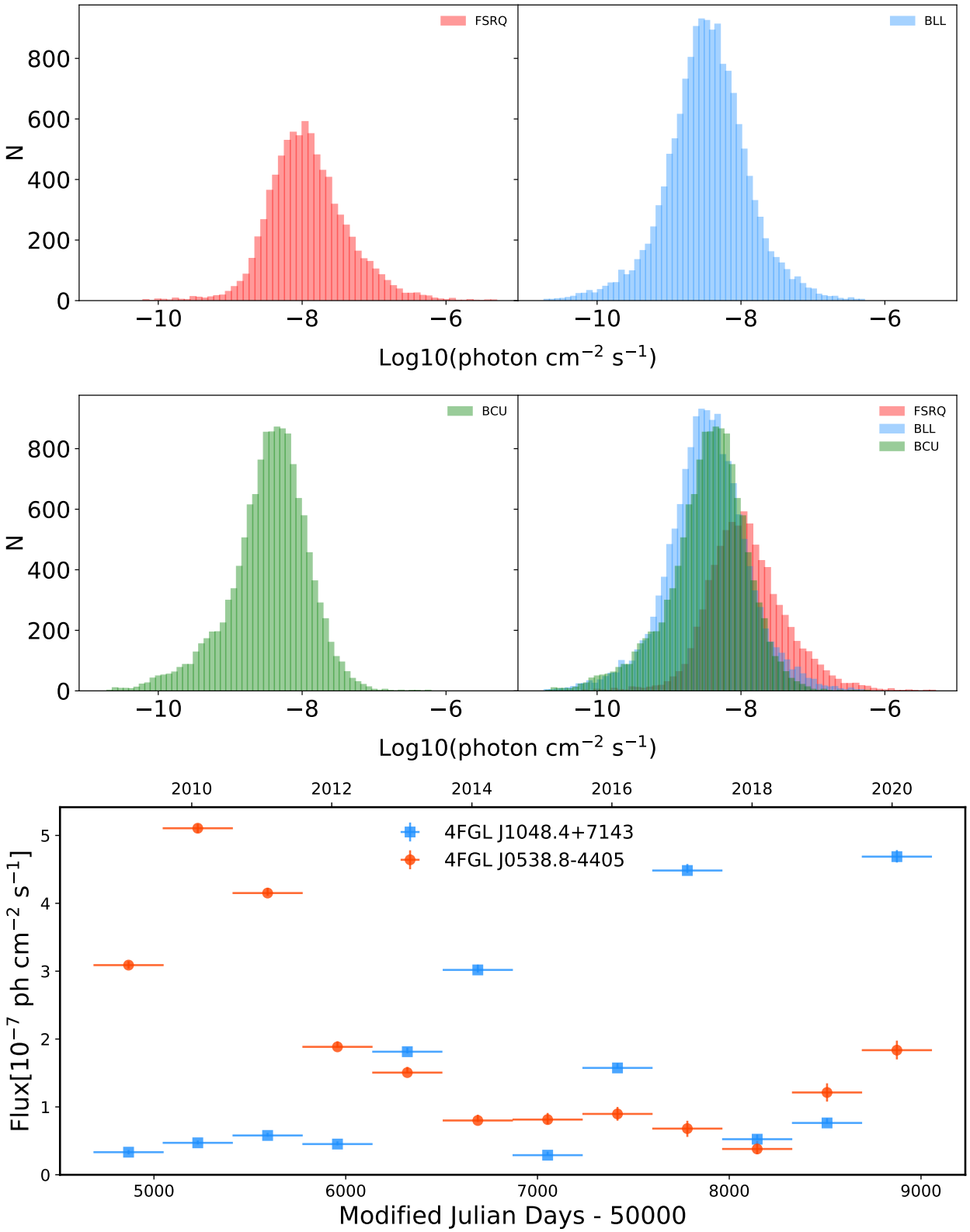

Figure 2.1: *Upper and middle panels:* The distribution of yearly fluxes of FSRQs, BL Lacs and BCUs included in the 4FGL catalog. *Lower panel:* The light curves of 4FGL J0538.8-4405 (BL Lac) and 4FGL J1048.4+7143 (FSRQ) measured during 12 years (2008-2020).

For each selected source this creates twelve parameters that describe the γ-ray flux evolution in different periods. One may speculate that the short time flux variability will be smoothed out when measuring the flux in one-year intervals. However, the goal is to identify common patterns in the change of the γ-ray flux of blazars in different sub-classes rather than to compare the variability timescales. Moreover, by comparing the variability of blazars using 2-month and 1 year light curves, Abdollahi et al. [37] showed that among 1173 sources identified as variable in 2-month intervals, 1057 show variability also in yearly binned intervals. Therefore, the one-year-binned light curves contain most of the variability information on the considered sources. Also, when the flux is measured in shorter periods, it might result in many upper limits which creates additional uncertainties for the models.

The distribution of the yearly measured fluxes of BL Lacs, FSRQs and BCUs is shown in Figure 2.1 (upper and middle panels), highlighting the difference in their γ-ray emission. For example, the mean of FSRQ γ-ray fluxes distribution is at 3.28×10^{-8}photon cm^{-2} s^{-1} while that of BL Lacs is at 8.19×10^{-9}photon cm^{-2} s^{-1}. FSRQs are brighter with a highest yearly flux of 5.05×10^{-6} photon cm^{-2} s^{-1} observed for 4FGL J2253.9+1609 (3C 454.3) as compared with the similar value of 5.2×10^{-7} photon cm^{-2} s^{-1} observed for BL Lacs, 4FGL J2202.7+4216 (BL Lacertae). The BCU yearly fluxes distribution with a mean of 6.72×10^{-9} photon cm^{-2} s^{-1} is broader, mimicking the properties of both FSRQs and BL Lacs. The distribution of yearly fluxes of FSRQs, BL Lacs and BCUs are shown together in Figure 2.1 middle panel right side.

The fluxes estimated in each interval represent an independent state of the sources and show their brightest and lowest emission states. The light curves of the sources (FSRQ and BL Lac) shown in Figure 2.1 (lower panel) clearly demonstrate their different emission states. For example, BL Lac 4FGL J0538.8-4405 (orange circles in Figure 2.1 lower panel) is initially in the high γ-ray emission state while it is in a relatively faint state in 2014, but then brightens again at the end of the considered period. Instead, the emission from

FSRQ 4FGL J1048.4+7143 (blue squares in Figure 2.1 lower panel) is initially in a relatively faint state but then it is in repeatedly flaring and quiescent states. Therefore, given that blazar emission is variable, a simple comparison of the fluxes of different sources estimated in the same year does not have any physical motivation. On the other hand, the change in the flux is linked with the source properties and it is meaningful to compare the fluxes when the sources are in the lowest, average or brightest emission states. Thus, we have sorted the early measured fluxes from the lowest to the highest and they are considered as twelve different input parameters. So, the network can compare and contrast the fluxes of sources whether they are in low or bright emission states. Some sources do not have the flux measured for all yearly bins, only the upper limits are given, so these data are missing. For the periods with no detection (upper limit) zero or NaN were set, depending on the method, meaning that there is no information.

2.2.2 γ-RAY SPECTRA

It is known that the γ-ray spectra of BL Lacs and FSRQs shown distinct differences. For example, Abdollahi et al. [37] have shown that 93% of FSRQs have power-law photon indices > 2.2 while those of 81% of BL Lacs < 2.2. However, the photon index of BL Lacs varies also for LBLs, IBLs and HBLs; the γ-ray spectra of LBLs are softer than those of HBLs [see e.g., 47]. In principle, the difference between FSRQs and BL Lacs can be of a purely physical origin. In BL Lacs jets the electrons can be accelerated to higher energies, having a harder energy spectrum and hence producing photons with harder spectra. Instead, in FSRQs where the electrons effectively interact with different photon fields and efficiently cool down, the produced photons will appear with a soft γ-ray spectrum. Therefore, the spectral difference between FSRQs and BL Lacs can be used for BCU classification.

The 4FGL catalogue provides the sources fluxes (spectra) measured in eight energy bands: *1)* 50–100 MeV, *2)* 100–300 MeV, *3)* 300 MeV–1 GeV, *4)* 1–3 GeV, *5)* 3–10 GeV, *6)* 10–30 GeV, *7)* 30–100 GeV and *8)* 100 GeV–1 TeV. We excluded the

first band, as at lower energies the fluxes could be affected by contamination of other sources. Visually inspecting plots of spectral fits of all sources, we decided to drop the last band as well because it is an upper limit for many sources, and work with the remaining 6 bands. The fluxes in each of these bands contain information of average spectra of the sources (e.g., spectral index, spectral curvature, spectral breaks, etc.) and can be used to distinguish between different types of blazars. The fluxes measured in each energy band were not sorted and provided as input according to the increase of the energy because they are defined by the photon index which is different for FSRQs and BL Lacs. There is already a physical interpretation for the fluxes in the same input parameter, so their compression is meaningful.

2.3 MODEL CONSTRUCTION

The aim of this work is to examine the nature of BCUs in 4FGL based on their γ-ray properties. The spectral and temporal properties discussed in the previous section provide a framework for predicting the expected types of unclassified blazars. This is done by defining models that find correlations between measured γ-ray properties of BL Lacs and FSRQs and then compare them to the γ-ray properties of BCUs. Here, we have implemented two different machine learning techniques to classify BCUs: Artificial Neural Network (ANN) and Gradient Boosted Decision Tree algorithm. Below we briefly introduce the general features of the used techniques.

- *Artificial Neural Network*

  ANNs [31] are among the most powerful tools in pattern-recognition problems. ANNs have been used successfully in various fields, including astrophysics and cosmology [e.g., 41, 42, 48–52].

  ANN consists of input, hidden, and output layers with connected neurons (nodes) representing a simplified model of the human brain functioning and the nervous system. A standard neural network contains an input layer and an output layer but in most cases it can include any number of hidden layers

with any number of hidden nodes in each layer. The input parameters, neurons in the input layer, are connected to one or more neurons in the hidden layer (intermediate layer) and propagate the data to the deeper layers and send the final output data to the last output layer (prediction). Each neuron in the first hidden layer is assigned weights associated to input parameters which indicates the importance of each neuron in the network. The goal of ANN training is to minimize the output error by finding the best set of weights for each connection. Initially, the weights are assigned randomly and are optimized during an ANN training. So, the ANN uses the input data to produce an output data which is compared with the real data to calculate the error (loss function). Then, ANN learns by adjusting its weights such that in the next iteration the net error produced by the ANN is generally smaller than that in the current iteration. So, it optimizes the weight values to get the best result from the network.

In our case, when the classification is the goal, the input parameters (fluxes in different years and fluxes in each energy bin) are values describing blazars while output layer is the number of classes (FSRQ or BL Lac). The network is trained (i.e., to find a function which best separates objects belonging to different classes) on already classified BL Lacs and FSRQs, tested on a selected sample of classified sources that was not used in the training, and then the resultant model can be used to classify BCUs.

- *Gradient Boosted Decision Tree*

  Gradient Boosted Decision Tree (GBDT) is a machine learning algorithm used for both classification and regression problems. Boosting is one technique which aims to build a strong classifier from a number of weak classifiers, so it is forward-learning ensemble method that obtains results by gradually improving the estimations. Initially, a model (e.g., a tree) is fitted to the data, and then a second model is constructed by improving the cases where the accuracy of the first model was not good. Then, these

processes of boosting are repeated many times to create a series of decision trees that produce an ensemble of weak prediction models; each successive model attempts to correct for the weakness of all the previous models and the combination of new models is better than the previous ones alone. In the gradient boosting method the loss function is minimized by adding trees in a gradient descent procedure. Namely, the very first model is trained on the dataset, whereas the second model is trained on the errors of the first model and added to the first model and so on. GBDT algorithms have wide applications and been used also in astronomy and astrophysics in a variety of problems [e.g., 53–56].

Here we use *XGBoost* and *LightGBM* methods based on gradient boosting algorithm to classify BCUs. Extreme Gradient Boosting (XGBoost) [32] is a scalable machine learning algorithm for tree boosting where the best model is found by applying more accurate approximations. Unlike GBDT, in *XGBoost* model the objective function is optimized using Newton-Raphson method, i.e., second-order partial derivatives are used to gather more information about the direction of the gradient and the way to get to the minimum of the loss function. *LightGBM* is another implementation of GBDT [33]. *LightGBM* uses portion of the data with low memory cost applying two novel approaches for sampling: Gradient-based One-Side Sampling and Exclusive Feature Bundling. In contrast to *XGBoost* where the trees are growth level-wise (horizontal), in *LightGBM*, the decision trees are grown vertically, which can reduce more loss and provide a more accurate result. The goal of both algorithms, *XGBoost* and *LightGBM*, is the non-linear mapping from a set of input parameters to an outcome, namely, a prediction whose possible numerical values are spanned by the set of leaves. As an output, it provides a probability whether the source belongs to BL Lac or FSRQ sub-classes.

Both methods apply conceptually different approaches in transferring the input data into output models. The complex methods based on neural networks

(like ANN) pose many challenges when applied to tabular data which contains sparsity (missing values, e.g., yearly fluxes in our case). The simple filling in of missing values with 0 or other constant might result in finding biased patterns in the data training or might significantly affect the obtained results. Instead, generally, the methods based on GBDT (like *XGBoost* and *LightGBM*) dominate when used on tabular data, showing superior performance. These algorithms can be trained on the data with missing values without doing imputation first and the tree branch directions for missing values are learned during training, each time deciding the best way to handle them. In addition, the algorithms based on decision trees are more applicable on the comparably small data sets (as in our case), as the complex methods based on neural networks tend to overfit the models. Thus, state-of-the-art algorithms, *XGBoost* and *LightGBM*, are more powerful and preferable tools for the classification of blazars. However, for a comparison we also performed classification using ANNs.

2.3.1 TRAINING AND TESTING

The data presented in previous section are used to train models and predict BCUs. Among the considered sources we dropped those which have three or more energy intervals with upper limits; in total 104 sources were dropped (73 BCUs and 31 FSRQs and BL Lacs). The entire dataset consists of 2219 rows from which 80% was selected as training set while 20% was the test set. We have used a 15-fold cross-validation procedure to evaluate the performance of the algorithms. In this procedure, the dataset is divided into 15 non-overlapping folds and the fitting is performed using 14 folds. Then, the model is validated using the remaining 15th fold. This procedure is repeated until every 15 folds serve as a validation and the average is taken as performance of the network. In this way, each of the 15 folds is given an opportunity to be used as a held-back validation set.

In our dataset each blazar (whether FSRQ or BL Lac) is characterized by 18 parameters: 12 yearly sorted γ-ray fluxes and 6 fluxes in each band. The

BL Lacs and FSRQs with evident differences (see Section 2.2 and Figure 2.1) occupy a different region in this parameter space and the goal is to quantify and determine the differences. In the ANN, the input neurons are 18, equal to the number of the input parameters, and we used three hidden layers with 64, 128 and 64 neurons. To prevent overfitting, we added two dropout layers, between hidden layers, to randomly set units to 0 with a frequency of 0.4 and 0.5. The number of neurons in hidden layers was selected by reducing the number of neurons but keeping the performance accuracy. The *XGBoost* and *LightGBM* classifiers contain a set of important hyperparameters, among which the most important are the number of leaf nodes, the learning rate, and the number of iterations. Different values of these hyperparameters may increase the model performance, so their best values were found by hyperparameter tuning, i.e., the best version of the models are found by running many jobs that test a range of hyperparameters on the training and validation datasets. We used HyperOpt package[2] which uses a form of Bayesian optimization for parameter tuning. We found the following optimal parameters for *LightGBM* model: the number of leaf nodes-31, learning rate-0.3, and number of iterations - 400, etc. However, in order to compare the resultant models, initially the model fitting was performed with the default parameters (*XGBoost_def* and *LightGBM_def*) and then with the optimized parameters (*XGBoost_opt* and *LightGBM_opt*). In all the trained models, the output was set up to have two possibilities, i.e., it returns the likelihood of a source to belong to either FSRQs ($L_{\rm FSRQ}$) or BL Lacs ($L_{\rm BL\,Lac}$). The likelihood is assigned such that $L_{\rm BL\,Lac} = 1 - L_{\rm FSRQ}$; the larger $L_{\rm BL\,Lac}$ (closer to 1) the higher the likelihood that the source is a BL Lac and vice-versa.

2.4 RESULTS AND DISCUSSIONS

In this section, we discuss the results of classification of BCUs from 4FGL. Table 2.1 provides summary results of applied models, showing their performance. To fully evaluate the effectiveness of the models, we compare the precision and recall. The precision measures the model's accuracy in classifying

[2] `https://github.com/hyperopt/hyperopt`

Table 2.1: The BCU classification performance of the models.

Model	Recall of Minority	Recall Weighted	Precision Weighted	ROC-AUC Macro
ANN	0.81	0.88	0.88	0.86
XGBoost_def	0.77	0.87	0.87	0.85
XGBoost_opt	0.80	0.87	0.87	0.86
LightGBM_def	0.81	0.87	0.87	0.86
LightGBM_opt	0.82	0.88	0.88	0.87

a sample as positive, i.e., the ability not to misclassify a BL Lac (FSRQ) as a FSRQ (BL Lac). Meanwhile, recall measures the model's ability to detect positive samples, i.e., the ability to identify all BL Lac (FSRQ) samples. Considering our dataset is slightly imbalanced, i.e., there are a disproportionate ratio of BL Lac and FSRQ classes (65:35), minority class (FSRQs in our case) has the highest interest from a learning point of view, as it can be under-classified. Therefore, we compare the models performance considering the recall of minority class (first column in Table 2.1) which shows that the *LightGBM_opt* model has the highest value for minority recall, 0.82, and a satisfactory precision, 0.88. Therefore, it provides the best BCU classification performance, so we report only the results obtained by this model.

In order to demonstrate the ability of *LightGBM_opt* to distinguish BL Lacs and FSRQs, the likelihood distribution of test sample is shown in Figure 2.2, left panel. The test sample contains 287 BL Lacs and 157 FSRQs, the ratio of which 287/157$\simeq$1.83 is the same as in the total sample (1436/783$\simeq$1.83). In the distribution, there are two evident and opposite peaks, BL Lacs (blue) centralized towards $L_{\rm BL\,Lac} = 1$ while opposite for FSRQs $L_{\rm BL\,Lac} = 0$, which clearly shows the ability of our model to separate BL Lacs and FSRQs from the test sample (not used during the training).

The performance of our applied model can be further examined from the confusion matrix shown in Figure 2.3 which summarizes the number of true and predicted classes. The comparison of the number of correct (129-FSRQs and 261-BL Lacs) and incorrect (28-FSRQs and 26-BL Lacs) predictions shows that the model classifies BL Lacs and FSRQs perfectly. Other ways to analyze

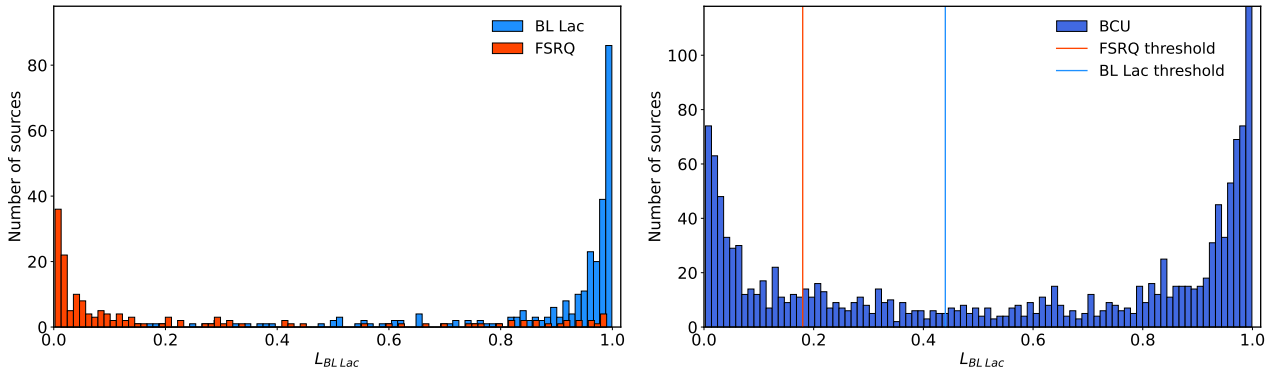

Figure 2.2: *Left panel:* Distribution of the likelihood to be BL Lac (blue) or FSRQ (orange) for the sources in the test sample. *Right panel:* Distribution of the likelihood of 1420 BCUs to be BL Lac or FSRQ candidates.

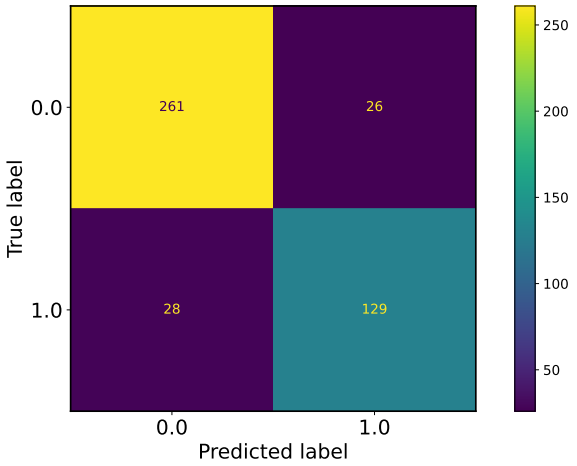

Figure 2.3: The confusion matrix of *LightGBM_opt* classifier on the test sample.

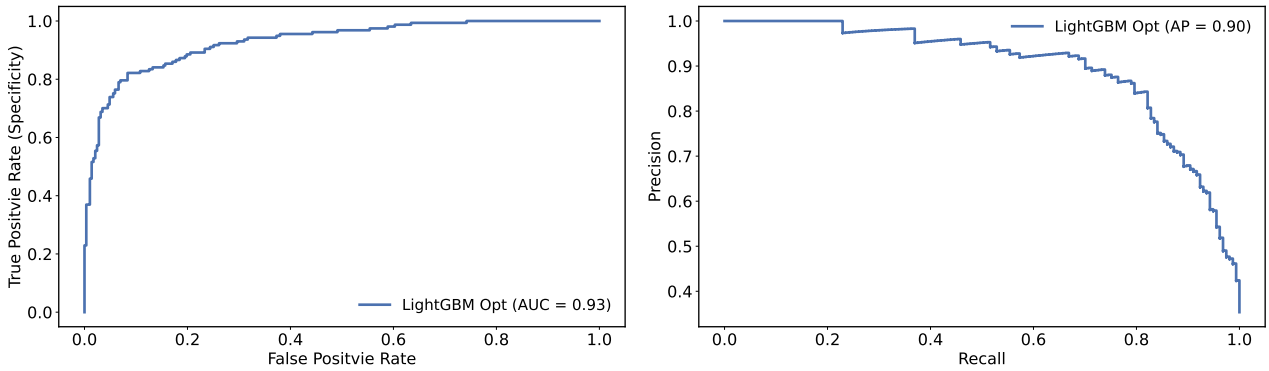

Figure 2.4: *Left panel:* ROC curve for *LightGBM_opt* classifier. *Right panel:* Precision Recall curve.

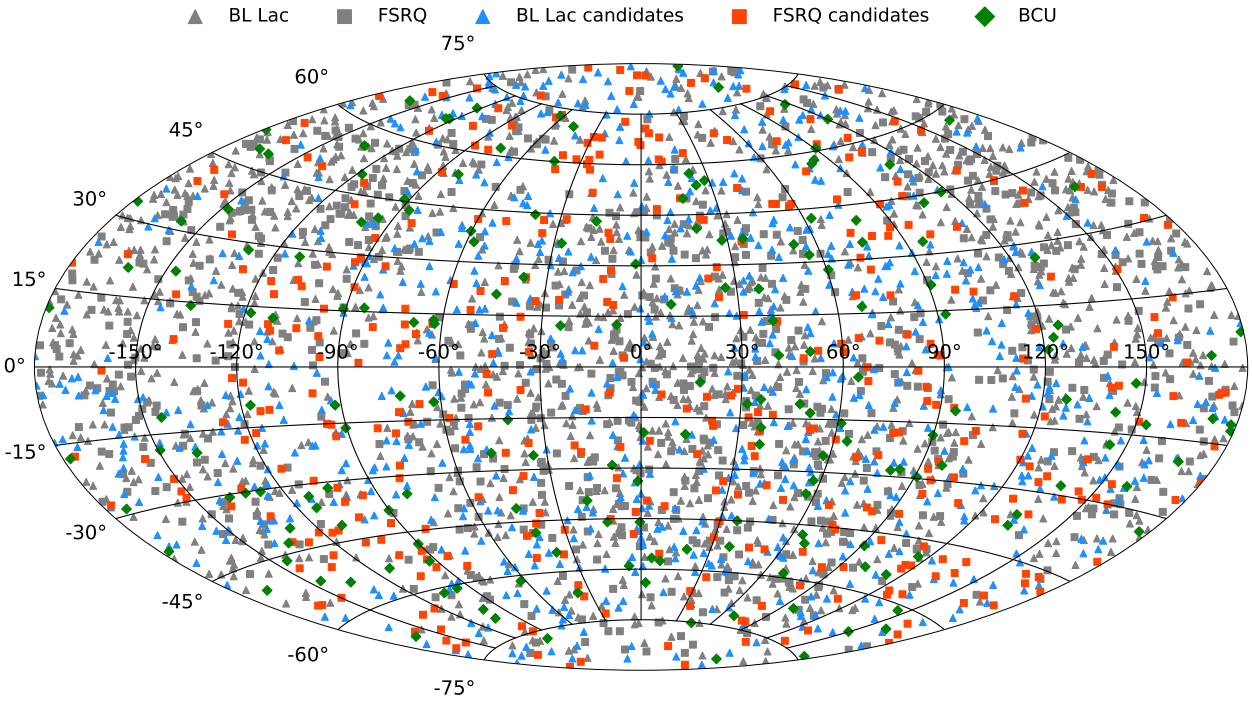

Figure 2.5: Hammer-Aitoff projection of FSRQs, BL Lacs and BCUs. The location of BL Lacs and FSRQs from 4FGL is shown with gray color while the new BL Lac and FSRQ candidates are in blue and orange, respectively.

the effectiveness of the model are Receiver Operating Characteristic (ROC) and Precision-Recall curves shown in Figure 2.4. The ROC curve (left panel in Figure 2.4) represents the graph of the true positive rate versus the false positive ones and shows the performance of the model at all classification thresholds. The Area under the ROC Curve (AUC) is a measure of the model usefulness- the higher the AUC the better the model can distinguish between BL Lacs and FSRQs; in this case AUC=0.93. The Precision-Recall curve in Figure 2.4 (right panel), the plot of the precision against the recall at a variety of thresholds, shows the trendoff between the precision and recall.

The accuracy of the network defined as positive association rate, i.e., how many BL Lacs (FSRQs) are correctly identified out of all BCUs, was optimized by selecting different classification thresholds for BL Lacs and FSRQs. The accuracy reaches 0.9 (90 %) when the classification threshold of $L_{\rm BL\,Lac} > 0.44$ identifies BL Lac candidates, while threshold $L_{\rm FSRQs} > 0.82$ identifies FSRQ candidates.

We applied the best model to the entire 1420 BCU sample in 4FGL. It is found

that 825 objects (58.1%) have likelihood above the threshold of $L_{\rm BL\,Lac} = 0.44$ and are classified as BL Lacs, 405 (28.5%) are FSRQs having likelihood above $L_{\rm FSRQ} = 0.82$, and 190 (13.3%) remain unclassified. The sky distribution of blazars locations in Galactic coordinates and Hammer–Aitoff projection is shown in Figure 2.5. The location of BL Lacs and FSRQs from 4FGL are shown with gray triangles and squares, respectively, most likely BL Lacs and FSRQs from BCUs are in blue triangles and orange squares, respectively, and the remaining unclassified BCUs are in green diamonds.

The likelihood distribution of the model applied to BCU sample is shown on the right panel of Figure 2.2. As expected, it mimics the same trend as seen for BL Lacs and FSRQs in test sample (left panel of Figure 2.2). The ratio of BL Lacs to FSRQs identified from BCUs is 2.03, similar to the result obtained in Kovačević et al. [52] which classified BCUs in *Fermi*-LAT 8-year source catalogue using ANNs. Table 2.2 shows the portion of the sources having higher probability of being BL Lacs and FSRQs; for each source the name in the catalogue, RA and Dec, detection significance (σ), energy flux and its uncertainty, and the probabilities to be BL Lac or FSRQ are reported. As it can be seen from the table, the used algorithm can classify BCUs as BL Lacs or FSRQs with a high probability. However, there are also sources with intermediate likelihoods falling in the region where the two sub-classes overlap, so they cannot be classified by the model. The full BCUs classification table that includes also the sources which have lower association likelihood is available in the online supplementary material and at the following GitHub repository[3].

The comparison of BL Lac and FSRQ candidate list presented here with the previous studies is not straightforward and rather difficult as the number of blazars and their classifications are changing in different versions of the catalogues. However, to show the accuracy of our method, we present a general comparison of our results with those presented in Butter et al. [46] where the BCUs from 4FGL DR2 (a catalogue version preceding 4FGL DR3) are classified

[3] `https://github.com/mherkhachatryan/BCU-Classification.git`

Table 2.2: List of BCUs from 4FGL with the most significant association.

Source Name	RA	Dec	Significance	Energy Flux	$L_{\rm BL\,Lac}$	$L_{\rm FSRQ}$
4FGL J1925.0+2815	291.2683	28.2643	17.84	$(6.8 \pm 0.61) \times 10^{-12}$	0.9989	0.0011
4FGL J1958.1+2438	299.5284	24.6417	11.24	$(6.6 \pm 0.94) \times 10^{-12}$	0.9986	0.0014
4FGL J0121.7+5153	20.4389	51.8947	5.90	$(1.5 \pm 0.37) \times 10^{-12}$	0.9983	0.0017
4FGL J0538.6+0443	84.6630	4.7262	4.51	$(1.6 \pm 0.45) \times 10^{-12}$	0.9982	0.0018
4FGL J1401.1-3717	210.2971	-37.2975	10.62	$(3.1 \pm 0.47) \times 10^{-12}$	0.9980	0.0020
4FGL J1846.7+7238	281.6849	72.6371	8.04	$(1.4 \pm 0.25) \times 10^{-12}$	0.9978	0.0022
4FGL J2142.1+4501	325.5291	45.0182	6.10	$(1.8 \pm 0.39) \times 10^{-12}$	0.9976	0.0024
4FGL J0215.3+7555	33.8285	75.9190	7.26	$(1.5 \pm 0.34) \times 10^{-12}$	0.9975	0.0025
4FGL J1535.3-3135	233.8391	-31.5907	6.59	$(1.7 \pm 0.39) \times 10^{-12}$	0.9973	0.0027
4FGL J0606.5-4730	91.6416	-47.5038	13.57	$(3.3 \pm 0.38) \times 10^{-12}$	0.9972	0.0028
4FGL J0507.4-3346	76.8591	-33.7813	13.88	$(3.0 \pm 0.38) \times 10^{-12}$	0.9971	0.0029
4FGL J0954.2-2520	148.5681	-25.3384	8.47	$(2.1 \pm 0.36) \times 10^{-12}$	0.9971	0.0029
4FGL J1943.6-0533	295.9249	-5.5665	4.86	$(2.2 \pm 0.53) \times 10^{-12}$	0.9971	0.0029
4FGL J1234.0-5735	188.5194	-57.5961	29.72	$(13.5 \pm 0.99) \times 10^{-12}$	0.9970	0.0030
4FGL J0213.8-6949	33.4704	-69.8311	8.96	$(1.4 \pm 0.27) \times 10^{-12}$	0.9970	0.0030
4FGL J1412.0+3836	213.0130	38.6102	8.30	$(1.4 \pm 0.27) \times 10^{-12}$	0.9970	0.0030
4FGL J0830.1-0946	127.5427	-9.7728	7.53	$(1.8 \pm 0.36) \times 10^{-12}$	0.9970	0.0030
4FGL J1537.9-1344	234.4867	-13.7335	5.76	$(1.6 \pm 0.40) \times 10^{-12}$	0.9969	0.0031
4FGL J2142.4+3659	325.6020	36.9856	9.83	$(2.8 \pm 0.43) \times 10^{-12}$	0.9969	0.0031
4FGL J1240.4-7148	190.1160	-71.8156	21.15	$(7.7 \pm 0.61) \times 10^{-12}$	0.9969	0.0031
4FGL J0620.5-2512	95.1445	-25.2129	17.24	$(7.8 \pm 0.70) \times 10^{-12}$	0.0023	0.9977
4FGL J0900.6-7408	135.1721	-74.1440	8.25	$(3.6 \pm 0.54) \times 10^{-12}$	0.0028	0.9972
4FGL J2057.4-0723	314.3535	-7.3901	8.64	$(3.9 \pm 0.53) \times 10^{-12}$	0.0033	0.9967
4FGL J1830.2-4443	277.5504	-44.7200	23.11	$(10.0 \pm 0.72) \times 10^{-12}$	0.0034	0.9966
4FGL J0138.6+2923	24.6637	29.3855	7.20	$(2.5 \pm 0.46) \times 10^{-12}$	0.0036	0.9964
4FGL J0616.7-1049	94.1761	-10.8230	6.02	$(5.1 \pm 1.11) \times 10^{-12}$	0.0037	0.9963
4FGL J0732.7-4638	113.1774	-46.6488	11.17	$(4.9 \pm 0.97) \times 10^{-12}$	0.0037	0.9963
4FGL J0953.1-3005	148.2779	-30.0979	10.08	$(3.5 \pm 0.51) \times 10^{-12}$	0.0041	0.9959
4FGL J0841.0-2744	130.2630	-27.7468	6.09	$(2.6 \pm 0.54) \times 10^{-12}$	0.0043	0.9957
4FGL J0348.8+4610	57.2185	46.1695	6.51	$(3.6 \pm 0.94) \times 10^{-12}$	0.0046	0.9954
4FGL J2139.9+3910	324.9929	39.1711	3.72	$(2.6 \pm 0.67) \times 10^{-12}$	0.0050	0.9950
4FGL J0008.0-3937	2.0048	-39.6320	5.44	$(2.1 \pm 0.41) \times 10^{-12}$	0.0052	0.9948
4FGL J1437.3-3239	219.3259	-32.6569	5.17	$(1.7 \pm 0.53) \times 10^{-12}$	0.0053	0.9947
4FGL J0118.7-0848	19.6884	-8.8080	7.56	$(2.7 \pm 0.43) \times 10^{-12}$	0.0053	0.9947
4FGL J2141.7-6410	325.4305	-64.1792	65.83	$(25.0 \pm 0.78) \times 10^{-12}$	0.0054	0.9946
4FGL J1821.6+6819	275.4034	68.3242	34.47	$(12.1 \pm 0.86) \times 10^{-12}$	0.0055	0.9945
4FGL J0429.0-0006	67.2549	-0.1006	3.39	$(2.3 \pm 0.63) \times 10^{-12}$	0.0055	0.9945
4FGL J0501.0-2423	75.2732	-24.3935	5.11	$(3.5 \pm 0.72) \times 10^{-12}$	0.0059	0.9941
4FGL J2318.2+1915	349.5568	19.2560	13.17	$(6.2 \pm 0.56) \times 10^{-12}$	0.0059	0.9941
4FGL J1421.6-4819	215.4125	-48.3317	6.61	$(3.8 \pm 0.85) \times 10^{-12}$	0.0059	0.9941

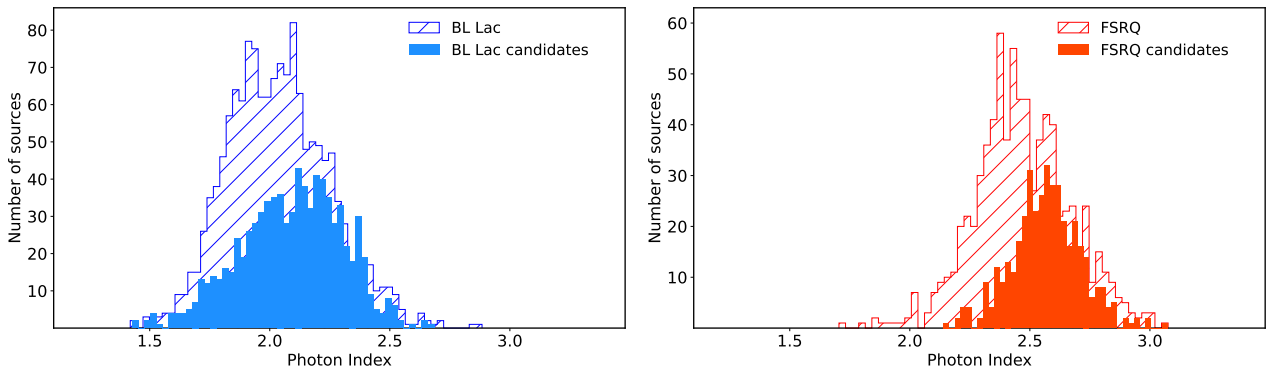

Figure 2.6: The power-law photon index distribution of BL Lacs (left) and FSRQs (right) in 4FGL. The distributions are compared with newly classified BL Lac and FSRQ candidates (filled histograms).

using Bayesian neural networks. Applying tight selection criteria, their list contains 429 BL Lacs and 178 FSRQs. Among their BL Lac candidates 355 (82.7%) objects are in agreement with our prediction and we found a difference in 74. Among those 74, in 4FGL DR3 53 objects have already been classified as BL Lacs, 2 as FSRQs and 1 as normal galaxy; 13 objects were dropped by us because of insufficient spectral data (see Section 2.3). So disagreement is found only with 5 objects: all remained unclassified. Similarly, out of 178 FSRQs in their list, 148 (83.1%) match with our results; from the remaining 31 sources in 4FGL DR3 4 have already been classified as FSRQs and 2 are missing, we excluded 6 objects, 13 objects remained unclassified with a probability between $L_{\rm BL\,Lac} = 0.18 - 0.44$ and we found disagreement for 5 objects. Similar picture can be drawn when comparing with the BL Lac and FSRQ list by applying loose selection criteria. Thus, our results are in a good agreement with those presented in Butter et al. [46] and obtained by a different method.

2.4.1 BL LAC AND FSRQ CANDIDATES VERSUS BL LACS AND FSRQS

The idea of the classification presented in the previous subsection is to identify new BL Lac and FSRQ candidates among the unclassified blazars. In this subsection, we compare and contrast the properties of newly identified and known sources.

The spectral difference between BL Lacs and FSRQs in 0.1-300 GeV band is well known. The distribution of power-law photon indexes of BL Lacs and FSRQs from 4FGL are shown in Figure 2.6 left and right panels, respectively (blue and orange shaded areas). The mean and standard deviation of these distributions is 2.03 ± 0.21 for BL Lacs and 2.47 ± 0.20 for FSRQs; on the average, BL Lacs spectra are harder than those of FSRQs. The distribution of newly classified BL Lac and FSRQ candidates is shown by filled blue and orange areas in the left and right panels of Figure 2.6, respectively. The distribution of likely BL Lacs and FSRQs is centered on 2.09 ± 0.21 and 2.57 ± 0.14, respectively, in an excellent agreement with the distributions of known BL Lacs and FSRQs. Thus, BL Lacs and FSRQs

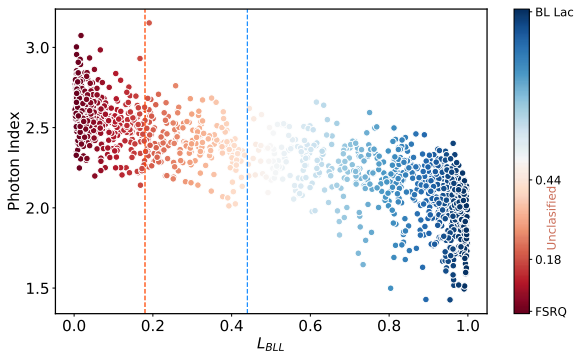

Figure 2.7: Photon index versus the probability. The color bar shows the probabilities of source associations: FSRQs are in dark red and BL Lacs in dark blue.

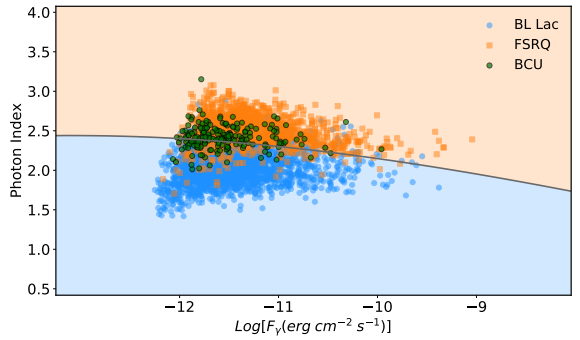

Figure 2.8: Photon index versus energy flux above 100 MeV. The curve represents the approximate boundary of two sub-classes separation.

classified from BCUs have similar spectral characteristics as compared with those derived for known sources. As the power-law index was not considered in the model training, this comparison is an effective way to illustrate the power of our method.

Another way to visualize the power-law photon index difference between BL Lacs and FSRQs is to plot the photon index versus $L_{\rm BL\,Lac}$ (Figure 2.7). There is a clear correlation between the photon index and probability; higher $L_{\rm BL\,Lac}$ corresponds to lower index and vice-versa. This very well follows the spectral trend observed for BL Lacs and FSRQs, namely higher $L_{\rm BL\,Lac}$ (more likely BL Lacs) corresponds to harder spectra while FSRQs (lower $L_{\rm BL\,Lac}$) appear with softer spectra.

Vertical blue and orange dashed lines show the classification threshold defined for BL Lacs and FSRQs. 57.2 % of total BCUs are classified as BL Lacs (right region from the blue dashed line in Figure 2.7) and 28.9 % are FSRQs (left region from the orange dashed line in Figure 2.7). The sources falling between

the orange and blue dashed lines (13.9 %) remain unclassified, their power-law index is in the range defined for BL Lacs and FSRQs.

The increased number of BL Lacs and FSRQs (2261 and 1188, respectively) allows to compare their properties with improved statistics. A convenient way to compare the properties of different blazar classes is through plotting the power-law photon index versus the flux (Figure 2.8). Since the spectra of some sources deviate from the simple power-law model, we computed the energy flux between 100 MeV and 100 GeV using the power-law model parameters given in 4FGL, namely, reported flux density, pivot energy and power-law photon index. The BL Lacs and FSRQs both from 4FGL and classified from BCUs are shown in blue and orange, respectively and the remaining unclassified BCUs are in green. The reported energy fluxes vary from 5.62×10^{-13} erg cm^{-2} s^{-1} to 9.06×10^{-10} erg cm^{-2} s^{-1} while the photon index is in the range from 1.42 to 3.08. A Kolmogorov–Smirnov test gives a probability of 0.31 that FSRQs and FSRQ candidates come from the same parent population and the probability is 0.15 for the BL Lacs and BL Lac candidates. From the distribution it is possible to quantify the space occupied by BL Lacs and FSRQs in the photon index versus energy flux plane. The boundary between these two classes (decision boundary) was found by using Gaussian naive Bayes classification. The black line in Figure 2.8 is the decision boundary, which corresponds to the curve that optimally separates the two classes. In other words, by computing the probabilities the algorithm optimally divides the plane in a such way as to have the highest number of BL Lacs and FSRQs below and above the line, respectively. The boundary line defines $\simeq$ 2.41, 2.31 and 2.15 indices at 10^{-12} erg cm^{-2} s^{-1}, 10^{-11} erg cm^{-2} s^{-1} and 10^{-10} erg cm^{-2} s^{-1} fluxes, respectively, well separating the two-classes: 91.2 % of BL Lacs occupy the region below the line while 86.1 % of FSRQs are above. The remaining BCUs (green circles in Figure 2.8) are distributed above and below the limit; 65.1% of BCUs occupy the space more characteristic for FSRQs, while 34.9 % show properties more similar to BL Lacs. The limit presented in Figure 2.8, which is a physical distinction between

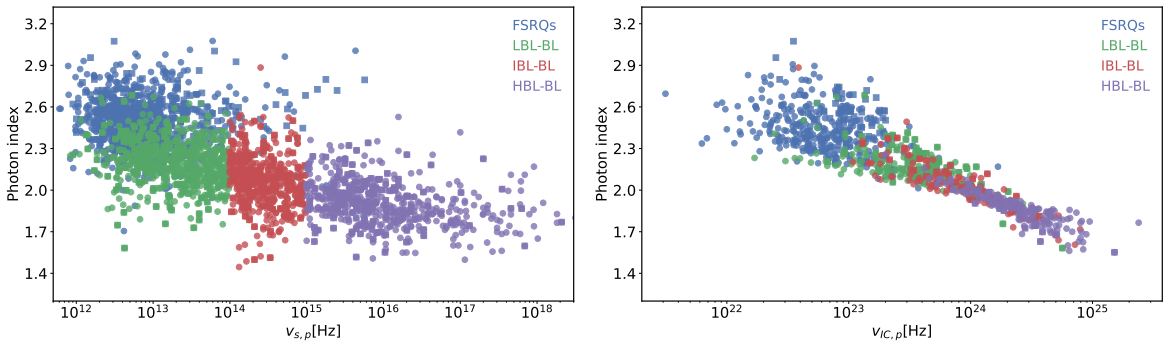

Figure 2.9: *Left panel:* γ-ray photon index versus the synchrotron peak frequency. *Right panel:* γ-ray photon index versus the inverse Compton peak frequency. The FSRQs, LBLs, IBLs and HBLs are in blue, green, red and purple, respectively. BL Lacs and FSRQs from 4FGL are shown with circles, while BL Lac and FSRQ candidates are with squares.

the two classes of blazars, BL Lacs and FSRQs, based on photon index and flux, was obtained using a large number of BL Lacs and FSRQs, 3449 in total. The accuracy of Gaussian naive Bayes classification is 90% implying the line satisfactorily well separates the two classes of blazars. Even if this is not a strict limit, it still can be used as a reference limit for BL Lac and FSRQ division.

It is also interesting to compare the photon index with the frequency of the synchrotron peak ($\nu_{\rm s,p}$). In the previous studies, a strong anticorrelation between these two parameters was already reported [e.g., 47, 57]. Now, with updated number of BL Lacs and FSRQs tighter constraints on the photon index distribution on different blazar types can be obtained [4]. Figure 2.9 (left panel) shows the photon index versus $\nu_{\rm s,p}$ where BL Lacs are separated into LBL, IBL and HBL classes. We note that also FSRQs are mostly LBLs, but we show and discuss their properties by separating them from BL Lacs that are classified as LBLs, IBLs and HBLs. For the FSRQs (blue), LBLs (green), IBLs (red) and HBLs (purple) the mean and rms of the photon index are 2.49 ± 0.18, 2.20 ± 0.16, 2.06 ± 0.18 and 1.90 ± 0.16, respectively. As expected, the distributions of FSRQs and LBLs are similar but LBLs have a slightly harder γ-ray photon index, but, clearly, as compared with them IBLs and HBLs occupy a different region in the γ-ray photon index $\nu_{\rm s,p}$ plane; the γ-ray photon index becomes smaller (harder) from FSRQs

[4] We note that for a more meaningful comparison, $\nu_{\rm s,p}$ should be corrected by a factor of $1+z$ but this will reduce the source sample size, as z is not measured for many sources.

to HBLs, $\Gamma_{\gamma,\mathrm{FSRQs}} > \Gamma_{\gamma,\mathrm{LBLs}} > \Gamma_{\gamma,\mathrm{IBLs}} > \Gamma_{\gamma,\mathrm{HBLs}}$.

The distribution of the high energy peak frequency (referred as inverse-Compton peak $\nu_{\mathrm{IC,p}}$) for the considered sources is shown in Figure 2.9 (right panel). This is a new parameter available in the fourth catalog of AGNs detected by *Fermi*-LAT - Data Release 3 [58] which has been estimated by fitting the significantly curved spectrum with a log-parabolic model. For the current study, we excluded all the sources for which the uncertainty on the high energy peak estimation is large (requiring the value to be larger than $1.5\times$ error) which resulted in 893 blazars with measured $\nu_{\mathrm{IC,p}}$, among which 369 are FSRQs, 217 are LBLs, 143 are IBLs and 164 are HBLs. The distributions of LBLs, IBLs and HBLs overlap and are slightly separated from FSRQs toward higher frequencies. The fit of the linear function $\Gamma_\gamma = \Gamma_0 + \alpha \times \nu_{\mathrm{IC,p}}$ yields $\alpha = -0.21 \pm 0.02$ and $\alpha = -0.31 \pm 0.01$ for FSRQs and BL Lacs (considering all LBLs, IBLs and HBLs), respectively. This shows that Γ_γ of BL Lacs becomes steeper with increasing $\nu_{\mathrm{IC,p}}$.

The comparison of synchrotron ($\nu_{\mathrm{s,p}}$) and high energy ($\nu_{\mathrm{IC,p}}$) peak frequencies estimated for different blazar sub-classes is shown in Figure 2.10. In general, the $\nu_{\mathrm{IC,p}}$ of FSRQs is at lower frequencies than those of BL Lacs which in their turn show different tendencies for LBLs, IBLs and HBLs. $\nu_{\mathrm{IC,p}}$ increases along with the increase of $\nu_{\mathrm{s,p}}$; the linear fit ($\nu_{\mathrm{IC,p}} = \nu_0 + \kappa \times \nu_{\mathrm{s,p}}$) for BL Lacs shows a slope of $\kappa = 0.33 \pm 0.01$. Only 10.1% of LBLs have $\nu_{\mathrm{IC,p}}$ above 10^{24} Hz, while the percentage is 41.2% for IBLs and 89.0% for HBLs. The difference between the FSRQs and BL Lacs as well as between LBLs, IBLs and HBLs is expected from simple theoretical considerations. Within a simple one-zone synchrotron/synchrotron-self Compton (SSC) model, which is successfully applied to model the SEDs of BL Lacs [e.g., see 12], assuming Thomson regime for the inverse Compton scattering, $\nu_{\mathrm{s,p}}$ and $\nu_{\mathrm{IC,p}}$ are linked by $\nu_{\mathrm{IC,p}}/\nu_{\mathrm{s,p}} = 4/3(\gamma_{\mathrm{p}}^{\mathrm{SSC}})^2$. So, it is natural that for the sources with higher synchrotron peak (HBLs) also $\nu_{\mathrm{IC,p}}$ is at higher frequencies. However, the $\nu_{\mathrm{s,p}}$ and $\nu_{\mathrm{IC,p}}$ relation is not valid for the FSRQs, where the high energy emission is most likely due to inverse Compton scattering of external photons (UV and IR external radiation

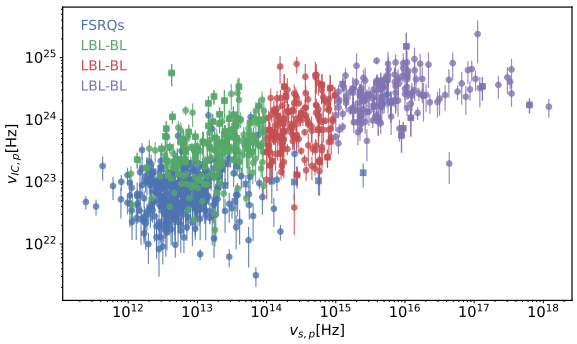

Figure 2.10: The synchrotron peak frequency ($\nu_{\rm s,p}$) as a function of the high energy peak frequency ($\nu_{\rm IC,p}$). The same color code and plot markers as in Figure 2.9.

fields which usually dominate over the jet synchrotron emission), so the $\nu_{\rm IC,p}$ scales with the average energy of up-scattered photons and bulk Lorentz factor of the emitting region.

2.5 SUMMARY

In this work, we performed machine learning classification of blazar candidates of uncertain type. By training and constructing predictive models which forecast the likelihood of a source to belong to a particular class of blazars, the classification of BCUs based on their direct observable spectral and temporal properties in the γ-ray band is conducted.

The models were trained on the set of γ-ray parameters (spectra and light curves) of BL Lacs and FSRQs from the latest and most detailed γ-ray catalog (4FGL DR3) which is based on accumulation of data in twelve years (2008-2022). Different machine learning algorithms were applied to classify blazars by dividing the entire data set into 80% and 20% train and test subsets and performing 15 fold cross validation. The algorithms based on gradient-boosted decision trees are preferred and outperform the other models because the available data set is comparatively small and contains missing data points. As a result, *LightGBM*- a state-of-the-art classification model based on gradient boosted trees shows the highest performance with a weighted recall of 0.88 and precision of 0.88.

The best model was applied to 1420 BCUs included in 4FGL to obtain the probability of their association to one of the blazar sub-classes and address the

question of their nature. As a result, among the BCUs 825 (58.1%) are BL Lac candidates, 405 (28.5%) are FSRQ candidates and only 190 (13.3%) cannot be classified by our model. The γ-ray spectral properties (e.g., power-law photon index) of already classified and BL Lac and FSRQ candidates are in an excellent agreement, showing the validity of our model.

The results of BCU classification reported here although cannot conclusively give the type of a BCU but they can be useful for statistical population studies or for planing optical monitoring of blazars. For example, the distributions of BL Lacs and FSRQs from a more complete list show clustering in the photon index and energy flux plane, clearly separating those two sub-classes. According to this criteria, the majority of BCUs (65.1%) that remained unclassified in our model show properties more similar to FSRQs. For a larger blazar sample, the distribution of the synchrotron peak frequency ($\nu_{\rm s,p}$) versus the γ-ray photon index confirms the strong difference between FSRQs and BL Lacs as well as between LBLs, IBLs and HBLs. In the distribution of the high energy peak frequency versus the γ-ray photon index most of the FSRQs occupy the region of $\Gamma_\gamma > 2.3$ and $\nu_{\rm IC,p} < 10^{23}$ Hz whereas $\nu_{\rm IC,p}$ of BL Lacs can reach higher frequencies with harder γ-ray photon index, however no distinction between LBLs, IBLs and HBLs sublasses is possible. Instead, the comparison of $\nu_{\rm s,p}$ and $\nu_{\rm IC,p}$ shows a remarkable difference between FSRQs and BL Lacs as well as between LBLs, IBLs and HBLs. The BL Lacs have much larger $\nu_{\rm IC,p}$ with a mean of 1.6×10^{24} Hz as compared with that of FSRQS with 1.1×10^{23}; 43.3% of BL Lacs have a peak above 10^{24} Hz. Among BL Lacs, HBLs have higher $\nu_{\rm IC,p}$ (for 89.0% of HBLs $\nu_{\rm IC,p} \geq 10^{24}$ Hz) whereas it is lower for LBLs; the linear fit shows a slope of 0.33 ± 0.01, so $\nu_{\rm IC,p}$ increases with $\nu_{\rm s,p}$. Such a correlation is in agreement with expectations from one-zone synchrotron-self-Compton scenarios.

3 MODELING BLAZAR BROADBAND EMISSION WITH CONVOLUTIONAL NEURAL NETWORKS - I. SYNCHROTRON SELF-COMPTON MODEL

3.1 INTRODUCTION

Blazars are emitting across the full electromagnetic spectrum, from radio bands to HE and sometimes VHE γ-ray bands, with the SED usually showing two broad components [2]. The low-energy bump is commonly interpreted as synchrotron radiation from relativistic electrons in the jet, while the origin of the high-energy component is more model dependent. In leptonic scenarios, it is assumed to arise from inverse-Compton scattering, either of synchrotron photons generated inside the jet itself in the SSC picture or of external photon fields in external-Compton models [12–22]. Hadronic models provide another look to origin of the second component, in this scenario it can be either from synchrotron emission from protons that are coaccelerated with electrons or from secondary particles generated through photo-pion and photo-pair interactions, which may also be linked to neutrino production [23–26, 59–61].

Because of this variety of physical scenarios, many numerical tools have been developed for blazar SED modeling, ranging from relatively simple leptonic implementations to more complete kinetic solvers that include particle injection, radiative cooling, and additional interaction channels [4, 11, 60–70] . In this section, we focus on the one-zone SSC case, which is widely used for BL Lacs and provides a well-defined framework in which the low-energy synchrotron component and the high-energy inverse-Compton component are generated self-consistently by the same electron population.

Even in this single case, the computational requirements for modeling blazars SEDs using fully numerical models is computationaly expensive. A kinetic SSC model requires solving coupled equations for electrons and photons, including cooling, emission, scattering, and pair-production effects. As a result, direct fitting is slow because the full transport problem must be solved repeatedly during parameter exploration. This is even more difficult for large source

samples or time-resolved SED studies, where the computational cost can prevent a thorough scan of the parameter space.

To make large-scale modeling computationally feasible, a new method based on a neural network is developed. In this approach, the full time-dependent SSC calculations are replaced by a neural-network surrogate trained on a large set of synthetic spectra generated with *SOPRANO* [61], a kinetic code that computes the radiative output of the emitting region self-consistently. A CNN is therefore trained to act as a fast emulator of the kinetic model, reproducing its output while reducing evaluation time by orders of magnitude [3]. As a result, broadband spectra can be modeled efficiently within a Bayesian framework while preserving the connection to the underlying physical calculation.

3.2 THE MODEL: SYNCHROTRON SELF-COMPTON

3.2.1 MODEL DESCRIPTION

In this work, we focus on modeling the emission from BL Lacs within the framework of the SSC model, for which the low-energy bump is attributed to the synchrotron emission of relativistic electrons, while the second peak arises from the inverse Compton scattering of the synchrotron photons on the same electron population. This model successfully reproduces the observed multiwavelength spectrum as well as the observational features in different bands, and is widely adopted for modeling the observed data from optical to the VHE γ-ray bands.

In the one-zone SSC model, it is assumed that the emission originates from a spherical region of the jet (referred to as a 'blob') with a comoving radius R, which moves with Lorentz factor Γ. We assume that the observers sees the jet at angle $1/\Gamma$, such that the Doppler boost factor $\delta \equiv \Gamma$. The magnetic field B inside this region is assumed to be homogeneous and constant. Electrons, once injected into this region, lose their energy under the effect of the magnetic field as well as by interacting with the local photon fields, ultimately generating the observed broadband spectrum.

Despite the likely presence of protons in the jet, for the SSC model, we

assume that only electrons are accelerated and radiate once injected in the radiation zone. The electron injection function and its luminosity normalization are defined by Equations 1.4 and 1.5. The temporal evolution of the electron distribution is obtained by solving the Fokker-Planck diffusion equation, while the evolution of photons is described by an integro-differential equation. We label the distribution function of photons by N_γ, and that of electrons by N_e. With the photon energy denoted as x, the kinetic equations are

$$\begin{cases} \dfrac{\partial N_e}{\partial t}(\gamma) = \dfrac{N_e}{t_{\text{esc}}} + \dfrac{\partial}{\partial \gamma}\left[(C_{\text{IC}} N_\gamma + C_{\text{sync}}) N_e \times\right] + Q_{\gamma\gamma\to e^+e^-}, \\ \dfrac{\partial N_\gamma}{\partial t}(x) = \dfrac{N_\gamma}{t_{\text{esc}}} + Q_{\text{sync}} + R_{\text{IC}} N_\gamma - S_{\gamma\gamma\to e^+e^-}, \end{cases} \tag{3.1}$$

where $t_{\text{esc}} = t_{\text{dyn}} = R/c$ is the escape time, so the first term on the right-hand side of each equation accounts for the escape of particles from the radiation zone. The coefficients C_{IC} and C_{sync} describe inverse Compton and synchrotron cooling, $Q_{\gamma\gamma\to e^+e^-}$ and $S_{\gamma\gamma\to e^+e^-}$ are the source and sink terms associated with pair creation, and R_{IC} is the redistribution kernel of Compton scattering. Synchrotron self-absorption is not included in the present analysis because it is not yet implemented in *SOPRANO*. More details on the kinetic equations and their numerical solution are given in Gasparyan et al. [61], where the explicit expressions for the different rates can also be found.

In this work, we employ *SOPRANO* [61] to solve the set of coupled kinetic equations as defined in Equation 3.1. We obtain the equilibrium solution to the kinetic equations (3.1) by evolving the system in time until $t = 4t_{\text{dyn}} = 4R/(\delta c)$. Our experiences show that further time evolution does not significantly alter the distribution functions; hence, we designate these as equilibrium distributions. These distributions serve as the final output from *SOPRANO* and are subsequently used to train the CNN.

3.2.2 MODEL LIMITATIONS

The model we use in this study is rather simple and has several limitations, in addition to the obvious constraints related to jet geometry. These limitations

are listed in this subsection. First, we assume that the emission originates from a localised (meaning at a given radius) steady system in equilibrium, without considering the dynamics of the jet. This is implied by our explicit choice to evolve the equation until a few times the dynamical time and by our consideration of the escape of particles from the radiation zone. We chose this assumption for its simplicity and because the final solution to the equation does not depend on an additional ad hoc parameter, namely the time at which the simulation stops. This assumption physically requires that any variation of the flux should happen on a time longer than $4t_{\rm dyn}$. In other word, the model is suitable to study steady state emission of blazar. The model can be also used to study blazar flares, considering that in this case the spectral evolution is neglected.

Another limitation of the model is given by the assumption of electron injection into the radiative zone after their *impulsive* acceleration, *i.e.* on a time scale $t_{\rm acc} \ll t_{\rm dyn}$. Additionally, we do not consider particle acceleration in the radiative zone, see e.g. Tramacere et al. [64]. This assumption has important consequences, as it prevents us from studying models in which the maximum electron Lorentz factor is determined by the interplay between acceleration and radiative cooling in the radiation zone. Although this effect could be considered in future studies, it would require to compute a new training set, as explain below. Such a requirement applies to any modification of the model, whether it involves the inclusion of new processes, like electron acceleration, or new constraints, such as a modified cooling rate due to field anisotropy [see, for example, 71, 72].

Finally, the current model does not consider self-consistent evolution of the magnetic field, radius and other outflow properties with observed time. This limitation is particularly significant for studying blazar flares, for which we assume an average scenario and neglect spectral evolution in this thesis. Yet, we note that the approach presented in this work can also be applied to time-dependent models, such as the Compton rocket model [73, 74] or shock evolution model [e.g. 75]. In the latter, the authors assumed that the

electron injection function is a Heaviside function, such that the particle number increases with time until injection stops, which allows them to mimic a flare. Following the work of Yan et al. [76] in the context of γ-ray bursts, we believe that time-dependent fit for blazar flares is also possible, but is outside of the scope of this thesis.

3.3 NUMERICAL MODEL: COMPUTATION AND VALIDATION

In this section, we provide details of the methodologies employed in our study to simulate spectra, which will be used as inputs to the CNN. Namely, we give details on the parameter space used for generating the SEDs via *SOPRANO*. With regards to the large number of spectra, we also provide our methodology to assess the validity of the generated spectra.

3.3.1 PARAMETER RANGES AND SAMPLING

For the SSC model considered in this thesis, there are seven free parameters: the comoving blob radius R, the Doppler factor of the emission region δ, the comoving magnetic field strength B within the emission zone, the electron luminosity L_e, the minimum Lorentz factor $\gamma_{\rm min}$, the cutoff Lorentz factor $\gamma_{\rm max}$, and the power-law index p. These parameters are inputs to *SOPRANO* which computes the resulting spectrum in a time frame ranging from several tens of seconds to a few minutes. This computational demand makes direct fits impossible due to the necessity to evaluate the model tens of thousands of times for a single fit[5]. To overcome this challenge, we developed a CNN, which we trained on a set of 2×10^5 spectra computed by *SOPRANO*. The input parameters cover the whole range of parameters relevant for an SSC model for *any* blazars. The calculation of so many spectra was facilitated by coupling *SOPRANO* as the spectrum generator with *ronswanson*—a python-based code designed for High-Performance Computing systems—as the distribution software [77]. The code *ronswanson* provides a flexible and comprehensive interface for

[5]This large number of likelihood estimations is due to the large number of parameters and is required for a full parameter exploration, for the computation of the posterior distributions and of the Bayesian factor.

constructing table models from computationally intensive simulations.

Table 3.3: Characteristics of the dataset. For each parameter, we recall its unit (if any) and symbol, and we provide its range and the distribution of the discrete parameter values. The total number of spectra is set to 2×10^5.

Parameter	Units	Symbol	Minimum	Maximum	Type of distribution
Doppler boost	-	δ	3	50	Linear
Blob radius	cm	R	10^{15}	10^{18}	Log
Minimum electron injection Lorentz factor	-	γ_{min}	$10^{1.5}$	10^5	Log
Maximum electron injection Lorentz factor	-	γ_{max}	10^2	10^8	Log
Injection index	-	p	1.8	5	Linear
Electron luminosity	erg.s^{-1}	L_e	10^{42}	10^{48}	Log
Magnetic field	G	B	10^{-3}	10^2	Log

The ranges and sampling distributions for the model parameters are detailed in Table 3.3. The Doppler boost factor varies linearly between 3 and 50, and the power-law index p is sampled linearly within the range of 1.8 to 5. We note that steep values of $p > 3$ are not expected from theory of shock acceleration or magnetic reconnection [see e.g. 78–80]. They are included so the range of p is sufficiently large to not have to deal with boundaries. Alternatively, our method allows to set p or to specify an informative prior, which can only be achieved if the model is trained on larger than expected range of the index. In contrast, the other model parameters, *i.e* the emission radius R, the minimum and maximum Lorentz factors γ_{min} and γ_{max}, the electron luminosity L_e, and the strength of the comoving magnetic field B, are sampled logarithmically within their respective ranges, such that $15 < \log(R) < 18$, $1.5 < \log(\gamma_{\text{min}}) < 5$, $2 < \log(\gamma_{\text{max}}) < 8$, $42 < \log(L_e) < 48$ and $-3 < \log(B) < 2$. This large range of the parameters guaranties that the CNN we developed will be usable for the modeling of any blazar SED.

We use Latin hypercube sampling to select the parameters of the spectra to be computed with *SOPRANO* [see *e.g.* 81, 82]. This sampling method is a widely popular technique in the creation of surrogate models as it presents several advantages. First, it allows to specify the number of simulations to be computed. As a byproduct, this method does not require to specify parameter spacing.

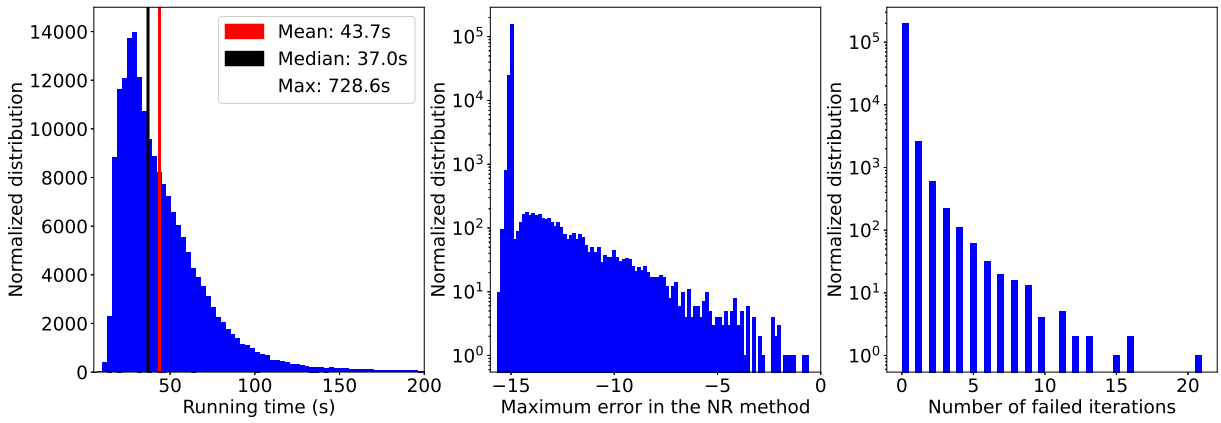

Figure 3.1: *Left panel:* distribution of the computation time for all simulations in the table model. The average compute time is 43.7s while the median time is 37s. *Middle panel:* Distribution of the maximum error in the Newton-Raphson method over the course of one simulation. We note that the ordinate is in logarithmic scale. Most of the spectra achieve the targeted relative error of 10^{-15}. On the other hand, the computation of a small fraction of spectra (1.8%) is seen to fail with a larger error. *Right panel:* number of failed time iteration by simulations, which is 0 for most of our simulations, while less than 1.8 % of our simulations have a number of failures larger than 0.

Second, it ensures uniform sampling across all parameters. Lastly, it avoids the regular sampling of parameters, which is typical in grid scan techniques. This variability in the sampling enhances the performance of the CNN, see *e.g.* [83].

3.3.2 PROPERTIES AND VALIDATION OF THE COMPUTED SPECTRA

In this section, we discuss the computational performance of *SOPRANO*, assessing the reliability of the computed spectra. Given that it is impossible to individually verify each of the 2×10^5 computed spectra, we rely on the meta-data taken for each simulations to assess the overall reliability of our numerical model. We anticipate that future implementations involving more complex models of blazar SEDs, such as external Compton or hadronic models, will necessitate even larger datasets. The validation methodology developed here will be applied in these future cases. In particular, we study (i) the time to solution ensuring it aligns with our expectations and prior experience with *SOPRANO*, (ii) the maximum error of the Newton-Raphson scheme over a simulation, and (iii) the number of times this maximum was larger than the targeted uncertainty in the computation, here set to 10^{-15}.

First, we begin by analyzing the computational time required by *SOPRANO*

for each run. The left panel of Figure 3.1 shows the the histogram of the run times for all simulations. The average simulation time is 43.7s per spectra, with a long tail extending beyond 700 seconds. These extended durations correspond to spectra characterized by a high compactness with small radius R, large electron luminosity L_e and small injection Lorentz factor $\gamma_{\rm min}$. We further note that these computation times are obtained when each independent simulations is executed on 8 cores on a AMD EPYC 7713 64-Core Processor CPU. An average computation time of ~ 40s for evolving the spectra until $4t_{\rm dyn}$ aligns with our initial expectations and previous experience with *SOPRANO*. Overall the computation of the table model with 2×10^5 spectra required ~ 20 thousand core hours, which is feasible by any dedicated server in a couple of weeks. Although it remains a moderately expensive computation, our approach present the advantage that it needs to only be performed once, if the full parameter space relevant for blazar modeling in the SSC scenario is covered.

The computation of the spectra by *SOPRANO* can fail, specifically in regions of large compactness, for which the numerical integrator currently used is not adapted. These failures originate from the implicit nature of the integration scheme, which necessitates to find the root of a non-linear systems of equations. This solution is obtained with the Newton-Raphson root finding algorithm, which can, in some instances, not converge towards the solution with the required accuracy. For the current numerical model, the accuracy of the root solver is set at 10^{-15}, close to machine accuracy. Yet, even if the required accuracy is not reached, the photons and electrons spectra are returned and the computation continued. Therefore, we computed the number of failures for each spectral computation as well as the maximum relative error on the solution.

The total number of spectra with at least one failed time iteration is 3693, constituting less than 2% of all calculated spectra. The distribution of the number of failed time bins per simulation is depicted in the right panel of Figure 3.1. The distribution of the maximum error across a full simulation is shown in the middle panel of Figure 3.1. It is evident that only a small fraction of the

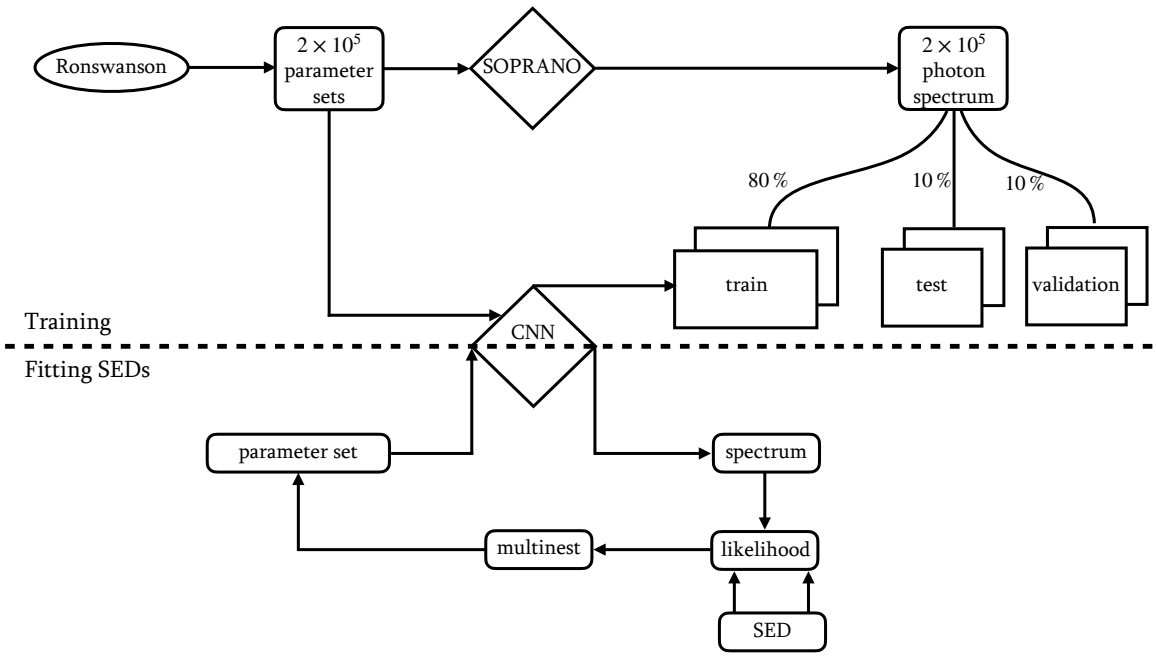

Figure 3.2: Workflow of the method proposed in this work, featuring the CNN at the center. Above the dashed line, the generation of the parameters with *Ronswanson*, the computation of the spectra with *SOPRANO* and the training of the CNN are depicted. Below the dashed line, the figure shows the CNN central to the fitting procedure, with multinest used for sampling the posterior distributions.

spectra are unreliable, with most spectra having a maximal error below 10^{-10}. We verified that the unreliable spectra are in the range of parameters space which are irrelevant for the interpretation of blazar SED.

We show in Figure 3.2 the workflow of the analysis and method used in this thesis. In this section, we presented the generation of the parameter sets with *Ronswanson*, and the corresponding spectrum computation with *SOPRANO*. This is shown on the top half of Figure 3.2, namely above the dashed line on the first row.

3.4 CONVOLUTIONAL NEURAL NETWORK

We initially attempted to directly use a table model by performing multi-dimensional linear interpolation between the input parameters to evaluate the model for any given parameter set. However, we encountered limitations in the interpolation procedure in a critical region of the spectrum, specifically at the transition between the synchrotron and SSC components. Even increasing the number of points in the table model to several millions did not resolve this issue. This transition frequently occurs in the X-ray band and must be accurately

represented for detailed analysis. Furthermore, the accurate modeling of this transition is also crucial in scenarios where neutrinos could be produced, as it constrains the maximum proton luminosity [e.g., see 11, 61, 84, 85].

To address the challenge of fitting blazar SEDs, we have developed a surrogate model utilizing a CNN. In essence, the CNN is modeling the relationship between input parameters and their corresponding spectra. Our CNN is designed to reproduce the spectra from *SOPRANO* in 150 energy bins. Before performing the training, the input parameters are detrended and their mean removed. We follow the same recipe for the spectra. However, instead of considering the 150 output independent, the mean and variance are computed for all outputs across all generated spectra. This is an essential step because these outputs are not truly independent: they collectively form a consistent spectrum. Based on our experience and trials, treating the averages and means as independent variables leads to less accurate reconstructions. Furthermore, if each output is considered independently of the other, unwanted oscillations appear in the produced spectra. This is because if each values are independent, each one can overestimate or underestimate the spectrum independently of each other. To remove these oscillations, we introduce three linear combinations that link together the 150 spectral outputs within the model, by constraining linear combinations of local neighbors. These combinations are chosen to represent the finite difference derivative at order 2 and 8, as well as the finite difference of the second order derivative at order 4. In other words, our output vector is of length 586 where

- the first 150 outputs represent the targeted spectral output,
- the next 142 outputs represent the 8^{th} order finite difference of the first derivative, multiplied by a numerical coefficient d_8^1 namely

$$\frac{df_i}{d\epsilon} = d_8^1 \left[\frac{f_{i-4}}{280} - \frac{4f_{i-3}}{105} + \frac{f_{i-2}}{5} - \frac{4f_{i-1}}{5} + \frac{4f_{i+1}}{5} - \frac{f_{i+2}}{5} + \frac{4f_{i+3}}{105} - \frac{f_{i+4}}{280} \right] \tag{3.2}$$

- the next 148 outputs represent the 2nd order finite difference approximation of the first derivative, multiplied by the coefficient d_2^1, namely

$$\frac{df_i}{d\epsilon} = d_1^1 \left[-f_{i-1} + f_{i-1} \right] \tag{3.3}$$

- the last 146 outputs represent the 4th order finite difference approximation of the second derivative, multiplied by the coefficient d_4^2 namely

$$\frac{df_i}{d\epsilon} = d_4^2 \left[-\frac{f_{i-2}}{12} + \frac{4f_{i-1}}{3} - \frac{5f_i}{2} + \frac{4f_{i+1}}{3} - \frac{f_{i+2}}{12} \right] \tag{3.4}$$

The CNN computes the 150 initial spectral outputs, and the remaining linear combinations are added in a last linear step. We find that setting the normalisation coefficients to $d_4^1 = 10$, $d_2^1 = 2$, and $d_4^2 = 4$ provides an adequate balance between (i) learning rate, (ii) accuracy of the CNN and (iii) the smoothness of the solution, specifically characterized by the absence of oscillatory behavior in the output spectra. We actually found that this method also increases the learning rate and the accuracy of the CNN.

By recursively building the CNN, we have determined that a deep network is not necessary to produce an accurate representation of our numerical model, which is computed using *SOPRANO*. Indeed, our CNN contains only 8 layers in this order: a first dense layer transform the 7 inputs to a high dimensional vector, 5 1D convolutional layer with different kernel size and stride, one maxpooling layer followed by a 1D convolutional layer and a final dense layer, mapping to the 150 outputs. This final layer of length 150 is then multiplied by the (non-square) matrix converting the 150 outputs to all outputs including the derivatives expressions. In this layer, all coefficients are known.

All these layers are followed by a ReLU activation function, apart from the maxpooling layer which is not followed by any, and the last dense linear layer, which is coupled to an activation function of type hyperbolic tangent.

In total our CNN comprises 687,815 free model parameters and is implemented using PyTorch. Our sample of spectra is split into a 80% training set, a 10% validation set and a 10% test set. We also experimented with different splits, but the results remain the same. The optimization is carried out via the NAdam algorithm, employing an epoch-dependent learning rate: 10^{-3} for the first 50 epochs, 10^{-4} for the subsequent 50 epochs, and 10^{-5} for the remaining 250 epochs. We use the L1 norm as our loss function with a sum reduction type. We find that our CNN model is straightforward to train and produces accurate results. Our CNN performances are attested by several metric scores applied on the validation set. With the inclusion of derivative expressions, the average R^2 score is 0.84 where the average is taken across all resulting spectral point plus derivatives, the mean squared error (MSE) is 0.0004, the mean absolute error (MAE) is 0.0027 and the root mean squared error (RMSE) is 0.004. In contrast, omitting the derivatives from the final score yields an average R^2 score of 0.9960, an MSE of 9.4374×10^{-6}, a MAE of 0.0013, and an RMSE of 9.4374×10^{-6}, all of which attest to the excellent performance of our CNN. The training of the CNN is represented on Figure 3.2, on the second row above the dashed line.

In Figure 3.3, the two leftmost columns display representative examples of νF_ν spectra from the training set. They are superposed with their corresponding spectra as computed by the CNN. In contrast, the two rightmost columns of Figure 3.3 feature spectra from the validation set, that is to say that were not used to train the CNN. These are also compared with their respective spectra generated by our CNN for comparative analysis. Despite a wide spread in normalization, the agreement between the original *SOPRANO* spectra and their corresponding CNN-generated spectra is remarkably high, spanning multiple orders of magnitude in both power and frequency. Notably, key features such as the synchrotron peak and the inverse Compton peak are accurately reproduced, once more attesting to the accuracy of the CNN model in reproducing the complex spectra produced from *SOPRANO*.

We note that the accuracy for some spectra is lower than for others. For

Table 3.4: Parameters describing the SEDs in Figure 3.4 and 3.7.

Parameters	Mrk 421	1ES 1959+650	1ES 1959+650
p	2.16 ± 0.04	2.12 ± 0.16	2.15 ± 0.15
$\log_{10}(\gamma_{\rm max})$	5.40 ± 0.17	6.87 ± 0.33	6.76 ± 0.36
$\log_{10}(\gamma_{\rm min})$	2.57 ± 0.17	2.56 ± 0.62	1.57 ± 0.71
δ	23.88 ± 6.54	14.13 ± 10.22	26.27 ± 7.75
$\log_{10}(B/[\rm G])$	-1.06 ± 0.22	-2.16 ± 0.49	-0.95 ± 0.33
$\log_{10}(R/[\rm cm])$	15.72 ± 0.37	16.89 ± 0.52	15.22
$\log_{10}(L_{\rm e}/[\rm erg\,s^{-1}])$	42.88 ± 0.12	43.98 ± 0.40	43.22 ± 0.30
$\log_{10}(L_{\rm B}/[\rm erg\,s^{-1}])$	41.66	41.34	40.95
	All parameters free	All parameters free	Variability time constraint

Note. The two middle columns correspond to models with all seven parameters free, while in the rightmost column, R and δ are linked through the variability time.

instance, the second and third spectra on the second line is slightly off around frequency 10^{20}Hz. We find that this happens at the boundary of the parameter space, as there is less information for the model to be train. On the other hand, these parameters are not expected to be relevant for the analysis of blazar SED, but have to be included to form regular continuous and independent parameter distributions.

3.5 MODELING THE BROADBAND SEDS OF MRK 421 AND 1ES 1959+650

To demonstrate the efficiency of our approach based on CNN in fitting and interpreting the SEDs of blazars, we model in this section the observed broadband dataset of two well-studied sources namely, Markarian 421 (Mrk 421) and 1ES 1959+650. Our analysis assumes uniform priors for the electron index p and the Doppler boost δ, and log-uniform priors for all remaining parameters, namely R, B, L_e, $\gamma_{\rm min}$, $\gamma_{\rm max}$. We assume a Gaussian likelihood and sample the posterior distributions with MultiNest [86], a nested sampling algorithm designed for efficient Bayesian inference. We assume 1000 active points and a tolerance of 0.5 to ensure efficient sampling and convergence. MultiNest offers a number of advantages, including computational efficiency and the ability to robustly handle multi-modal posterior distributions, which is a distinct possibility given the high dimensionality and complexity of the parameter space.

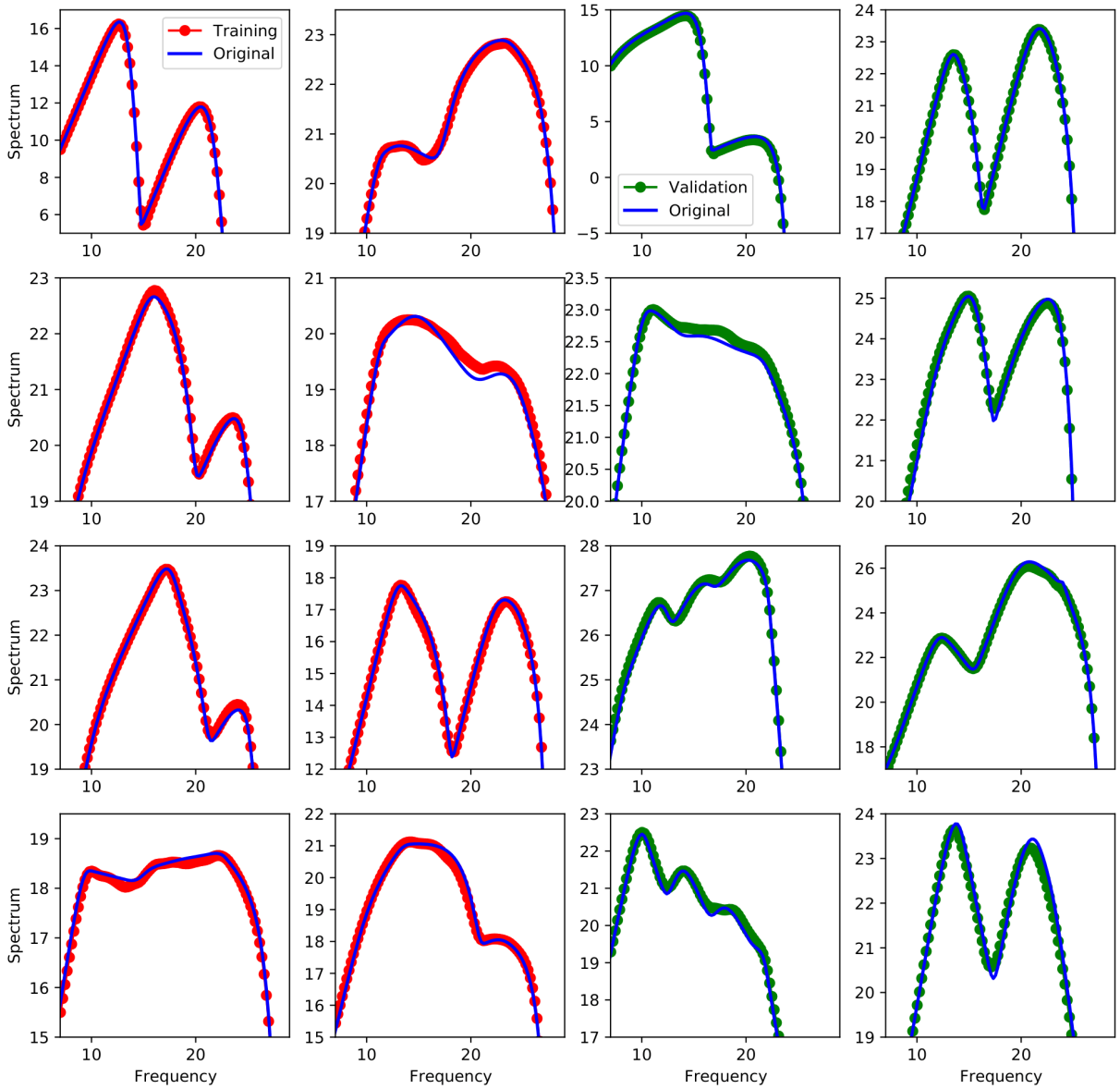

Figure 3.3: Comparison between the νF_ν spectra computed by the CNN (dots) and by *SOPRANO* (solid line) before unit conversion and expression in the observer frame. The x axis is the comoving frequency in unit of Hz. *Left Panel:* Spectra from the training set. *Right Panel:* Analogous spectra from the validation set. This figure shows the large diversity of spectra the CNN must be (and is) able to reproduce, the accuracy at which it reproduces them and the wide span of the typical emitted power across the leptonic SSC model.

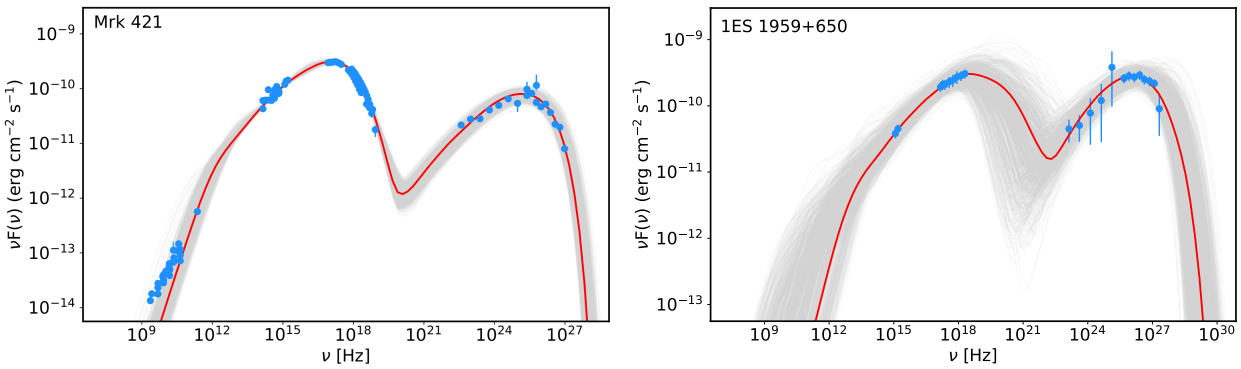

Figure 3.4: The broadband SEDs of Mrk 421 during the 4.5-month-long multi-wavelength campaign in 2009 (left) and of 1ES 1959+650 on the 14$^{\text{th}}$ of June 2016 (right). The data and its errors are in blue, the red line is the model corresponding to the best parameters, i.e., maximizing the likelihood, and the grey spectra represent one in 10 randomly selected samples from the MCM sampling, representing the model uncertainty. The data are corrected for EBL absorption.

We use the CNN as a mean to compute the spectral model for each set of parameters required by the fitting process. The result of the computation is then used by multinest to compute the likelihood and choose new sampling points. This process is depicted on the bottom half of Figure 3.2. To link together free model parameters or set them to constants, we must only specify the functional dependence between the parameters or the constants. Then, it is sufficient to modify the definition of the likelihood by specifying the parameter dependence to obtain the values of all model parameters for a set of independent parameters, such that the CNN can be used.

3.5.1 MARKARIAN 421

Located at a redshift of $z = 0.031$, Mrk 421 is one of the most extensively monitored blazars as it is the brightest blazar in the extragalactic X-ray sky. Owing to its proximity and brightness, the broadband emission features of Mrk 421 have been thoroughly investigated at all wavelengths from radio to VHE γ-rays. In 2009, a 4.5-month-long multi-wavelength campaign was conducted, yielding an unprecedented volume of simultaneous data [28]. The observed SED is presented in the left panel of Figure 3.4, where the set of data is obtained from Abdo et al. [28]. We performed a fit to the SED, excluding data below 10^{11} Hz, as emission in the radio band can be self-absorbed, implying that it is dominated by the outer regions of the jet. The best-fit parameters are listed in the left column

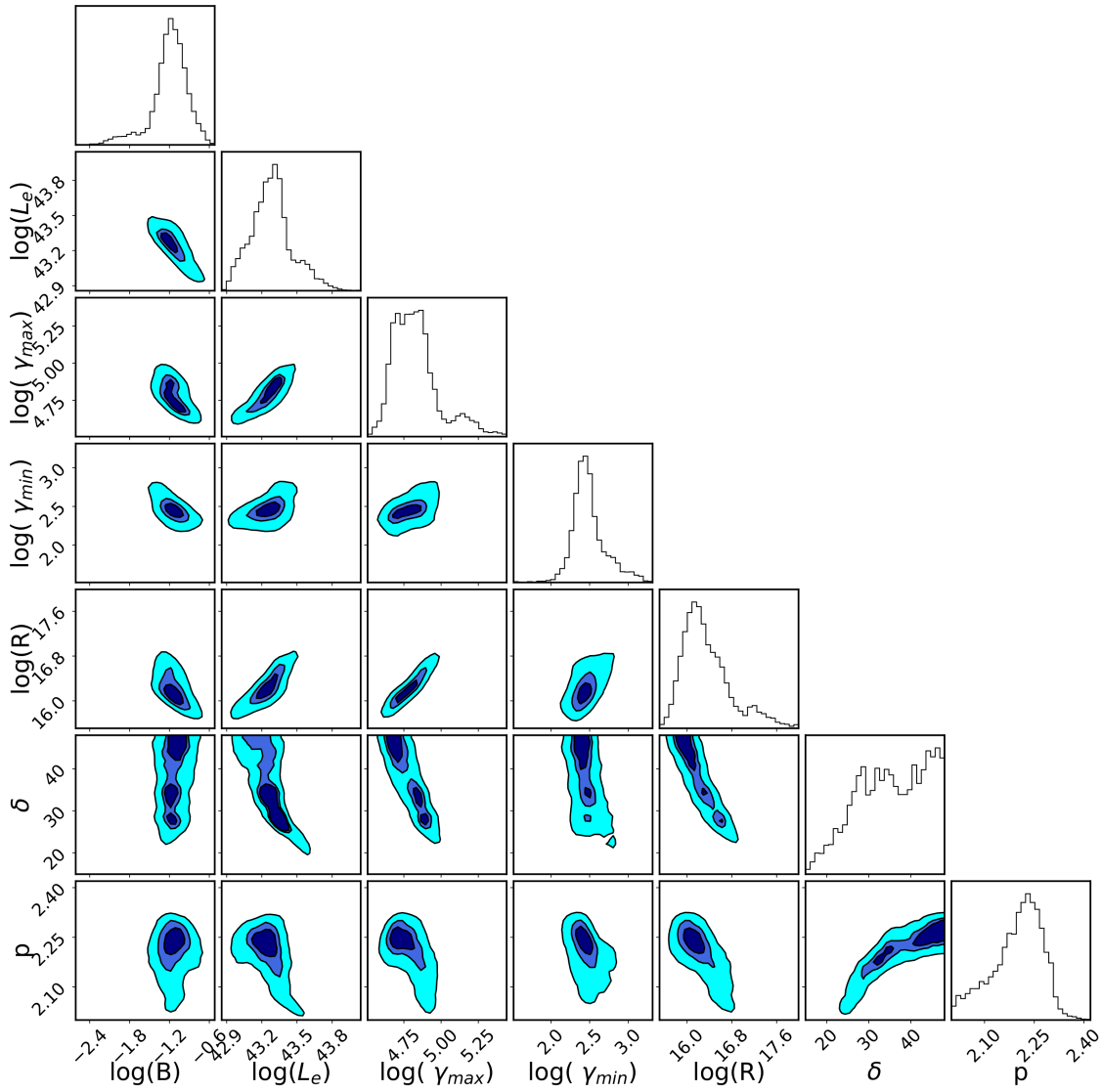

Figure 3.5: Posterior distributions for the SSC-model fit to Mrk 421.

of Table 3.4. The left panel of Figure 3.4 displays the model uncertainty in grey and the best model, based on the best-fit parameters, in red. The posterior distribution functions are provided in Figure 3.5.

The model displayed in the left panel of Figure 3.4 accurately reproduces the observed data above 225 GHz. Given the current parameter set, self-absorption dominates below 1.3×10^{13} Hz, making it impossible to model lower frequency data. The parameters we obtained are somewhat in agreement with the values determined by [28], who used a three-component power-law function to fit the broadband SED. In their model, the electron distribution between $\gamma_{\rm min} = 8.0 \times 10^2$ and $\gamma_{\rm brk,1} = 5.0 \times 10^4$ has an index of 2.2, which is consistent with our estimated value of $p = 2.16$ (for the errors see Table 3.4). In our approach the main

difference is that we achieve an acceptable fit by assuming a single electron index for the injection, which is consistently evolved under the influence of radiation cooling. In our case, the synchrotron cooling would affect the spectrum at a frequency of $\approx 5.6 \times 10^{17}$ Hz. This is above the maximum frequency defined by $\gamma_{\rm max} = 7.37 \times 10^4$ (8.5×10^{16} Hz). Consequently, an electron spectrum with a power-law index of $p = 2.16$, above $\gamma_{\rm min} = 2.10 \times 10^2$ is sufficient to reproduce the observed spectrum. Our fit indicates that the magnetic field is around $B = 6.70 \times 10^{-2}$ G, which is in agreement with the value from [28] within the uncertainties. The dissipation radius we obtained, $R = 2.96 \times 10^{16}$ cm, is somewhat close to the value estimated in their model which was derived based on the variability time. We further find that the total luminosity of the electrons, $L_{\rm e} = 2.09 \times 10^{43}\,{\rm erg\,s^{-1}}$, is of the same order of magnitude as the magnetic field luminosity $L_{\rm B} = 1.19 \times 10^{43}\,{\rm erg\,s^{-1}}$, calculated as $L_B = \pi c R^2 \delta^2 B^2 / 8\,\pi$. This suggests that the system is close to equipartition.

3.5.2 1ES 1959+650

Blazar 1ES 1959+650, at $z = 0.048$, is another bright blazar known for frequent flaring across the optical, X-ray, and TeV bands. The X-ray and γ-ray (TeV) flares often occur simultaneously, although orphan γ-ray flares have also been observed. This suggest that the same population of electrons is responsible for emissions in both bands. The source was in an active state from April to November 2016, during which the MAGIC telescopes observed major VHE γ-ray flares on June 13 and 14, as well as July 1, 2016 [87]. The multi-wavelength campaigns conducted during these flaring periods also enabled the accumulation of data across lower-frequency bands, providing a comprehensive view of the flaring activities. In this study, we focus on modeling the flare observed on the 13$^{\rm th}$ of June 2016. We retrieved the data of the flare from [87]. We note that the data are corrected for extragalactic background light (EBL) absorption. If it was not the case, our numerical model includes the possibility to incorporate EBL absorption, via the model of Domínguez et al. [88].

The fit to the data obtained during the flaring activity of 1ES 1959+650 is depicted in the right panel of Figure 3.4, and the corresponding parameter posterior distributions are provided in Figure 3.6. The best-fit parameters are summarized in Table 3.4. The data suggest that the synchrotron peak should occur at frequencies $\gtrsim 10^{20}$ Hz, enabling the X-ray data to constrain the power-law index of the electron injection function at $p = 2.26$. In contrast to the case of Mrk 421 where the X-ray data define the high-energy tail of the synchrotron component, the value of the parameter $\gamma_{\rm cut} = 2.57 \times 10^6$ is not well-constrained in this case. It is determined solely by the last data of the MAGIC spectrum, which have a large uncertainty. The interpretation of the parameter is also difficult because of the EBL effect at these high frequencies. The fit to our model constrains the magnetic field to be 2.4×10^{-2}G and the Doppler boost δ to be 22.49. The parameters p, $\gamma_{\rm cut}$, and δ are similar to those proposed by [87], but the magnetic field and the radius R differ significantly.

The dissipation radius $R = 6.69 \times 10^{16}$cm is rather large and the value of the Doppler factor is average, $\delta = 22.49$, which leads to an estimated variability time of $t_{\rm var} \sim 10^5$s, which is much longer than the reported variability time of approximately 36 min [87]. Although our fitting procedure generally treats the radius R and δ as independent variables, we can easily couple these parameters by specifying the variability timescale and removing one of them from the model parameter. To illustrate this approach, we set the radius to be $R = c\delta t_{\rm var}$ and retain δ as a free parameter. In order to not jump outside of the parameter range, the bounds on δ are changed to $\delta_{\rm min} = \max(3, R_{\rm min}/(ct_{\rm var}))$ and $\delta_{\rm max} = \min(50, R_{\rm max}/(ct_{\rm var}))$.

The fit results are illustrated in Figure 3.7, while the parameter posterior distributions are presented in Figure 3.8. The best-fit parameters are listed in the rightmost column of Table 3.4. A significant difference is observed in the value of the Doppler boost parameter, δ, which has shifted to larger values, compared to $\delta \approx 22.49$ in the previous scenario. This indicates that the compact emission region is moving at a higher velocity. Additionally, the magnetic field

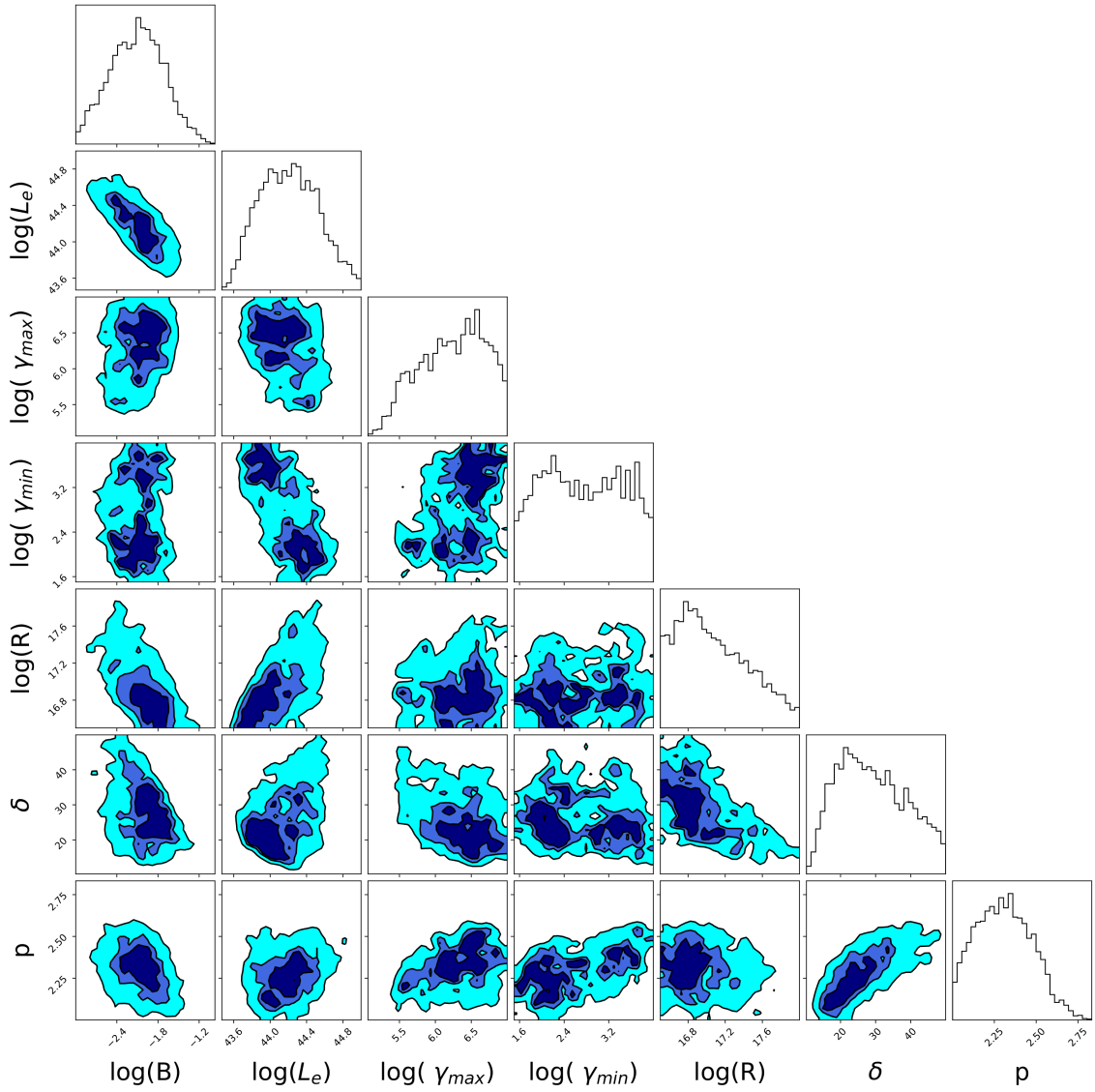

Figure 3.6: Posterior distributions for the SSC-model fit to 1ES 1959+650 with all parameters free.

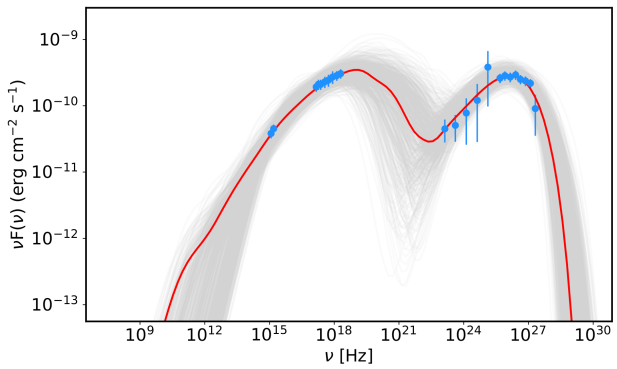

Figure 3.7: The same SED of 1ES 1959+650 as presented in Figure 3.4, but fitted with a model where R is constrained by a variability of 35 minutes.

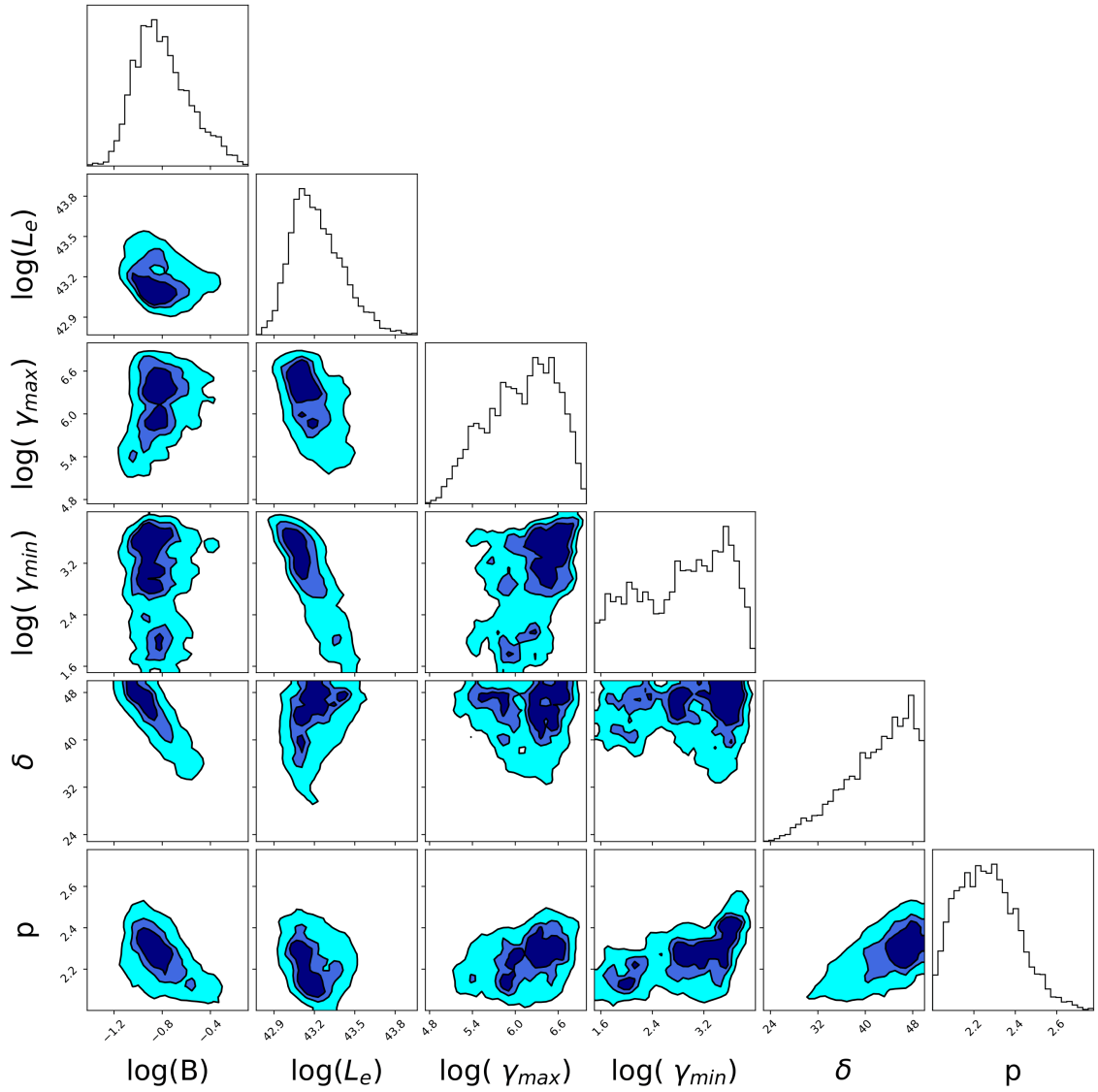

Figure 3.8: Posterior distributions for the SSC-model fit to 1ES 1959+650 with the variability-time constraint.

density in this case is larger — $B \sim 0.24$G as opposed to $B \sim 0.02$G in the previous case — which influences the electron cooling process. In the first case, synchrotron cooling is inefficient for all electrons. However, in the second case, the synchrotron cooling is efficient for the highest energy electrons, and a cooling break occurs at $\sim 2 \times 10^{17}$ Hz, resulting in the X-ray emission to be produced by cooled electrons.

3.6 SUMMARY

In this work, we presented a new approach to fit multi-wavelength SEDs of blazars with numerically intensive models. Indeed, there is a clear gap between the computational resources needed for each model evaluation and

the analysis, fitting, and detailed interpretation of multi-wavelength (and soon, multi-messenger) data for blazars. To bridge these two aspects of blazar SEDs analysis, we developed a neural network that can be trained on different computationally demanding numerical models. In this study, the CNN is trained on a large set of SSC spectra generated by *SOPRANO*, taking into account all relevant cooling processes and the pair creation process. Our surrogate model achieves high accuracy, is computed in a relatively short time $\sim$ms, includes the self-consistent cooling of the electron, and enables on-the-fly fits to data. We demonstrate the performance of the CNN by fitting the multi-wavelength observations of two BL Lac objects, namely Mrk 421 and 1ES 1959+650, thereby constraining the parameters of the SSC model and obtaining their posterior distributions.

The significant advantage of the method proposed in this work is its computational speed; the model performs fast independently of the considered physical processes and is expected to do so when hadronic processes will be included. However, a key limitation of this approach is the initial requirement for the substantial computational resources to generate the spectra needed for training the CNN. Once this initial step is completed, our methodology enables efficient and straightforward analysis of blazar SEDs. The low computational cost of the model evaluation via the CNN offers the advantage of enabling more sophisticated data fitting techniques. In future works, this efficiency will permit us to allocate computational resources for model forward-folding. Specifically, instead of using pre-analyzed data, we plan to utilize raw observational data in conjunction with the response functions of various instruments, such as *SWIFT*-XRT and *Fermi*-LAT. This integration will be facilitated through the use of 3ML [89], a framework specifically designed to combine analyses from different instruments across energy bands into a unified, coherent picture.

In this study, we trained the first CNN to accurately model the radiative signatures associated with the SSC model. This approach provides a novel framework for fitting the SED of blazars, and we intend to further apply it to

other models of blazar SEDs. Specifically, we plan to implement additional computationally intensive models based on external Compton and hadronic scenarios, for which the CNN will be trained. This set of models will facilitate the interpretation of a large variety of blazar SEDs, spanning various wavelengths, time periods, and sources.

We believe that the approach outlined in this thesis has the potential to provide significant advances of our understanding of blazars by enabling the fitting of self-consistent models to their SEDs. To facilitate broader analysis and interpretation, the model developed here will be made publicly available on the MMDC[6]. Users will be able to interact with an interface to reproduce single snapshot SEDs by specifying model parameters. Additionally, users will be able to perform fits after uploading their data (if necessary), which will provide them with the parameters that best describe the observed data, along with their posterior distributions. It should be noted that, as of the current time, this will be the only public tool available for performing fits with self-consistent model of blazar SEDs.

Not only the CNN and the associated methodology could be applied to several model of blazar as demonstrated here, but we believe that it is sufficiently general and robust to also be used in spectral and temporal analysis of γ-ray bursts prompt and afterglow phase, multi-wavelength temporal evolution of kilonovae [e.g. 90], and for the spectral interpretation of X-ray binaries.

In summary, this study represents a pioneering effort in employing CNNs for the efficient and accurate modeling of blazar SEDs. We have introduced a flexible and efficient methodology for self-consistent blazar modeling, which holds the potential for deepening our understanding of blazar physics. With the tool made publicly available through the MMDC, researchers will be able to perform state-of-the-art, self-consistent analyses of multi-wavelength—and soon, multi-messenger-data from blazar observations.

[6] http://www.mmdc.am

4 A COMPREHENSIVE VIEW OF PKS 2155-304 FROM 2008 TO 2023 THROUGH A MULTI-EPOCH MODELING OF ITS SEDS

4.1 INTRODUCTION

This section applies the modeling framework presented in Section 3 to the blazar PKS 2155-304, a high-synchrotron-peaked source at redshift $z = 0.117$ [91]. PKS 2155-304 is one of the best-studied HBL objects and shows strong variability across the electromagnetic spectrum, from hour-scale variations in the X-ray band [92] to minute-scale flares in the VHE γ-ray regime [93]. Its long observational history and rich multiwavelength coverage make it a suitable target for a time-resolved study of broadband emission.

The analysis is carried out in the context of the Modeling of time-resolved SEDs of blazars (MSED) project, which aims to study the temporal evolution of the physical conditions in blazar jets through systematic modeling of quasi-simultaneous SEDs.

The main objective of this section is to investigate how the physical properties of the emitting region in PKS 2155-304 evolve across different emission states. To do this, a large set of quasi-simultaneous SEDs is constructed from optical/UV, X-ray, and γ-ray observations, and each SED is modeled within the same one-zone SSC framework introduced earlier. This provides a homogeneous set of inferred parameters that can be compared across epochs.

Rather than concentrating on a few individual states, the analysis examines parameter distributions derived from 253 modeled SEDs and compares them across activity classes. The selected SEDs are grouped into quiescent, multiwavelength-flaring, and band-limited flaring states, allowing a systematic comparison of how changes in jet properties are associated with the broadband variability of PKS 2155-304.

4.2 DATA ANALYSIS

In investigating the multiwavelength emission of PKS 2155-304, we used data from MMDC which is an open-access platform that provides time-resolved SEDs for blazars, combining archival catalog data with newly processed observations in the optical/UV, X-ray, and γ-ray bands [30]. We note that the data can also be downloaded from the *firmamento* platform [94]. The MMDC platform also enables SED modeling within leptonic models [SSC and EIC; 3, 34]—as well as hadronic and lepto-hadronic models [95]. From MMDC, both SEDs and multi-band light curves are used to investigate the temporal evolution of the emission from PKS 2155-304. Below we present the analysis method applied to generate the data and summarize the main results; for more details on the analysis methods, we refer to Sahakyan et al. [30].

4.2.1 γ-RAY DATA

Since the launch of the *Fermi*-LAT in 2008, the γ-ray emission of PKS 2155-304 has been monitored continuously. *Fermi*-LAT is a pair-conversion γ-ray telescope sensitive to photons from 20 MeV to 300 GeV and, in survey mode, scans the entire sky approximately every three hours. A full description of the instrument is provided by Atwood et al. [36].

The analysis follows the standard *Fermi*-LAT point-source procedures and is described in detail in Sahakyan et al. [30]; the key steps are summarized here. We analyzed data from 2008 August 4 to 2023 July 4 (Mission Elapsed Time 239667417-710178221) using `Fermitools` v2.0.8 with the `P8R3_SOURCE_V3` instrument response functions. Events in the 100 MeV-300 GeV range were selected from a region of interest (ROI) of radius 12° centered on PKS 2155-304 position (RA $= 329.71^\circ$, Dec $= -30.22^\circ$). We used `evclass=128` (SOURCE class) and `evtype=3` (FRONT+BACK) events, and applied a zenith-angle cut of $< 90^\circ$ to suppress Earth-limb contamination. The source model included all cataloged γ-ray emitters within 17° of the target selected from the 4FGL incremental catalog (DR3; [10]). Parameters of sources within 12° were left free during the fit,

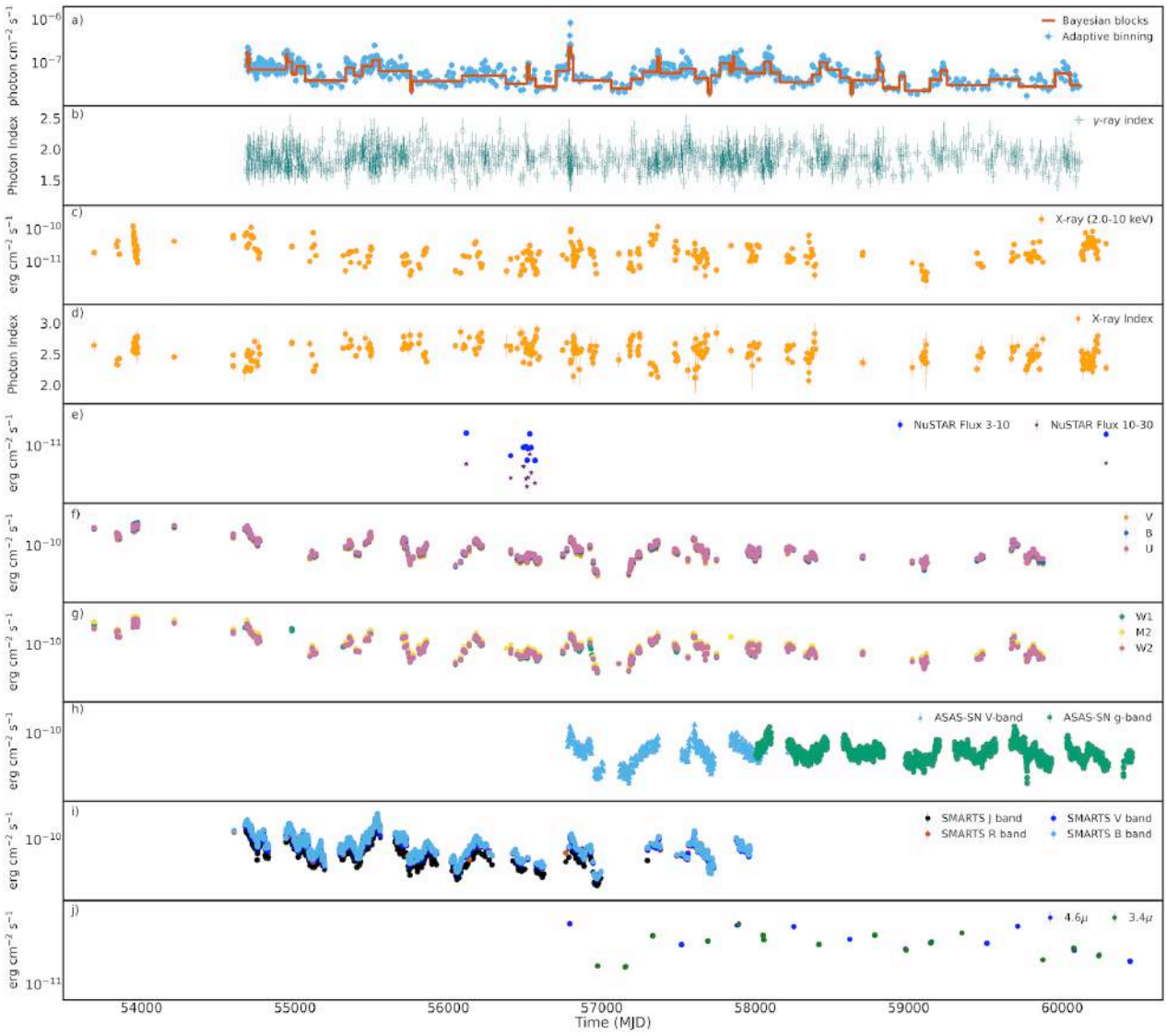

Figure 4.1: Multiwavelength light curves of PKS 2155-304. *(a)* γ-ray light curve (light-blue adaptive bins) with Bayesian-block segmentation (orange step curve) used to define time-resolved SED intervals. *(b)* γ-ray photon index. *(c) SWIFT*-XRT $2-10$ keV flux. *(d)* Photon index in different XRT observations. *(e) NuSTAR* fluxes in $3-10$ keV (blue diamonds) and $10-30$ keV (magenta pentagons). *(f) SWIFT*-UVOT U, B, V fluxes. *(g) SWIFT*-UVOT $W1$, $M2$, $W2$ fluxes. *(h)* ASAS-SN g- and V-band fluxes. *(i)* Fluxes in J, V, R, B bands from SMARTS observations. *(j)* NEOWISE $W1\,(3.4\,\mu\mathrm{m})$ and $W2\,(4.6\,\mu\mathrm{m})$ fluxes (weighted means over ≤ 10 days windows).

while those outside this radius were fixed to their catalog values. The spectra of the sources were assumed to be identical to those used in the 4FGL-DR3 catalog. The Galactic diffuse emission (`gll_iem_v07`) and the isotropic component (`iso_P8R3_SOURCE_V3_v1`) were modeled using the latest recommended templates, with the normalization of each component left free during the fit. We performed a binned maximum-likelihood analysis to optimize the spectral parameters.

Using the optimized model, we derived the γ-ray light curve of PKS 2155-304 with an adaptive-binning approach [96]. Instead of regular fixed time step, in this method the time bin width is chosen such that the relative flux uncertainty above the optimal energy ($E_{\rm opt} = 276.9$ MeV for PKS 2155-304) reaches a value of 20%. Consequently, bins are shorter during bright states and longer during quiescence. For each interval then an unbinned likelihood analysis was applied assuming a simple power-law spectrum for PKS 2155-304 (appropriate for short intervals), applying the same event selections and background components as above. The normalizations of the diffuse background models were fixed to the values derived from the full-period fit, because these components are not expected to vary. Adaptive binning has been widely used to identify and characterize flaring activity in blazars (e.g., [97–106]).

The γ-ray light curve of PKS 2155-304 is shown in Figure 4.1 (a); the corresponding photon index, Γ, is shown in Figure 4.1 (b). The light curve exhibits several episodes in which the γ-ray flux rises to $\sim 3\times$ the long-term mean of 7.32×10^{-8} photon cm^{-2} s^{-1}, e.g., near MJD 54693.5, 55517.8, 56789.0-56794.0, and 58089.6. The most prominent γ-ray outburst occurred in May-June 2014: it began around MJD 56783 (2014-05-05), peaked at MJD 56794.7 (2014-05-17), and declined by MJD 56817 (2014-06-09), for a duration of ≈ 34 days. During the peak γ-ray emission at MJD 56794.7, the flux reached 8.44×10^{-7} photon cm^{-2} s^{-1} (> 276.9 MeV) with a very hard photon index of $\Gamma = 1.47$. During this activity, between MJD 56783 and 56817, the γ-ray spectrum hardened as the flux increased and then softened toward $\Gamma \sim 2.0$ during the decay. Similar episodes—flux enhancements accompanied by spectral hardening— can be seen

in other periods as well (see Figure 4.1 a and b). However, there are also periods when the γ-ray flux increased but the γ-ray photon index did not change or even softened [e.g., MJD 54690- 54700; see e.g., 107].

4.2.2 X-RAY DATA

In the X-ray band, PKS 2155-304 has been regularly monitored by XRT on board of the *SWIFT* [35] in the 0.3-10 keV band and with the Nuclear Spectroscopic Telescope Array [*NuSTAR*; 108] in the 3-79 keV band. Their joint coverage enables soft-to-hard X-ray investigation of PKS 2155-304 emission over more than two orders of magnitude in energy.

SWIFT XRT *SWIFT*-XRT made 343 observations of PKS 2155-304 until July 4 2023. All blazar observations performed by *SWIFT* have been analyzed and processed, following the method detailed in Sahakyan et al. [30] and are made publicly available through the MMDC platform Sahakyan et al. [30]. Here we summarize main steps relevant to reducing the observational data. The data have been processed with the `swift_xrtproc` pipeline [109], which automatically downloads observation and calibration files, runs `xrtpipeline` to generate cleaned event files and exposure maps for each snapshot and the full observation, and performs standard analysis. Source and background spectra are extracted using a 20-pixel source aperture when the observation is not piled up and a source-free annulus for the background; pile-up is explicitly checked and, when present, spectra are re-extracted from an annulus with the inner radius set by the measured count rate. Ancillary response files are built with `xrtmkarf` and appropriate response matrices from CALDB. Spectra (0.3-10 keV) are fitted in XSPEC [110] with a power law model assuming a fixed Galactic absorption $N_{\rm H}$ (using *phabs* model); best-fit models are then converted to νF_ν for SED construction. Further details on `swift_xrtproc` are provided in Giommi et al. [109].

The variation of the X-ray flux (2-10 keV) and photon index ($\Gamma_{\rm X}$) in time are presented in Figure 4.1, panels c and d respectively. In the X-ray band,

several flaring episodes are evident when the flux exceeds the long-term mean of $\langle F_{2\text{-}10} \rangle \simeq 2.3 \times 10^{-11}\,\mathrm{erg\,cm^{-2}\,s^{-1}}$. The brightest flare occurred at MJD 53945 (2006-07-29), when the flux reached $(1.25 \pm 0.02) \times 10^{-10}\,\mathrm{erg\,cm^{-2}\,s^{-1}}$—a factor of ~ 5.4 above the mean—with $\Gamma_{\rm X} = 2.56 \pm 0.01$. The second-highest flux was observed at MJD 57363 (2015-12-07), $(1.21 \pm 0.15) \times 10^{-10}\,\mathrm{erg\,cm^{-2}\,s^{-1}}$, with a harder spectrum, $\Gamma_{\rm X} = 2.13 \pm 0.06$. Overall, $\Gamma_{\rm X}$ spans $\simeq 2.1$-2.9. The hardest spectrum, $\Gamma_{\rm X} = 2.07 \pm 0.07$ was observed at MJD 58347 (2018-08-17) with a flux of $(6.5 \pm 0.9) \times 10^{-11}\,\mathrm{erg\,cm^{-2}\,s^{-1}}$, whereas the softest, $\Gamma_{\rm X} = 2.90 \pm 0.10$, was measured at MJD 56578 (2013-10-13) at $(4.7 \pm 0.9) \times 10^{-12}\,\mathrm{erg\,cm^{-2}\,s^{-1}}$. These show strong spectral and flux variability in the X-ray band, with episodes of both spectral hardening and softening.

NuSTAR *NuSTAR* with its two focal plane modules, FPMA and FPMB [108] observed PKS 2155-304 11 times; nine of these observations fall within the analysis window considered here. All data of blazars that were observed with *NuSTAR*, including PKS 2155-304, are available via MMDC. Here, we summarize the main points of the analysis. The data were processed with the automated `NuSTAR_Spectra` pipeline [111], built on `NuSTARDAS`. The pipeline *i)* downloads the observations and calibration files; *ii)* generates a 3-20 keV image to derive the count rate to set extraction radii; *iii)* localizes the source with `XIMAGE`; and *iv)* runs `nuproducts` to create high-level science products. Source and background regions are chosen automatically with radii that scale with the measured count rate (typical the source radius is ≈ 30-$70''$ while the background is from an annulus separated by $\gtrsim 50''$). Then, the spectra are grouped to ≥ 1 count per bin and the data are fitted in `XSPEC` from 3 keV up to the energies when the background starts to dominate (often 20-79 keV) using Cash statistics [112] and assuming a power law model and then computing the fluxes in the 3-10 and 10-30 keV bands. Finally, X-ray SED points are computed from 3 keV up to the energies where the net source signal exceeds the local background. For more details see Middei et al. [111].

In Figure 4.1 panel (e), the variation of the fluxes in the 3-10 and 10-30 keV bands is shown displaying moderate variability, especially in the hard X-ray band. In the 3-10 keV band the flux changes from 5.6×10^{-12} to 1.7×10^{-11} erg cm^{-2} s^{-1} (mean $\approx 10^{-11}$ erg cm^{-2} s^{-1}) while in the 10-30 keV band, it varies between 2.0×10^{-12} and 7.2×10^{-12} erg cm^{-2} s^{-1} (mean 3.7×10^{-12} erg cm^{-2} s^{-1}). This corresponds to variability amplitudes of ~ 3.0 (3-10 keV) and ~ 3.6 (10-30 keV). The brightest epochs occur at MJD 56116.7 and 56530.8, where the 3-10 keV flux reached $(1.67 \pm 0.17) \times 10^{-11}$ and $(1.61 \pm 0.16) \times 10^{-11}$ erg cm^{-2} s^{-1}, respectively. The *NuSTAR* photon index spans a relatively narrow range, $\Gamma_{\rm X} = 2.58$-3.03 (mean $\langle \Gamma_{\rm X} \rangle \simeq 2.80$). The hardest spectrum, $\Gamma = 2.58$, was measured at MJD 56489.965 with 3-10 and 10-30 keV fluxes being 9.4×10^{-12} and 4.4×10^{-12} erg cm^{-2} s^{-1}, respectively. The softest spectrum, $\Gamma \simeq 3.03$, was observed at MJD 56506.939 with corresponding fluxes of 9.7×10^{-12} and 2.7×10^{-12} erg cm^{-2} s^{-1}. The soft indices in this band indicate that the *NuSTAR* band observes the declining, high-energy tail of the synchrotron component which is characteristic for HSP blazars.

4.2.3 OPTICAL/UV DATA

SWIFT-UVOT observed PKS 2155-304 in six filters in the optical (V: 500-600 nm; B: 380-500 nm; U: 300-400 nm) and ultraviolet (UVW1: 220-400 nm; UVM2: 200-280 nm; UVW2: 180-260 nm) bands providing information on the low energy component of the emission spectrum. UVOT data for all blazars observed by *SWIFT* (including PKS 2155-304) are accessible via MMDC. Here, we summarize only the main analysis steps. Data reduction was performed using an automated pipeline that follows standard UVOT analysis procedures, with photometry extracted from a $5''$ aperture centered on the target and the background estimated from nearby source-free regions (from a $20''$ region). Each image was inspected for contamination, and calibrated magnitudes were converted to fluxes using established zero-points and corrected for Galactic extinction with a reddening ratio $A_v/E(B-V) = 3.1$ and $E(B-V) = 0.019$ extracted from the Infrared Science Archive [7]. For further details, see Sahakyan et al.

[7] https://irsa.ipac.caltech.edu/applications/DUST/index.html

[30].

The optical and ultraviolet light curves are shown in Figure 4.1 (panels e and f). Variability is detected in all *SWIFT*-UVOT filters, with the source alternating between flaring and quiescent states. The highest flux of 3.13×10^{-10} erg cm^{-2} s^{-1}, was observed in M2 band on MJD 53960.85, exceeding the time-averaged flux in the same filter, 1.18×10^{-10} erg cm^{-2} s^{-1}, by a factor of 2.7. Among the remaining filters, the highest flux is 2.78×10^{-10} erg cm^{-2} s^{-1} in W2 filter on the same epoch, which is 2.6 times higher than the time-averaged flux in this band 1.05×10^{-10} erg cm^{-2} s^{-1}. Across the UVOT bands, the ratio of the highest and lowest fluxes ($F_{\rm max}/F_{\rm min}$) are $V = 8.15$, $B = 7.90$, $U = 7.04$, $W1 = 8.29$, $M2 = 8.27$, and $W2 = 7.99$, indicating comparable but band-dependent variability.

In the optical band, we include additional data from the All-Sky Automated Survey for Supernovae [ASAS-SN; 113] in the V and g filters which was extracted from MMDC [for the details see 30]. The corresponding light curve is shown in Figure 4.1 panel h. The ASAS-SN light curve exhibits variability consistent with *SWIFT*-UVOT observations. The mean flux over the monitoring period is 5.8×10^{-11} erg cm^{-2} s^{-1}. The brightest epoch occurred at MJD 57604.14, when the flux reached 1.31×10^{-10} erg cm^{-2} s^{-1}; the faintest state was at MJD 59771.34 with the flux of 2.37×10^{-11} erg cm^{-2} s^{-1}, corresponding to ratio of ~ 5.5 between the highest and lowest fluxes. These long-term optical measurements show pronounced variability of PKS 2155-304 emission in the optical band.

4.2.4 ARCHIVAL AND VHE γ-RAY DATA

In addition to the data described above, we retrieved multi-band observations of PKS 2155-304 from MMDC. Some of these datasets are from catalogs that lack reliable time measurements; therefore these data are used only to construct the time-averaged SED of PKS 2155-304. In contrast, time-resolved datasets—such as data from the Near-Earth Object Wide-field Infrared Survey Explorer [NEOWISE; 114] and the Small and Moderate Aperture Research Telescope System [SMARTS; 115] - are used to investigate the temporal evolution of PKS

2155-304 emission in the IR and optical bands. The details of the NEOWISE and SMARTS data extraction, as well as the conversion from magnitudes to fluxes, are presented in Sahakyan et al. [30]. The SMARTS lightcurves in the J, R, V, and B filters are shown in Figure 4.1, panel i, demonstrating clear variability in all bands. SMARTS monitoring shows a major optical flare around MJD 55500: the activity started after MJD 55400 and lasted several weeks. This flare was detected quasi-simultaneously in all available bands (J, R, V and B). The brightest epoch occurred on MJD 55538.05, when the B-band flux reached 2.34×10^{-10} erg cm^{-2} s^{-1}, a factor of ~ 2.9 above the long-term average flux from the SMARTS monitoring of PKS 2155-304 ($\langle F\rangle \simeq 8.2\times10^{-11}$ erg cm^{-2} s^{-1}). Additional flares are present throughout the campaign, but this flare is the most prominent one. In the infrared band, NEOWISE observed PKS 2155-304 in different periods at 3.4 and $4.6\,\mu$m. NEOWISE observations are organized in short campaigns spanning one to a few days approximately every six months. Therefore, in order to increase signal-to-noise ratio the observations with separation less than 10 days are grouped and combined using a weighted mean. The resulting light curve with the fluxes grouped around each observations is shown in Figure 4.1, panel j revealing moderate variability of the source in the IR band. The maximum weighted-mean flux at 8.817×10^{13} Hz ($3.4\,\mu$m) is $(4.57\pm0.02)\times10^{-11}$ erg cm^{-2} s^{-1} at MJD 56791.00, while at 6.517×10^{13} Hz ($4.6\,\mu$m) the peak is $(3.81\pm0.01)\times10^{-11}$ erg cm^{-2} s^{-1} at MJD 56791.03.

PKS 2155-304 is a well-known emitter in the VHE γ-ray band. To complete the broadband SED, we include published VHE observations of PKS 2155-304 by HESS from Aharonian et al. [107] and Abdalla et al. [116] and incorporate them into our dataset. When contemporaneous multi-band coverage exists, these points are included in the time-resolved SEDs. The VHE data provide crucial information at the highest energies, helping to constrain the second component in the SED of PKS 2155-304.

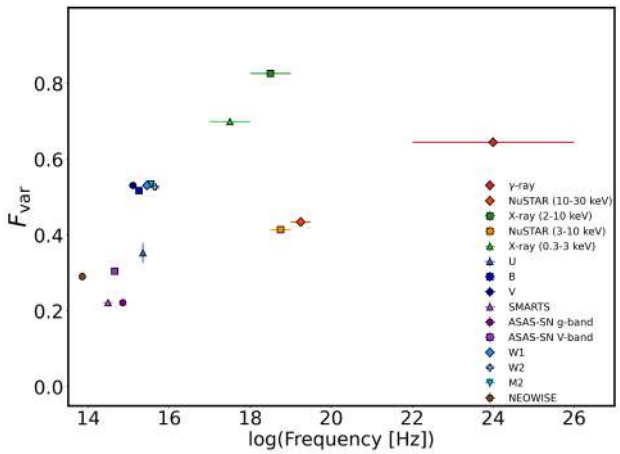

Figure 4.2: Fractional variability amplitude $F_{\rm var}$ as a function of frequency for PKS 2155-304. Symbols/colours denote bands as in the legend. Vertical error bars are 1σ uncertainties on $F_{\rm var}$; horizontal bars indicate the width of each band.

4.2.5 FRACTIONAL VARIABILITY

In order to quantify the variability in different bands, we use the fractional variability $F_{\rm var}$ estimated following Schleicher et al. [117]. Figure 4.2 shows $F_{\rm var}$ as a function of frequency; horizontal bars indicate the frequency/bandwidth of each instrument/filter, and vertical bars show $F_{\rm var}$ and its uncertainty. The variability amplitude is strongly energy-dependent. In the infrared-optical bands (NEOWISE, SMARTS, ASAS-SN) the variability is low to moderate, $F_{\rm var} \sim 0.2$–0.3. In the optical/UV bands (*SWIFT*-UVOT) the variability amplitude is higher, $F_{\rm var} \sim 0.35$–0.55, showing more active states in the light curve. The variability is highest in soft/medium X-rays: $F_{\rm var} \sim 0.7$ in 0.3–3 keV and ~ 0.8 in 2–10 keV bands. At harder X-rays (*NuSTAR*, 3–10 and 10–30 keV) the amplitude decreases to $F_{\rm var} \sim 0.42$–0.44. In the HE γ-ray band the variability is moderate with $F_{\rm var} \approx 0.65$ (Figure 4.2).

This trend of fractional variability is overall expected for a blazar of type HSP. In the spectrum of this type of blazars, the emission in the infrared-optical bands are dominated by low-energy electrons with longer synchrotron cooling times, so the variability amplitude is shorter. Variability grows toward the soft/medium X-rays, which corresponds to the highest-energy tail of the synchrotron component; here acceleration and cooling timescales are shortest, so small changes in the injected electron population, magnetic field B, or

Doppler factor δ produce large flux changes. The moderate GeV-band variability is consistent with SSC-dominated inverse-Compton emission in HSPs: the IC component reflects the changes in the same electron population that powers the variability in the X-ray band, but the longer binning partially smooth out the rapid fluctuations.

4.3 TIME EVOLUTION OF THE MULTIWAVELENGTH SED

The datasets assembled above provide a comprehensive, multi-epoch view of the emission from PKS 2155-304 across the electromagnetic spectrum. This allows to build both a time-averaged SED and a series of time-resolved SEDs that track spectral evolution in different periods. For blazars, this distinction in time-resolved SEDs is essential: variability can shift the normalization and peak frequencies of both the synchrotron and inverse-Compton components. This combination of broad spectral coverage and temporal resolution in different periods is therefore critical to understand the origin of the emission and its changes in time.

In order to build the time resolved SED of PKS 2155-304, we adopt the SED/LC animation methodology used previously to study the source BL Lac [106], 3C 454.3 [104], CTA 102 [105], and OJ 287 [29]. To build the SED/LC animation, we merge the multi-band light curves in Figure 4.1 with additional observational data from MMDC, then group the data that are simultaneous or quasi-simultaneous considering the γ-ray intervals as a base to build the time-resolved SEDs. Namely, the γ-ray light curve is segmented into smaller intervals with the Bayesian Blocks algorithm to define intervals of approximately constant flux (orange line in Figure 4.1, panel a). For each block, a dedicated spectral analysis of *Fermi*-LAT data is then performed with the method previously described in Section 4.2 to produce energy-resolved flux points (5 or 7 flux points, depending on the detection significance of the source in the considered interval). Data from all other bands that are within the Bayesian block window are then binned within the same block applying an adaptive time scan that subdivides the block into shorter windows to maximize simultaneity of the

data while retaining sufficient data points. The resulting SEDs are plotted and changed sequentially—each aligned with its corresponding light-curve segment—to produce an SED/LC animation that tracks changes in the emission components. More implementation details on building SED/LC animation are provided in Sahakyan et al. [30].

The resulting SED/LC animation for PKS 2155-304 is available on YouTube[8]. It demonstrates the temporal evolution of the synchrotron and inverse-Compton components and enables to identify spectral component changes, peak-frequency shifts, flaring periods, etc. The broadband SED of PKS 2155-304 shows the traditional two-component structure, with the synchrotron peak at $\nu_{\rm s} \simeq (1\text{-}5) \times 10^{16}$ Hz (UV-soft X-ray). Although the X-ray flux varies substantially, the synchrotron peak frequency remains stable within uncertainties; variability is dominated by changes in flux with only mild curvature variations and no systematic shift in $\nu_{\rm p}$. The variability is energy-band dependent and is consistent with the fractional-variability pattern: variability is small to moderate in the optical/UV, largest in the soft X-ray band, and moderate in the HE γ-ray band.

4.4 MODELING OF PKS 2155-304 SEDS

4.4.1 THE SSC MODEL

To model the broadband SEDs of PKS 2155-304, we adopt a one-zone leptonic synchrotron/SSC model [12–14]. In this model, a spherical emission region of radius R moves relativistically along the jet with bulk Lorentz factor Γ and is viewed at a small angle $\theta \sim 1/\Gamma$ with respect to the jet axis. The region contains a homogeneous magnetic field of strength B and a non-thermal population of relativistic electrons. The low-energy component of the SED, extending from radio to X-ray frequencies, is explained by synchrotron radiation from these electrons as they spiral in the jet magnetic field. The same population upscatters the synchrotron photons to HEs via the inverse Compton process, producing the HE component. In the current study, the model is computed using a novel

[8] https://youtu.be/nHYfChQSOPU

Table 4.5: Model parameters from one-zone SSC fits to the SEDs of PKS 2155-304 in the different states shown in Figure 4.3. These are provided as examples, but each of the 253 SEDs have been fitted and their parameters recovered.

State	B [10^{-2} G]	L_e [10^{44} erg s^{-1}]	$\gamma_{\rm max}$ [10^5]	R [10^{17} cm]	δ	p	L_B [10^{43} erg s^{-1}]
QS	1.62 ± 0.02	9.14 ± 5.20	2.09 ± 0.88	3.31 ± 1.20	24.6 ± 6.1	2.30 ± 0.21	6.55 ± 2.51
MWF	4.78 ± 0.19	5.36 ± 1.35	4.87 ± 2.78	1.88 ± 0.83	24.8 ± 5.2	2.20 ± 0.13	18.5 ± 6.13
γF	1.71 ± 1.70	13.7 ± 4.73	1.83 ± 0.43	4.64 ± 0.96	18.2 ± 4.9	2.06 ± 0.09	7.78 ± 1.76
XF	1.64 ± 0.21	6.48 ± 2.46	9.81 ± 5.82	5.34 ± 0.84	18.8 ± 5.4	2.21 ± 0.14	10.1 ± 2.22
OUF	1.28 ± 0.14	11.1 ± 4.23	2.33 ± 0.63	5.63 ± 1.15	20.8 ± 5.4	2.17 ± 0.14	8.42 ± 2.21
Unclassified	1.56 ± 1.35	9.42 ± 5.50	1.51 ± 0.41	4.53 ± 1.58	23.0 ± 5.4	2.25 ± 0.14	9.98 ± 2.49

neural-network-based method presented in Bégué et al. [3]. In this approach, the computationally expensive radiative calculations, including electrons cooling, are replaced by a CNN surrogate model, trained on a large set of synthetic SEDs generated with `SOPRANO` [118] over a wide range of model parameters. `SOPRANO` self-consistently solves the coupled kinetic equations for electrons and photons—including particle injection and radiative cooling—and computes the corresponding SEDs. Once trained, the CNN accurately reproduces the radiative output of particles inside the jet while reducing the evaluation time by orders of magnitude, enabling fitting and parameter inference.

In this work, the injection spectrum of the electron energy distribution and its normalization follow Equations 1.4 and 1.5. In addition, both electrons and photons are assumed to leave the emitting region in the characteristic dynamical time $t = R/\Gamma$. To conclude, the model has seven free parameters: p, $\gamma_{\rm min}$, $\gamma_{\rm max}$, B, R, δ, and the electron luminosity $L_{\rm e}$, although in practice we do not fit for $\gamma_{\rm min}$, see below.

4.4.2 FIT METHOD AND CLASSIFICATION

In the SED/light-curve animation discussed in Section 4.3, a total of 327 SEDs are available. However, not all of these can be reliably modeled due to insufficient observational coverage. Among them, only 253 SEDs have adequate multiwavelength coverage enough for the modeling: specifically, we require the availability of X-ray data together with measurements in the low-energy band, as the γ-ray data is available by default. These SEDs were therefore selected for modeling. The fits were performed using MultiNest, a nested

sampling algorithm [86]. We adopted 1500 active points and a tolerance of 0.4, which ensures both efficient exploration of the parameter space and robust convergence of the posterior distributions. For the modeling, we fixed the minimum Lorentz factor of the electron distribution to $\gamma_{\rm min} = 100$. This choice is motivated by two considerations. First, the low-energy emission (below $\sim 10^{10}$ Hz) is often produced in more extended regions of the jet, which are not well constrained by the compact one-zone model applied here. Second, observational data at low frequencies are not available in most of the SEDs selected here. Setting $\gamma_{\rm min} = 100$ avoids introducing unconstrained degrees of freedom while remaining consistent with the value of $\gamma_{\rm min}$ usually adopted in blazar modeling [see e.g. 119]. Finally, we note that EBL absorption at high energy is included by multiplying the emission model described in Section 4.4.1 by the model developed in Domínguez et al. [88].

In order to have a quantitative discussion on the emission states of PKS 2155-304, the selected SEDs were grouped in different categories based on the activity states. Namely, the dataset was divided into three frequency ranges: optical/UV ($3 \times 10^{14} - 10^{16}$ Hz), X-rays ($10^{16} - 10^{21}$ Hz), and γ-rays ($10^{21} - 10^{28}$ Hz). For each range, we computed the average flux and its standard deviation which serve as a baseline level. Then, the state of the source was classified in the following way. A multiwavelength flare (MWF) was identified when the flux in all three bands exceeded the archival average, whereas a quiescent state (QS) was defined when the flux in all bands is on average or remained below the average. If only the γ-ray flux was above the average while the UV/optical and X-ray bands were below, the episode was classified as a γ-ray flare (γF). Similarly, an X-ray flare (XF) corresponded to a case where the X-ray flux was above the average while the other bands remained lower, and a UV/optical flare (OUF) was defined when only the optical/UV flux exceeded the average. A total of 117 SEDs were classified as QS, 18 as MWF, 7 as γF, 20 as XF, and 31 as OUF. The remaining 61 SEDs display mixed characteristics in the mentioned bands and are left unclassified. This separation makes it possible to separate true

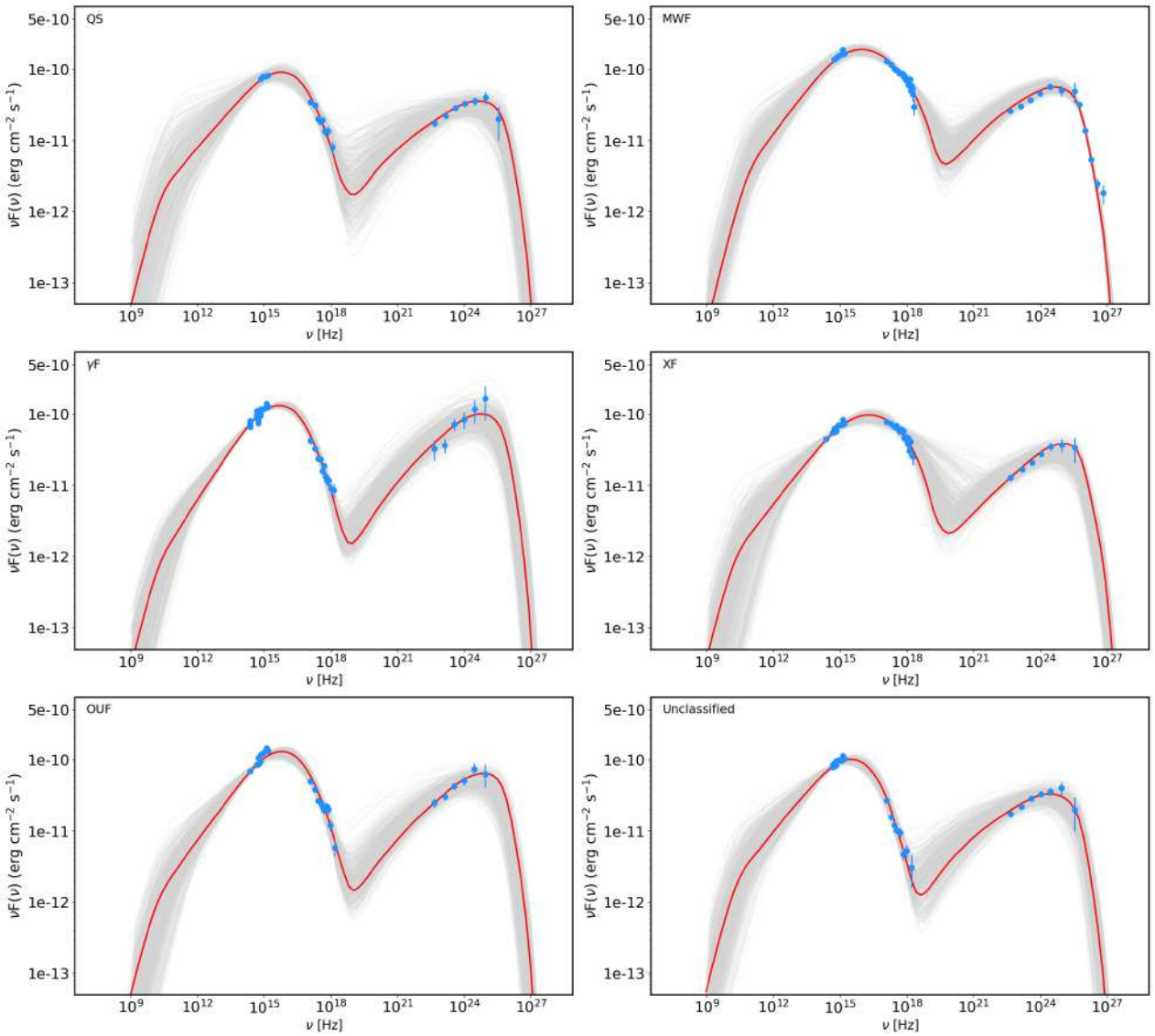

Figure 4.3: For each SED class, example of a multiwavelength SEDs of PKS 2155-304 modeled within the one-zone SSC framework. The blue points are the data, the red curve corresponds to the best-fit model (e.g., when the likelihood is maximum) and the gray spectra corresponds to the model uncertainty. Extragalactic background light absorption is included in the modeling using the model of Domínguez et al. [88].

multiwavelength flares from band-limited flares and quiescent states, thereby providing a clearer characterization of the variability pattern of PKS 2155-304 across the electromagnetic spectrum.

4.4.3 EXAMPLE OF FIT RESULTS FOR EACH CATEGORY

Before studying in detail the statistical properties of each SED category, we provide for each one independently an example demonstrating the fitting performances and results.

An example of the SED corresponding to the QS is shown in the upper-left

panel of Figure 4.3 and the corresponding parameters are given in Table 4.5. The red solid line represents the model obtained with the best-fit parameters, while the gray lines indicate the associated uncertainties. In this state, the emission can be explained with (i) an electron power-law index $p = 2.3$, (2) a maximum Lorentz factor of the electron distribution $\gamma_{\rm max} = 2.1 \times 10^5$, (3) a magnetic field strength $B = 1.6 \times 10^{-2}$ G, (4) an emitting region radius $R = 3.3 \times 10^{17}$ cm, and (5) a Doppler factor $\delta = 24.6$. The total kinetic power carried by electrons is $L_{\rm e} = 9.1 \times 10^{44}$ erg s^{-1}, while the power in the magnetic field, computed as $L_B = \pi c R^2 \Gamma^2 U_B$, is 6.5×10^{43} erg s^{-1}.

The SED corresponding to the MWF is presented in the upper-right panel of Figure 4.3 with corresponding parameters in Table 4.5. In this case, the emission is produced from a region with a magnetic field of $B = 4.8 \times 10^{-2}$ G and an electron kinetic power of $L_{\rm e} = 5.4 \times 10^{44}$ erg s^{-1}. The maximum Lorentz factor of the electron distribution is $\gamma_{\rm max} = 4.9 \times 10^5$, indicating the presence of highly energetic particles in the emitting region. As we demonstrate below, these high energy electrons are characteristics of the MWF activity. The size of the emitting region is $R = 1.9 \times 10^{17}$ cm, and the Doppler factor is $\delta = 24.8$ demonstrating a significant relativistic boosting during this MWF. The electron energy distribution is characterized by a power-law index $p = 2.20$.

The SEDs corresponding to γF, XF, and OUF states are shown in the middle and lower-left panels of Figure 4.3. In all cases, the broadband emission is well modeled with the SSC model used in this study, with the best-fit parameters for these examples summarized in Table 4.5. In the γF state, the fit yields a magnetic field of $B = 1.71 \times 10^{-2}$ G, an electron luminosity of $L_{\rm e} = 1.37 \times 10^{45}$ erg s^{-1}, and a maximum Lorentz factor of $\gamma_{\rm max} = 1.8 \times 10^5$. The emitting region size is $R \simeq 4.6 \times 10^{17}$ cm, and the Doppler factor is moderately low compared to other states ($\delta \simeq 18.2$). The electron slope is harder than in the QS ($p = 2.06$), consistent with harder particle injection during the γ-ray activity. In the XF state, the electron energy distribution reaches significantly higher cutoff energies, with $\gamma_{\rm max} \simeq 9.8 \times 10^5$, almost an order of magnitude larger than in the γF and OUF states. This shift is

accompanied by a relatively weak magnetic field ($B = 1.64 \times 10^{-2}$ G) and large emission region ($R \simeq 5.3 \times 10^{17}$ cm). The Doppler factor remains moderate ($\delta \simeq 18.8$), while the electron luminosity is comparatively lower ($L_{\rm e} \simeq 6.5 \times 10^{44}$ erg s^{-1}). These values indicate that the electrons are effectively accelerated to higher energies which drives the strong changes in the X-ray component. On the contrary, the OUF state is characterized by a higher magnetic field ($B = 2.04 \times 10^{-2}$ G) and a more compact emission region ($R \simeq 3.5 \times 10^{17}$ cm). The maximum Lorentz factor is the lowest among the flaring states ($\gamma_{\rm max} \simeq 1.4 \times 10^{5}$), suggesting that the flare is dominated by the emission from low energy electrons rather than re-acceleration or injection of fresh energetic electrons. The Doppler factor remains high ($\delta \simeq 23.9$), also in this case.

An example of modeling of the SED which was unclassified is shown in the lower-right panel of Figure 4.3, and the corresponding parameters are listed in Table 4.5. In this epoch, the optical/UV and γ-ray fluxes are consistent with their long-term averages, whereas the X-ray flux is comparatively low. In this case a one-zone SSC model reproduces the broadband SED well with parameters that are not substantially different than those obtained in the other cases.

As seen from these examples, while the SSC model provides a satisfactory description of the data in all cases, the key differences in the parameters during different states, namely: the high $\gamma_{\rm max}$ in the XF state, the flatter electron spectrum in the γF state, and the stronger magnetic field in the OUF state show that distinct physical processes dominate in each activity state. These examples suggest that the spectral variability in PKS 2155-304 is not driven by a single mechanism, but rather by changes in the emitting particle or in the emission region. It is the purpose of Section 4.5 to demonstrate the statistical differences across the different emission episodes and isolate parameter changes responsible for changes in the spectrum of PKS 2155-304, to enable a physical description of the different emission periods of PKS 2155-304.

4.4.4 THE PREVIOUS MODELINGS OF PKS 2155-304

In contrast to earlier studies, where the modeling of PKS 2155-304 was performed for only a limited number of broadband SEDs, the analysis presented here considers modeling of a substantially larger number of SEDs. The results obtained in this study across different states are typical of those usually found for blazars and consistent with previous studies of PKS 2155-304. For example, Madejski et al. [120] modeled the source during a low-flux state using contemporaneous multiwavelength data. Their results indicated that the emission can be explained with an electron energy distribution with an index $p = 2.2$, a break Lorentz factor $\gamma_{\rm br} = 2.6 \times 10^4$, and a magnetic field strength of $B = 0.5$ G, with a characteristic emitting region radius of $R = 1.3 \times 10^{16}$ cm. Most of these parameters (except B) are within the range that we estimated for the QS, see Section 4.5. Another modeling of PKS 2155-304 was presented in Aleksić et al. [121] based on the 2006 MAGIC campaign; the SED was modeled by adopting (and not fitting) the parameters $\delta = 50$, $B \simeq 0.085$ G, and $R \simeq 9 \times 10^{15}$ cm. However, in their SED the contemporaneous HE γ-ray data were absent limiting the constraints provided by the inverse Compton component. The main difference between the results obtained here and these previous studies of PKS 2155-304 is that we performed modeling without assuming any specific initial spectral shape, instead exploring the global minima of the posterior distributions for each SED across many time periods.

4.5 STATISTICAL ANALYSIS OF THE DIFFERENT STATES

Multiwavelength modeling plays a central role in advancing our understanding of blazar emission, especially when different states can be compared. This approach allows to compare and contrast key model parameters, which in turn provides a direct link between the observed variability patterns and the underlying physical conditions in the jet. In this way, observational properties, e.g., the flux changes or spectral variability in different bands, can be connected with physical parameters characteristics of

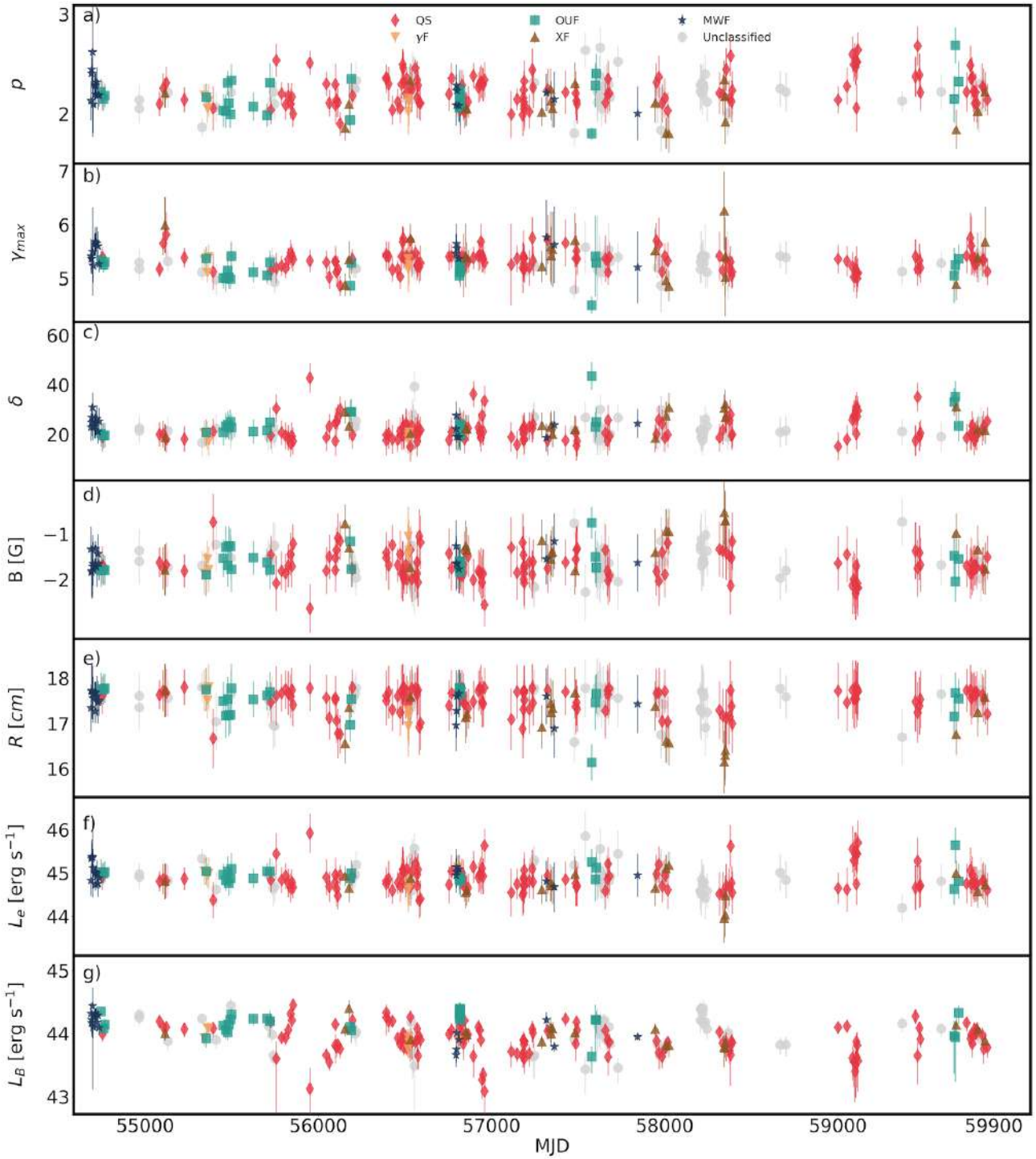

Figure 4.4: Time evolution of the one-zone SSC parameters for PKS 2155-304, derived from fitting the SEDs in different states — QS (red diamonds), γF (orange downward triangles), OUF (green squares), XF (brown upward triangles), MWF (navy stars), and unclassified (gray circles). Panels show (a) the electron power-law index p, (b) the maximum electron Lorentz factor $\gamma_{\rm max}$, (c) the Doppler factor δ, (d) the magnetic field B [G], (e) the emitting-region radius R [cm], (f) the electron kinetic power L_e [erg s^{-1}] , and (g) the (derived) magnetic power L_B [erg s^{-1}] versus MJD. Colored symbols denote activity states as indicated in the legend.

the emission region, such as the spectral slopes of the emitting particles, the magnetic field, the maximum energy of the electrons, etc. These can then be transformed into constraints on particle acceleration, energy dissipation, and radiation processes.

The modeling of the selected 253 time-resolved SEDs together with the time evolution of the posterior distributions of the model parameters is presented as a YouTube animation[9] synchronized with the corresponding light-curve intervals, connecting the evolution of both the multi-wavelength emission state and the SED modeling. The images from the animations are available on GitHub[10]. The convergence of the fitted parameters was evaluated using the posterior distributions obtained from the MultiNest sampling. For each parameter, the 68% highest posterior density interval was derived, and its position and extent were compared with the adopted prior boundaries. Parameters were considered converged when their posteriors were well contained within the prior range, while those showing a significant fraction of posterior samples near a prior boundary were flagged as potentially unconstrained. According to these criteria, only the spectral index and the emitting-region radius exhibited edge effects: in 13 SEDs, the spectral index showed boundary proximity, whereas for R this occurred in 161 cases. This behavior is expected, as R is difficult to constrain from the SED alone [see 122] and is typically estimated through variability or geometrical arguments, which were not imposed in the present analysis. Overall, these diagnostics confirm stable and well-converged sampling for all parameters except the radius, whose broad posterior distributions reflect intrinsic parameter degeneracies rather than numerical non-convergence. The temporal evolution of the parameters is shown in Figure 4.4, where different emission states are represented by distinct colors and symbols. Such a representation allows to evaluate changes in parameter space that are responsible for flaring activities when comparing with the light curve from Figure 4.1, either across the full multiwavelength band or within specific energy

[9] https://youtu.be/jqssDn5Gjs8

[10] https://github.com/gevorgharutyunyan/PKS-2155-304/tree/main/time_resolved_sed_modeling

Table 4.6: Results of the KS test, indicating if the parameter variation between any state and the QS are significant. The parameters are in this order: magnetic field (B), electron luminosity (L_e), maximum energy ($\gamma_{\rm max}$), emission region size (R), Doppler factor (δ), spectral index (p).

State	B		$L_{\rm e}$		$\gamma_{\rm max}$		R		δ		p	
	KS	$\mathfrak{p}$	KS	$\mathfrak{p}$	KS	$\mathfrak{p}$	KS	$\mathfrak{p}$	KS	$\mathfrak{p}$	KS	$\mathfrak{p}$
MWF	0.338	0.045	0.359	0.027	0.474	1.0×10^{-3}	0.252	0.236	0.410	0.007	0.137	0.899
γF	0.267	0.354	0.293	0.254	0.327	0.155	0.265	0.364	0.239	0.489	0.506	0.004
XF	0.545	3.0×10^{-5}	0.301	0.072	0.338	0.030	0.519	8.8×10^{-5}	0.390	0.008	0.405	0.005
OUF	0.316	0.007	0.381	4.8×10^{-4}	0.418	8.9×10^{-5}	0.143	0.581	0.290	0.016	0.283	0.021

ranges, thereby offering clues about the physical origin of these events.

4.5.1 STATISTICAL PROPERTIES OF THE INFERRED MODEL PARAMETERS

From modeling the 117 SEDs in the QS state we found that, the best-fit model parameters exhibit relatively narrow distributions. The electron power-law index is centered around a mean of $p \simeq 2.24$ (median 2.22), varying between 1.90 and 2.68. The electrons maximum Lorentz factor spans nearly an order of magnitude, from $\gamma_{\rm max} \simeq 7.2\times10^4$ to 6.5×10^5, with an average value of 2.3×10^5. The magnetic field strength is typically weak, ranging from $B \simeq 2.3\times10^{-3}$ to 1.8×10^{-1} G, with a mean of 2.6×10^{-2} G. The size of the emitting region is large, with radii between $R \simeq 4.7\times10^{16}$ and 6.3×10^{17} cm (mean 3.8×10^{17} cm). The Doppler factor varies moderately, with values from $\delta \simeq 15.1$ to 42.7 (mean ~ 21.9). The electron kinetic power is of the order of $L_{\rm e} \sim 10^{45}$ erg s^{-1}, ranging from 2.4×10^{44} to 8.3×10^{45} erg s^{-1}, with a mean value of 1.0×10^{45} erg s^{-1}.

The modeling of the 18 SEDs identified as MWF shows that the magnetic field strength varies within $B \simeq 1.5\times10^{-2}$ - 7.0×10^{-2} G, with an average value of 2.9×10^{-2} G. The electron luminosity varies in the range between 4.8×10^{44} erg s^{-1} and 2.4×10^{45} erg s^{-1} with a mean of 1.1×10^{45} erg s^{-1}. The maximum Lorentz factor of the electron distribution is between 1.6×10^5 and 5.8×10^5, with a mean value of 3.4×10^5, which shows the presence of electrons accelerated to GeV energies during flares. The emission region is found to be relatively extended, $R = 0.8\times10^{17}$–5.4×10^{17}cm, with a mean radius of 3.4×10^{17} cm. The Doppler factors cluster around $\delta \sim 24$, ranging from 18.7 to 30.9, while the power-law index of electron energy distribution changes between $p = 2.0$ and 2.6 with a mean of 2.23.

In the γF state, the modeling shows that the emission regions are moderately extended, $R \sim 0.9$–6.3×10^{17}cm, with relatively weak magnetic fields, $B \sim 1.3 \times 10^{-2}$–$8.9 \times 10^{-2}$G. The maximum energy of the electron distribution $\gamma_{\rm max}$ is in the range between 1.0×10^5 and 2.5×10^5, while the electron luminosity are in the range of $L_{\rm e} \sim (0.4 - 1.4) \times 10^{45}$ erg.s^{-1} with a mean of $L_{\rm e} = 8.4 \times 10^{44}$ erg s^{-1}. In these periods, the power-law index of the electrons is stepper than in other ones, with $p = 2.02 - 2.18$, indicating that more energy is present in the highest energy electrons, while the Doppler boost is in the range $\delta \sim 17 - 21$.

In contrast, the modeling shows that XF have systematically higher electron maximum energies and magnetic field: $\gamma_{\rm max}$ varies in the range of 7.1×10^4 and 1.8×10^6 with 70% of the estimated $\gamma_{\rm max}$ being above 2×10^5. The magnetic field is stronger on average, varying between $B \sim 1.6 \times 10^{-2} - 0.3$ G, while the emission regions are somewhat more compact, $R \sim 1.4 \times 10^{16}$–$5.3 \times 10^{17}$cm. The modeling of these flares also results in a high Doppler factor, $\delta \sim 18.5 - 32.2$, consistent with enhanced beaming during strong X-ray activity, and the electron luminosity is in the range between 9.0×10^{43} erg s^{-1} to $L_{\rm e} = 1.5 \times 10^{45}$ erg s^{-1} with a mean of $L_{\rm e} = 6.06 \times 10^{44}$ erg s^{-1}.

The modeling of SEDs in the OUF states shows yet another behavior: the magnetic field is moderate, $B = 9.0 \times 10^{-3} - 0.18$ G, with a mean of 3.7×10^{-2} G, but the emission regions are systematically larger, $R = 1.4 \times 10^{16} - 6.2 \times 10^{17}$cm, with 89% of the cases having an emission region size exceeding 10^{17}cm. The maximum Lorentz factor of the electrons is comparatively low, $\gamma_{\rm max}$ is in the range between 3.1×10^4 and 2.6×10^5 which is similar to the values estimated in the γF state but well below those estimated for XF. The Doppler boost is relatively strong varying in the interval $\delta = 19.4 - 43.5$, and the electron luminosity is comparable to the values estimated in γF, with $L_{\rm e} = 0.4 - 4.4 \times 10^{45}$ erg s^{-1}.

To clearly display the differences between the different emission states, we show on Figure 4.5, the distributions of the parameters for different states separately. This comparison shows several general trends. (i) In most cases, the mean of the electron power-law index remains relatively stable around

$p \sim 2.1 - 2.2$, with only a modest hardening during XF and γF. In contrast, (ii) the mean of the magnetic field shows a strong dependence on the spectral state: it is weakest in the QS and OUF ($B \lesssim 0.03$ G), moderate during MWF and γF, and highest in XF ($B \gtrsim 0.08$ G), representing a variation of a factor of nearly 3 on average between the different states. The mean of the Doppler factor clusters around $\delta \sim 20 - 25$ in most cases. (iii) The mean of the electron maximum Lorentz factor allows to distinguish the states very clearly: it is the highest in the MWF and XF ($\gamma_{\rm max} \gtrsim 3 \times 10^5$), comparatively lower in OUF state ($\gamma_{\rm max} = 1.5 \times 10^5$), and moderate in γF ($\gamma_{\rm max} = 1.7 \times 10^5$). (iv) The distribution of R shows relatively extended emission regions across all states, clustering around a few $\times 10^{17}$ cm. While the median values do not differ drastically, XF exhibits the widest spread, with R reaching both the lowest and highest extremes among the states. In contrast, QS, MWF, OUF, and γF tend to show more confined distributions with median values around $3 - 4 \times 10^{17}$ cm. (V) The distribution of $L_{\rm e}$ is comparatively stable across all states, with mean values around $10^{44.5} - 10^{45}\,{\rm erg\,s^{-1}}$. The QS exhibits a slightly broader spread, extending toward higher luminosities, while the flaring states (MWF, XF, and γF) appear more clustered and show no systematic enhancement in $L_{\rm e}$.

In order to investigate differences in the parameter distributions between the QS and other activity states, we performed Kolmogorov-Smirnov (KS) tests on the parameters. The results are summarized in Table 4.6, for each parameter providing the KS statistics and corresponding $\mathfrak{p}$-values (probability). We consider $\mathfrak{p}$-values below 0.05 (roughly corresponding to 2σ) as indicating statistically significant differences from the Quiet State distribution. For the MFW state, significant differences appear in B ($\mathfrak{p} = 0.045$), $L_{\rm e}$ ($\mathfrak{p} = 0.027$), $\gamma_{\rm max}$ ($\mathfrak{p} = 0.001$), and δ ($\mathfrak{p} = 0.007$), suggesting that these parameters change during flares compared to QS. In contrast, R and p show no notable differences ($\mathfrak{p} > 0.2$), meaning that the emission region size and electron spectrum remain similar to the QS. In the γF state, most parameters do not differ significantly from the QS, with $\mathfrak{p}$-values above 0.15 for B, $L_{\rm e}$, $\gamma_{\rm max}$, R, and δ. However, the spectral index p

shows a clear hardening ($\mathfrak{p} = 0.004$), pointing to changes in the electron energy distribution during γ-ray flares. The largest number of parameter changes are observed during the XF state with significant p-values for B ($\mathfrak{p} < 0.001$), $\gamma_{\rm max}$ ($\mathfrak{p} = 0.030$), R ($\mathfrak{p} < 0.001$), δ ($\mathfrak{p} = 0.008$), and p ($\mathfrak{p} = 0.005$). Only L_e does not show significant changes ($\mathfrak{p} = 0.072$), indicating that X-ray flares involve broad changes in the magnetic fields, emission geometry, beaming, as well as in the particle distribution, but electron luminosity is comparable to quiescence. For the OUF state, we find significant differences in all parameters except R ($\mathfrak{p} = 0.581$). For the other parameters, the significance is given by B ($\mathfrak{p} = 0.007$), $L_{\rm e}$ ($\mathfrak{p} < 0.001$), $\gamma_{\rm max}$ ($\mathfrak{p} < 0.001$), δ ($\mathfrak{p} = 0.016$), and p ($\mathfrak{p} = 0.021$). This suggests that flares in the optical/UV bands are the results of changes in magnetic fields, electron properties, and beaming, while the emission region size does not deviate much from the QS.

Overall, these KS test results show state-dependent variations in the physical parameters. The XF and OUF states show the strongest departures from QS, particularly for $\gamma_{\rm max}$ and δ. This could be due to enhanced particle acceleration and relativistic effects during flaring activities. The limited changes in the γF state, except p, suggest that γ-ray flares might be due to different mechanisms, which affects the electron spectrum but not the other parameters.

4.5.2 PHYSICAL INTERPRETATION

The modeling across different periods reveals state-dependent changes in several parameters that inform the emission scenario. The electron power-law index varies during the γF, XF, and OUF states but remains within $p \simeq 1.8$–2.7, i.e., within the range expected from shock-acceleration theory. Indices near $\simeq 2.0$ are characteristic of diffusive shock acceleration [1, 123, 124], while softer or harder spectra can arise in relativistic shocks [125–128]. Alternatively, such indexes can also be produced in magnetic-reconnection events [129–133].

During the γF state the electron spectrum hardens, with $p \simeq 2.0$–2.3. This is consistent with temporarily more efficient acceleration (e.g., higher

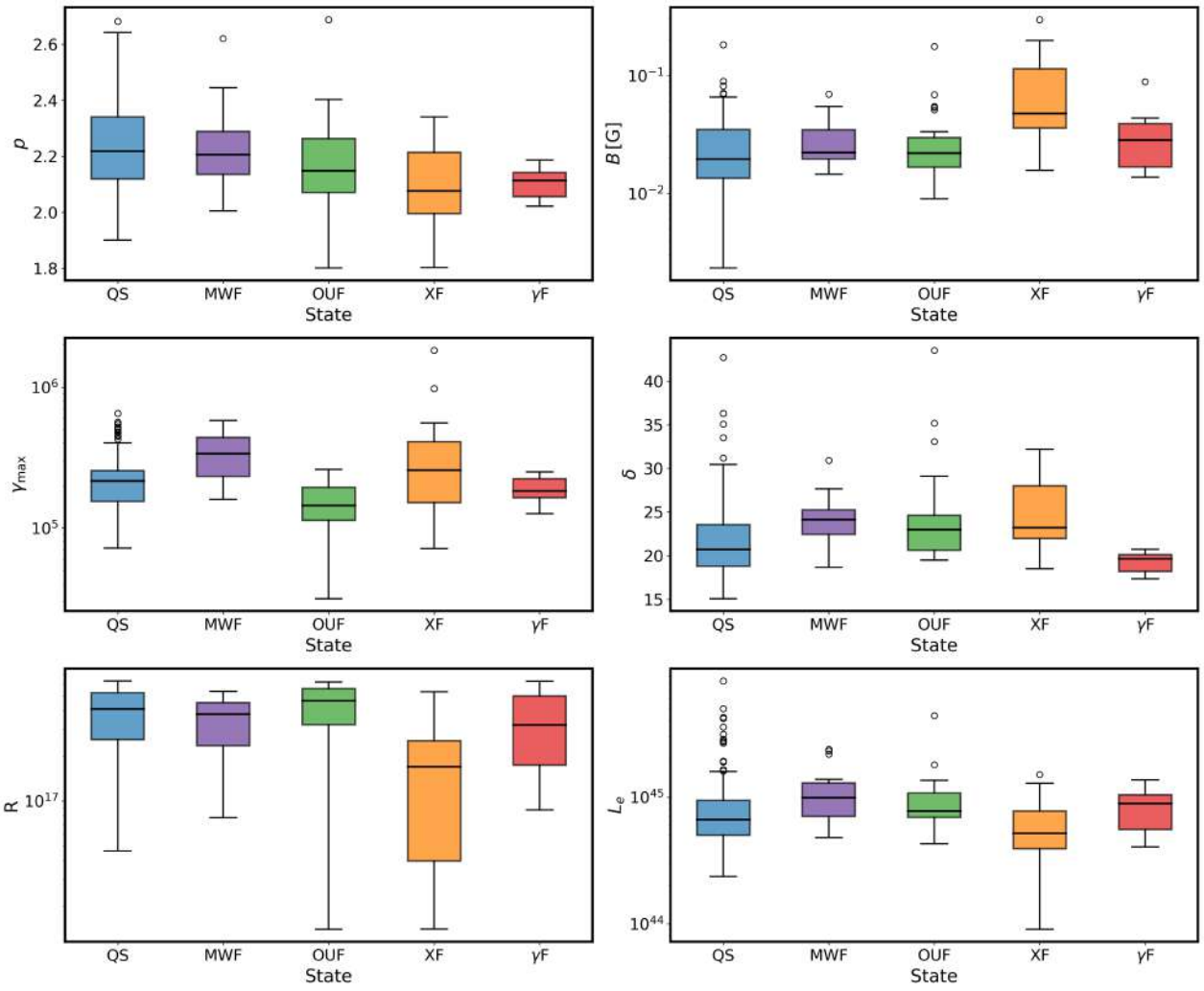

Figure 4.5: The distributions of all model parameters p, B [G], $\gamma_{\max}$, δ, R [cm] and L_e [erg.s^{-1}] for different states represented as box plots — QS (blue), MWF (violet), OUF (green), XF (orange) and γF (red). The central line marks the median, box edges correspond to the 25th and 75th percentiles, whiskers extend to $1.5\times$ the interquartile range , and outliers are plotted as circles. Qualitatively, the X-ray–flaring state tends to show larger B, while γ-ray-flaring states favor slightly harder p and lower δ and $\gamma_{\max}$ relative to other states.

shock compression, changes in turbulence anisotropy, or a larger effective mean-free-path ratio near the shock). The modeling does not show a significant increase in $\gamma_{\rm max}$ during γF, consistent with the relatively unchanged X-ray flux during these periods. As the other parameters do not change significantly, the γ-ray flares are more naturally attributed to changes in the injection/acceleration spectrum rather than to extended acceleration that raises the maximum energy or to changes in the emission-region size, parameters which remain statistically constant compared to the QS.

In the XF state, the inferred increase in B aligns with the observed X-ray variability pattern: the X-ray flux rises while the photon index remains soft (see Figure 4.1, panels c and d). Because the X-rays probe the high-energy tail of the synchrotron component, a higher B shifts the synchrotron peak upward and produces a higher peak flux without requiring a hardening of the electron slope.

During OUF, the fitted parameters are broadly consistent with those in other states, but the injected slope spans a wider range, $p \simeq 1.8$–2.7. This spread is expected because the optical/UV band samples the rising part of the synchrotron component, where the observed slope is sensitive to the locations of the synchrotron peak and the cooling break. Small changes in B or δ can move these features across the band, and modest curvature can be absorbed by the fit as changes in p. Moreover, if the γ-ray spectrum remains nearly unchanged while the optical/UV flux and shape vary, joint fits can accommodate a broader range of p.

In MWF states, the pattern indicates enhanced magnetic fields, increased power injected into electrons, and changes in bulk motion that affect beaming, while R and p show no systematic change within uncertainties. Thus, the geometry of the emitting region and the overall electron-slope shape appear roughly stable; flares are mainly driven by plasma variations that modify the magnetic field and the acceleration conditions.

The inferred parameters for the emission region size R in all the periods suggest that the radiation originates from an extended region in the jet. This

implies that the characteristic variability time, computed as $t_{\rm var} = (1+z)R/(\delta c)$, is of several days across all states: for the average state, with average $R \simeq 3.85\times10^{17}$ cm and average $\delta \simeq 21.9$, $t_{\rm var} \simeq 7.6$ days; in the XF state ($R \simeq 1.86\times10^{17}$ cm, $\delta \simeq 24.5$), $t_{\rm var} \simeq 3.3$ days; or in the UVOF state ($R \simeq 3.89 \times 10^{17}$ cm, $\delta \simeq 24.2$), $t_{\rm var} \simeq 7.0$ days, etc. This indicates that the flaring activity occurs over relatively large scales, without the rapid flux changes.

4.5.3 JET ENERGETICS

We examine the jet energetics, and in particular the luminosity carried by electrons and magnetic field in different activity states. We use the power ratio $\eta_B \equiv L_B/L_e$ to measure the magnetization of the jet. Because $L_{e,B} \propto \pi R^2\Gamma^2 c\, u'_{e,B}$, the common geometric/beaming factor cancels in the ratio, so η_B primarily shows the internal energy partition rather than beaming characteristics. Using the averaged mean values, the power ratio for each independent state is: $\eta_B \simeq 0.1$ (electron-dominated by a factor ~ 11) in QS, $\eta_B \simeq 0.13$ (~ 7.9) in MWF state, $\eta_B \simeq 0.12$ (~ 8.6) in γF state, $\eta_B \simeq 0.17$ (~ 5.9) in XF state and $\eta_B \simeq 0.16$ (~ 6.2) in OUF. Thus, the jet is particle-dominated in all states ($\eta_B \approx 0.09 - 0.17$). The jet is closest to the equipartition during XF: a higher B results in a larger $u'_B \propto B^2$ and hence L_B, while L_e does not change significantly. On the contrary in γF, η_B is lower than for XF which supports the scenario that γ-ray brightening is mainly driven by particle injection properties, producing a steeper index, rather than by an increased magnetization, or variation of other parameters.

It should be noted that the estimates of η_B strongly depend on the assumption of $\gamma_{\rm min} = 100$. Since L_e direction depends on the comoving electron energy density as $U_e \propto \int_{\gamma_{\rm min}}^{\gamma_{\rm max}} \gamma^{1-p} {\rm d}\gamma \approx \gamma_{\rm min}^{2-p}/(2-p)$, where the last approximation is obtained from assuming $p > 2$. Therefore, lowering $\gamma_{\rm min}$ increases U_e (and consequently L_e). In reality, the deviation from the equipartition condition could thus be stronger than reported here. Nevertheless, even under the assumption of $\gamma_{\rm min} = 100$, the obtained results allow for meaningful qualitative assessments of the underlying acceleration mechanisms. The condition $L_e \gg L_B$ (i.e., $\eta_B = L_B/L_e \ll 1$)

implies a low magnetization for an electron–positron-pair plasma. Moreover, if cold protons would carry part of the jet energy, the magnetization would become even smaller for a fixed U_B. In such a weakly magnetized environment, diffusive shock acceleration and stochastic (second-order Fermi) processes can operate more efficiently. Taken together, these considerations suggest that the energetics favor injection-driven variability in a particle-dominated, low-σ flow, where shocks or turbulence can reach the inferred $\gamma_{\rm max}$ without requiring high-σ reconnection or extreme acceleration efficiencies.

The assumption of $\gamma_{\rm min} = 100$ introduces uncertainties in the estimation of L_e, which in turn affect the inferred total jet power carried by electrons and the magnetic field. The contribution of the protons cannot be directly estimated from our analysis. Consequently, these facts limit a detailed discussion on the relation between the total jet power and the source properties. For instance, Nemmen et al. [134] showed that the kinetic power carried by accelerated particles correlates with the γ-ray luminosity in both blazars and γ-ray bursts, while Ghisellini et al. [135] found that the power of relativistic jets often exceeds the luminosity of their accretion disks. Keeping in mind the caveats in the determination of L_e and its large uncertainty, assuming one cold proton per electron would likely lead to an overestimation of the jet power. Having in mind that i) the content of cold protons in the jet is unknown, and *ii)*, that the disk of PKS 2155-304 is not directly observed, such a discussion in the context of PKS 2155-304 would remain incomplete.

4.6 SUMMARY

We presented a comprehensive time-resolved multiwavelength study of the HSP blazar PKS 2155-304, using extensive archival and processed data from the MMDC platform. Using observational data in the γ-ray, X-ray, optical, ultraviolet and IR bands, we have investigated the source variability in these bands and examined the origin of the emission through modeling the time-resolved SEDs in the different emission states.

The analysis showed energy-dependent variability, with the fractional

variability amplitude peaking in the soft to medium X-ray regime ($0.7 - 0.8$) - while remaining moderate in the optical/UV ($0.35 - 0.55$) and HE γ-ray bands ($\simeq 0.65$). This pattern aligns with expectations for HSP blazars, where synchrotron emission from HE electrons drives rapid variations in X-rays, contrasted by more stable contributions at lower energies.

Through Bayesian block segmentation of the γ-ray light curve, we generated 253 well-sampled time-resolved SEDs with quasi-simultaneous data, classifying them into distinct activity states: QS, MWF, γF, XF, and OUF. The modeling of these SEDs within a one-zone SSC scenario shows state-dependent parameter changes that are statistically significant compared to QS. KS tests show that MWF episodes differ in B, L_e, $\gamma_{\rm max}$, and δ, while R and p are consistent with QS. γ-ray flares are distinguished by a harder electron index p (with other parameters not significantly changed), indicating that the γ-ray brightening is due to changes in the particle injection/acceleration process leading to steeper electron spectra. XF states show the broader changes in the parameters: higher B and $\gamma_{\rm max}$, smaller R, and higher δ—consistent with enhanced acceleration and magnetization driving the strong X-ray flares. OUF states differ in B, L_e, $\gamma_{\rm max}$, δ, and p, but not in R, suggesting that optical/UV activity is produced by moderate changes in magnetization, boost, and the HE cutoff without geometric changes. During all the flaring periods, the jet energetics is dominated by the electrons luminosity rather than the magnetic luminosity, with power ratios $\eta_B \simeq 0.09 - 0.17$, which is approaching to equipartition during X-ray-dominant activity.

The results obtained here show the complex interplay of magnetic fields, particle acceleration, and relativistic beaming in producing flares in blazar emission, highlighting the value of long-term, multi-epoch modeling for these events for a better understanding of the origin of the flares.

5 THE ORIGIN OF MULTIWAVELENGTH EMISSION FROM PKS 1441+25

5.1 INTRODUCTION

Observations of blazars at VHE γ-raysare particularly important for understanding the physical conditions in their jets. In this energy range, most detected sources are BL Lac objects, whereas only a small number of FSRQs have been observed. This is generally because the dense external radiation fields present in FSRQs, especially those associated with the BLR, can strongly absorb VHE photons through $\gamma\gamma$ pair production. For this reason, the detection of VHE emission from an FSRQ is important for understanding how such photons are produced and escape from the source environment.

PKS 1441+25 is one of the few FSRQs detected in the VHE γ-ray band. During a strong flaring episode in April 2015, the source was detected by MAGIC and VERITAS [136, 137], with the emission extending to several hundred GeV. With a redshift of $z = 0.939$, it is also among the most distant blazars observed at VHE energies. This makes PKS 1441+25 an important case for studying the physical conditions under which VHE emission can arise in an FSRQ jet, while also taking into account the attenuation of the observed spectrum by the EBL [136, 137].

The 2015 activity of PKS 1441+25 was accompanied by extensive multiwavelength observations, providing a suitable dataset for a detailed study of the source over different activity periods. In this section, the origin of multiwavelength emisssion from PKS 1441+25 is investigated using the γ-ray data from *Fermi*-LAT, X-ray data from *NuSTAR*, X-ray and optical/UV data from *SWIFT*, together with additional optical measurements, to assemble the broadband SEDs of the source during selected epochs.

The main objective of this study is to examine the physical conditions in the jet of PKS 1441+25 during its 2015 activity, with particular focus on the period associated with the VHE detection. To do this, first the multiwavelength light curves is used to identify the relevant time intervals, and then model the corresponding SEDs with self-consistent radiative models. In this way, the

broadband emission changes across different states and what these changes imply for the origin of the VHE photons in this source are investigated.

5.2 DATA ANALYSIS

PKS 1441+25 was monitored across multiple wavelength bands using a combination of ground-based and space-based instruments. The datasets employed in this study are summarized below.

5.2.1 *FERMI*-LAT γ-RAY DATA

The γ-ray observations from the *Fermi*-LAT are used to examine the emission of PKS 1441+25 in the γ-ray band. The LAT is a pair-conversion instrument operating over an energy range of 20 MeV to 300 GeV and, in its nominal survey mode, scans the entire sky approximately every three hours. A detailed description of the *Fermi*-LAT instrument can be found in [36].

The γ-ray data used in this study were obtained from MMDC [30], which provides uniformly processed data from the observations of the blazars bright in γ-ray band. A complete description of the analysis methodology is given in [30]; here we summarize the essential steps. The analysis follows the standard point-source procedures implemented in the *fermitools* (version 2.0.8) using the P8R3_SOURCE_V3 instrument response functions. Events with high photon probability (*evclass*=128 and *evtype*=3) were selected within a 12° region of interest centered on the γ-ray position of PKS 1441+25 (RA $= 220.99^\circ$, Dec $= 25.02^\circ$), covering the interval from 2008 August 4 to 2023 July 4 (MET 239667417–710178221). To reduce contamination from Earth-limb emission, events with zenith angles greater than 90° were excluded. For the binned likelihood analysis, the model included all sources within a 17° radius of the target, as listed in the 4FGL catalog (incremental DR3; [10]). The spectral parameters of sources located inside the 12° region of interest were left free during the fit, whereas those outside this radius were fixed to their catalog values. The model also incorporated the standard Galactic and isotropic diffuse components, using the most recent templates, `gll_iem_v07` and

`iso_P8R3_SOURCE_V3_v1`. The significance of the γ-ray emission was evaluated using the test statistic $TS = 2(\ln L_1 - \ln L_0)$, where L_1 and L_0 denote the maximum likelihoods obtained with and without the source included in the model [138].

The γ-ray variability of PKS 1441+25 was investigated using the adaptive binning technique described by [96]. Unlike methods that divide the light curve into fixed time intervals, this approach defines time bins according to the statistical precision of the flux. Consequently, the bins become shorter during bright states-allowing to resolve the rapid variability-and longer during low-flux periods, ensuring sufficient photon statistics. This method enables the detection of flux changes and the identification of distinct emission states. To construct the adaptively binned light curve for PKS 1441+25, the full dataset was segmented into intervals for which the flux uncertainty above the optimal energy threshold $E_{\rm opt} = 300.2$ MeV reaches 20%. For each resulting bin, a standard unbinned likelihood analysis was performed using the same cuts described above. Within these shorter intervals, the spectrum of PKS 1441+25 was modeled with a simple power law, which provides an adequate representation of the γ-ray emission on such timescales.

The γ-ray light curve is shown in Figure 5.1, panel (a). The source exhibits enhanced γ-ray activity beginning around MJD 57000. The highest flux above 100 MeV was measured on MJD 57046.91, reaching $(9.11 \pm 1.93) \times 10^{-7}$ ph cm^{-2} s^{-1}. During this interval, the γ-ray photon index was 2.27 ± 0.24. While additional periods of elevated γ-ray activity are present, this episode represents the strongest γ-ray flare of PKS 1441+25 within the time range considered. The temporal evolution of the photon index is shown in Figure 5.1, panel (b). The mean γ-ray photon index over the entire dataset is $\Gamma_{\rm mean} = 2.15$, although the spectrum occasionally hardens significantly. The hardest index, 1.64 ± 0.21, was observed on MJD 57182.82. In total, 41 time bins exhibit a hard spectrum with $\Gamma < 1.9$. Notably, during the period when VHE γ-ray emission from PKS 1441+25 was detected (20-27 April) [136, 137], the HE-band photon index remained hard ($\Gamma < 2.0$) for most of the time.

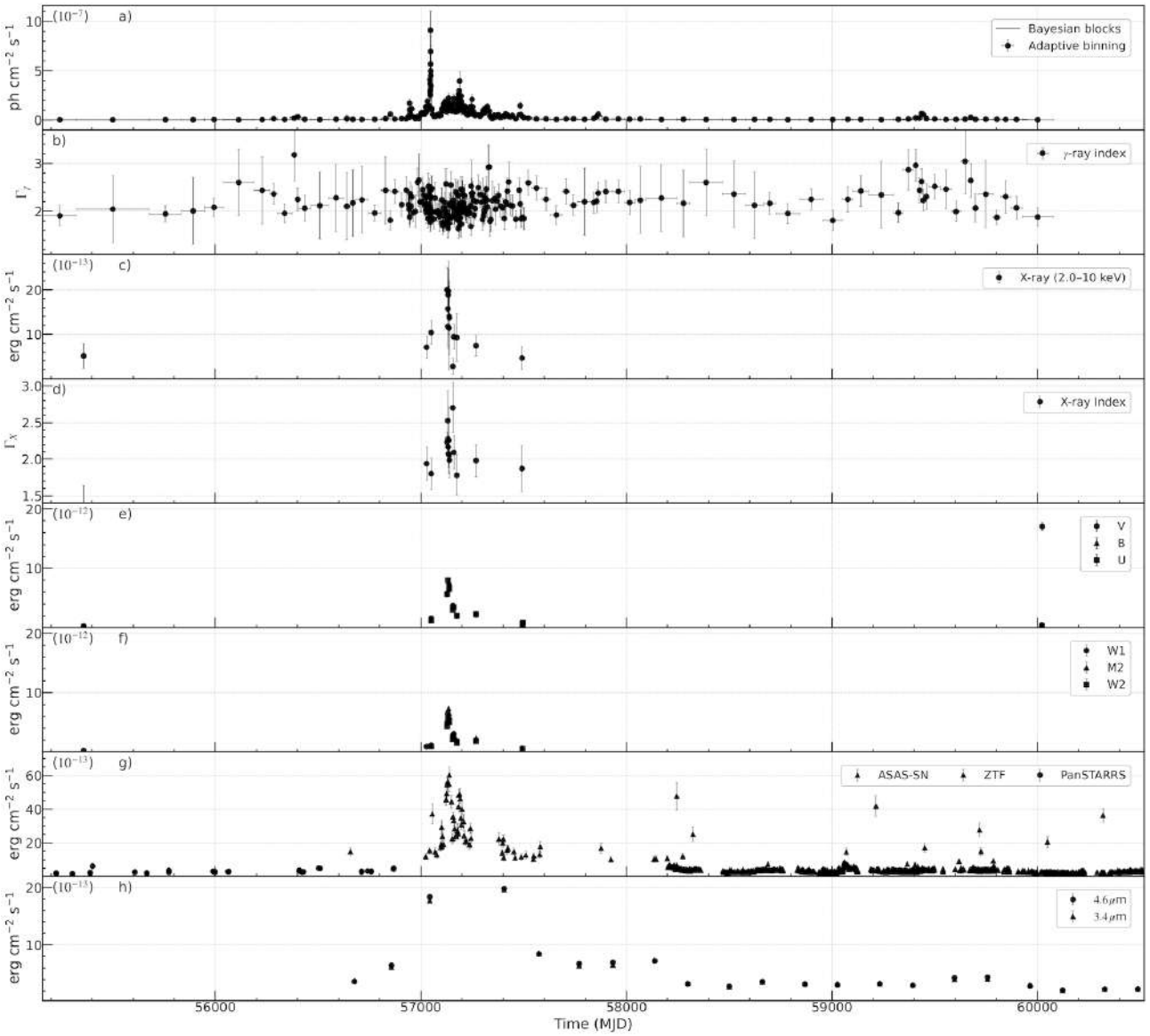

Figure 5.1: Multiwavelength light curves of PKS 1441+25 from 2008 to 2023. (a) Adaptively binned *Fermi*-LAT flux above 300.2 MeV, with the Bayesian-block representation of the light curve (solid line), (b) γ-ray photon index, (c) *SWIFT*-XRT 2-10 keV flux, (d) X-ray photon index in the 0.3-10 keV band, (e) *SWIFT*-UVOT optical fluxes in the V (circles), B (triangles), and U (squares) filters, (f) *SWIFT*-UVOT ultraviolet fluxes in the W1 (circles), M2 (triangles), and W2 (squares) filters, (g) Optical fluxes from ASAS-SN (triangles), ZTF (points), and Pan-STARRS (pentagons), (h) NEOWISE infrared fluxes at 4.6 μm (circles) and 3.4 μm (triangles). The pronounced high state around MJD 57000 is contemporaneous across the γ-ray, X-ray, optical/UV, and infrared bands.

5.2.2 X-RAY BAND

In the X-ray band, the emission from PKS 1441+25 was examined using ustar observations in the 0.3-10 keV range and *NuSTAR* data covering 3-79 keV.

In the *SWIFT* archive, 29 observations of PKS 1441+25 are available. These data-along with X-ray observations of all blazars by *SWIFT*-have been uniformly processed and are made publicly accessible through MMDC. A full description of the X-ray data analysis procedure is provided in [30]; here we summarize the steps relevant to the present work. The analysis was performed with the *Swift_xrtproc* tool [109], which builds on XRTDAS and uses XSPEC and XIMAGE to implement the standard reduction methods required for analyzing ustar data. For each observation, the tool automatically retrieves the archival dataset, applies event cleaning and filtering, and generates calibrated Level-2 products. Source counts are extracted from a circular region with a radius of 20 pixels (~ 47 arcsec), while the background is estimated from a nearby source-free region with a radius of 40 pixels. To check for possible pile-up, the count rate of each observation was inspected, and datasets exceeding $0.5\,\mathrm{count\,s^{-1}}$ were corrected following [109]. The spectra were grouped with GRPPHA to ensure at least one count per bin and then imported into XSPEC [110] for fitting using Cash statistics [112]. Both power-law and log-parabola models were tested, adopting a fixed Galactic hydrogen column density of $3.11 \times 10^{20}\,\mathrm{cm^{-2}}$. From the final spectral fits, we obtained the photon index and flux measurements in different X-ray bands for each observation.

The time evolution of the 2–10 keV X-ray flux is shown in Figure 5.1, panel (c). Most X-ray observations were carried out between MJD 57000 and 58000, coinciding with the period when the source exhibited enhanced γ-ray-band activity. The highest X-ray flux, $(2.00 \pm 0.50) \times 10^{-12}\,\mathrm{erg\,cm^{-2}\,s^{-1}}$, was observed on MJD 57127.5, exceeding by a factor of 7.3 the lowest flux of $(2.73 \pm 1.81) \times 10^{-13}\,\mathrm{erg\,cm^{-2}\,s^{-1}}$ observed on MJD 57155.3. The temporal evolution of the photon index in the 0.3–10 keV range is presented in Figure 5.1, panel (d). The mean photon index is 2.05, with values spanning from a minimum of 1.78 ± 0.28 to

a maximum of 2.74 ± 0.34. The observed variability in the photon index-ranging from relatively hard $\Gamma \approx 1.8$ to distinctly soft $\Gamma \approx 2.7$-suggests that the X-ray band in PKS 1441+25 can probe different parts of the broadband emission. Harder spectra are consistent with sampling the rising portion of the inverse Compton component or the transition region between synchrotron and inverse Compton components, while softer indices shows the X-ray band is the highest tail of the synchrotron component.

NuSTAR, operating in the 3-79 keV band with its two focal-plane modules (FPMA and FPMB), observed PKS 1441+25 on 2015 April 25. The data were retrieved from MMDC, where all data from *NuSTAR* observations of blazars are uniformly processed and made publicly available [30]. A detailed description of the *NuSTAR* data-analysis is provided in [30]; here we summarize the steps relevant to this work. The analysis was performed using the *NuSTAR_Spectra* pipeline [111], which downloads the raw event files, applies standard *NuSTAR* calibration and screening, and produces science-ready products through the *nuproducts* task. Source photons were extracted from a circular region centered on the source, while background events were taken from an annular region centered on the same position. The radii of the extraction regions were automatically optimized by the pipeline based on the observed count rate, ensuring adequate signal-to-noise in both bright and faint states. The spectra from FPMA and FPMB were then imported into XSPEC [110] and fitted jointly using both power-law and log-parabola models, with Galactic absorption included. Cash statistics [112] were adopted to determine the best-fitting spectral parameters.

The *NuSTAR* observation yields a 3-10 keV flux of $(7.88 \pm 0.32) \times 10^{-12}$: erg cm^{-2} s^{-1} and a 10-30 keV flux of $(5.85 \pm 0.41) \times 10^{-12}$ erg cm^{-2} s^{-1}. The spectrum is relatively soft, with a photon index of 2.18 ± 0.12. This observation coincides with a ustar observation on the same day, for which a photon index of 2.05 ± 0.24 was measured. The combined *SWIFT* and *NuSTAR* data therefore provide continuous coverage of the X-ray spectrum from 0.3 to 30 keV, enabling

a consistent characterization of the spectral shape across the soft and hard X-ray bands.

5.2.3 OPTICAL/UV BAND

Together with the *SWIFT*-XRT observations, PKS 1441+25 was monitored in the optical (V: 500-600 nm, B: 380-500 nm, U: 300-400 nm) and ultraviolet (W1: 260-400 nm, M2: 200-280 nm, W2: 180-260 nm) bands using the Ultra-Violet/Optical Telescope [UVOT; 139] on board *SWIFT* [35]. The UVOT data are retrieved from MMDC, where all *SWIFT*-UVOT blazar observations are uniformly processed and publicly released [30]. A detailed description of the reduction procedure is provided in [30]; here we summarize the key steps relevant to this work. The data were reduced following the standard UVOT data analysis using HEAsoft v6.29 and the latest HEASARC CALDB. Source counts were extracted from a 5-arcsec circular region, while the background was estimated from a nearby 20-arcsec region free of contaminating sources. Count rates were converted into fluxes using the UVOT calibration from [140]. Extinction corrections were applied adopting a reddening value of $E(B-V) = 0.038$, obtained from the Infrared Science Archive[11].

In addition to the *SWIFT*-UVOT observations, MMDC provides additional optical data. Specifically, V- and g-band photometry from ASAS-SN [113] was obtained by querying the public archive within a 5-arcsecond radius around the position of PKS 1441+25. Likewise, photometric measurements in the g, r, and i bands from ZTF [141], as well as g, r, i, z, and y data from Pan-STARRS [142], were retrieved using a 5-arcsecond cone search. The details of these queries, along with the extinction-correction procedure applied to the data sets, are described in [30].

The resulting optical and UV light curves are shown in Figure 5.1, panels (e)-(g). In the optical/UV bands the same general trend seen in the γ-ray and X-ray light curves is present: the source enters a brightening phase beginning around MJD 57000. During this interval, the *SWIFT*-UVOT

[11] http://irsa.ipac.caltech.edu/applications/DUST/

observations show a pronounced increase in flux, with the highest value of $(8.03 \pm 0.18) \times 10^{-12}$ erg cm^{-2} s^{-1} measured in the U filter at MJD 57132.24. Across this active period, a large fraction of the UVOT measured fluxes exceed 10^{-12} erg cm^{-2} s^{-1}. The enhanced optical activity is most evident in panel (g), where the Pan-STARRS and ZTF data indicate that the source remained in a relatively low state prior to MJD 57000 and again after MJD 58000, while the ASAS-SN measurements show a clear brightening between MJD 57000 and 57300. The highest flux in the ASAS-SN data is $(1.05 \pm 0.16) \times 10^{-11}$ erg cm^{-2} s^{-1} observed at MJD 60098.35.

In addition to the optical data shown in Figure 5.1, panels (e)-(g), the infrared (IR) emission of PKS 1441+25 was examined using observations from the Near-Earth Object Wide-field Infrared Survey Explorer [NEOWISE; 114]. The NEOWISE measurements, retrieved from MMDC [30], include only the 3.4 and 4.6μm bands. Because NEOWISE obtains data in short intervals repeated every six months, measurements separated by less than 10 days were combined using a weighted mean to improve the temporal sampling. The resulting IR light curve is shown in Figure 5.1, panel (h), which reveals that the source entered a bright state between MJD 57000-57500. During this interval, the flux peaked at $(3.23 \pm 0.02) \times 10^{-12}$ erg cm^{-2} s^{-1}, while in its typical state the flux remains in the range $(2.00\text{-}3.00) \times 10^{-13}$ erg cm^{-2} s^{-1}. These IR measurements are particularly important because [143] demonstrated that the spectral slope between 3.4 and 4.6μm provides a predictor for the synchrotron peak frequency in blazar SEDs. Thus, variations in the IR flux and spectral slope may reflect changes in the synchrotron component of PKS 1441+25 emission.

5.3 ORIGIN OF MULTIWAVELENGTH EMISSION FROM PKS 1441+25

The multiwavelength light curve shown in Figure 5.1 illustrates the temporal evolution of PKS 1441+25 and provides a basis for defining distinct intervals for theoretical modeling. To increase the statistical quality of the γ-ray spectra, the light curve is segmented into intervals of approximately constant flux using the

Bayesian Blocks algorithm (solid line in Figure 5.1 panel a). This procedure groups observations with similar flux levels, and the resulting merged data sets yield spectra that extend to higher energies, which is essential for robust theoretical modeling. For each Bayesian Block interval, we also search for contemporaneous multiwavelength observations, then investigate the SEDs with contemporaneous data. Based on this approach, the following periods were selected for detailed modeling:

- **29-30 January**: a period of enhanced HE γ-ray activity with simultaneous *SWIFT* coverage.
- **24 April-28 April**: an interval coincident with *SWIFT* and *NuSTAR* observations, as well as VHE γ-ray detections by VERITAS.
- **01-15 May and 01-04 June**: two intervals during which the source remained in a quiescent state across all monitored bands.

Selecting intervals that span both active and quiescent states enables investigation of the physical changes in the jet that give rise to emission extending into the VHE γ-ray band.

5.3.1 THEORETICAL MODELING

The SEDs corresponding to the selected periods are modeled within a one-zone EIC framework, commonly adopted for FSRQs [16–19]. In this scenario, the low-energy component is produced by synchrotron radiation from relativistic electrons, while the high-energy component arises from inverse Compton scattering of both synchrotron photons (SSC) and external photon fields. The latter may include radiation from the accretion disk, photons reprocessed in the BLR, and infrared emission from the dusty torus.

The modeling is performed through MMDC using the neural-network-based methodology presented in [34]. This approach replaces computationally expensive numerical calculations with a convolutional neural network (CNN) trained on physically motivated radiative simulations, enabling efficient and

self-consistent modeling of blazar broadband emission, including particle injection and cooling. Similar surrogate-modeling strategies for SSC scenarios and lepto-hadronic cases are described in [3] and [27], respectively. Here, a brief description of the CNN-based method is provided, and a a full description is provided in [34] for a full description.

In this model, the electrons are injected into a spherical emission region of radius R, filled with a uniform magnetic field B. The electron injection prescription and its luminosity normalization follow Equations 1.4 and 1.5. The emission region moves with bulk Lorentz factor Γ and is viewed at an angle $\sim 1/\Gamma$, yielding a Doppler factor $\delta \simeq \Gamma$. The electrons interact with both internal synchrotron photons as well as external photons from (i) the accretion disk, (ii) the BLR, and (iii) the dusty torus. The accretion disk is modeled following the standard [144] thin-disk model. The BLR is treated as a spherical shell at

$$R_{\rm BLR} = 10^{17}\ {\rm cm}\ \left(\frac{L_d}{10^{45}\ {\rm erg\,s^{-1}}}\right)^{1/2}, \tag{5.1}$$

reprocessing a fraction $f_{\rm BLR} = 0.1$ of the disk luminosity and emitting as a black-body spectrum peaking at $\nu_{\rm BLR} = 2.47 \times 10^{15}$ Hz [21]. The dusty torus is modeled as a spherical shell located at

$$R_{\rm DT} = 2.5 \times 10^{18}\ {\rm cm}\ \left(\frac{L_d}{10^{45}\ {\rm erg\,s^{-1}}}\right)^{1/2}, \tag{5.2}$$

reprocessing a fraction $f_{\rm DT} = 0.5$ of the disk luminosity and emitting a black-body spectrum peaking at $\nu_{\rm IR} = 3 \times 10^{13}$ Hz.

In this case the model contains nine parameters p, $\gamma_{\rm min}$, $\gamma_{\rm max}$, B, R, δ, $L_{\rm e}$, L_d and the mass of the central supermassive black-hole $M_{\rm BH}$. For very broad range of these parameters, the SEDs are computed using the *SOPRANO* code [118]. These simulations form the training data set for the CNN, which learns the mapping between physical parameters and the resulting radiative output. The trained network is then used instead of the numerical code to model the observed SEDs.

Table 5.7: Best-fit physical parameters obtained from modeling the SEDs of PKS 1441+25 during the four different periods. For each interval, the table lists the electron injection index p, the cutoff Lorentz factor $\gamma_{\rm cut}$, the Doppler factor δ, the magnetic-field strength B, the radius of the emitting region R, and the electron kinetic luminosity $L_{\rm e}$. The magnetic luminosity $L_{\rm B}$ is computed from the fitted B, R, and δ.

Parameter	29–30 Jan 2015	24–28 Apr 2015	01–15 May 2015	01–04 Jun 2015
p	2.40 ± 0.52	2.41 ± 0.20	2.33 ± 0.29	2.38 ± 0.35
$\log \gamma_{\rm cut}$	3.71 ± 1.21	4.94 ± 0.19	5.04 ± 0.42	4.41 ± 0.96
δ	42.62 ± 8.04	45.36 ± 7.46	32.47 ± 7.85	39.53 ± 6.97
$\log B$	0.77 ± 0.26	-1.66 ± 0.36	-1.74 ± 0.50	-1.79 ± 0.80
$\log R$	15.03 ± 0.91	17.10 ± 0.44	17.17 ± 0.44	17.13 ± 0.52
$\log L_{\rm e}$	44.98 ± 0.83	45.99 ± 0.24	45.92 ± 0.56	46.08 ± 0.58
$\log L_{\rm B}$	44.43	43.77	43.46	43.44

5.3.2 MODELING RESULTS

The CNN-based EIC, SSC, and lepto-hadronic models described above are publicly available through the MMDC data center. The trained neural networks are interfaced with the Bayesian inference framework of MultiNest [86], enabling efficient nested sampling and determination of the parameter sets that best describe the observed SEDs. For all fits, MultiNest was run with 1500 active points and a tolerance of 0.4, ensuring adequate exploration of the parameter space and convergence of the posterior distributions. Because the low-energy (radio/IR) data are sparse or unavailable for the selected periods, we fixed the minimum Lorentz factor to $\gamma_{\rm min} = 100$ during the fit. The accretion disk luminosity was fixed to $L_{\rm d} = 2 \times 10^{45}$ erg s^{-1}, and the black-hole mass to $M_{\rm BH} = 6.76 \times 10^{7} M_{\odot}$. Absorption by the extragalactic background light (EBL) is included by adopting the model of [88].

The modeled SEDs for the four activity periods are shown in Figure 5.2, and the corresponding best-fit parameters are summarized in Table 5.7. All intervals can be reproduced within a one-zone EIC framework, but the physical conditions inferred from the fits vary in a systematic way across the epochs. During the quiescent period between 1–15 May (Figure 5.2 left bottom panel), the SED is explained by a moderately energetic electron population with a relatively high cutoff energy, $\log \gamma_{\rm cut} \simeq 5.0$ so that the HE tail of the synchrotron components can reach X-ray band, and a Doppler factor of about 32.5. The magnetic field is weak $\log B \approx -1.7$, and the emitting region is comparatively large $\log R \approx 17.2$.

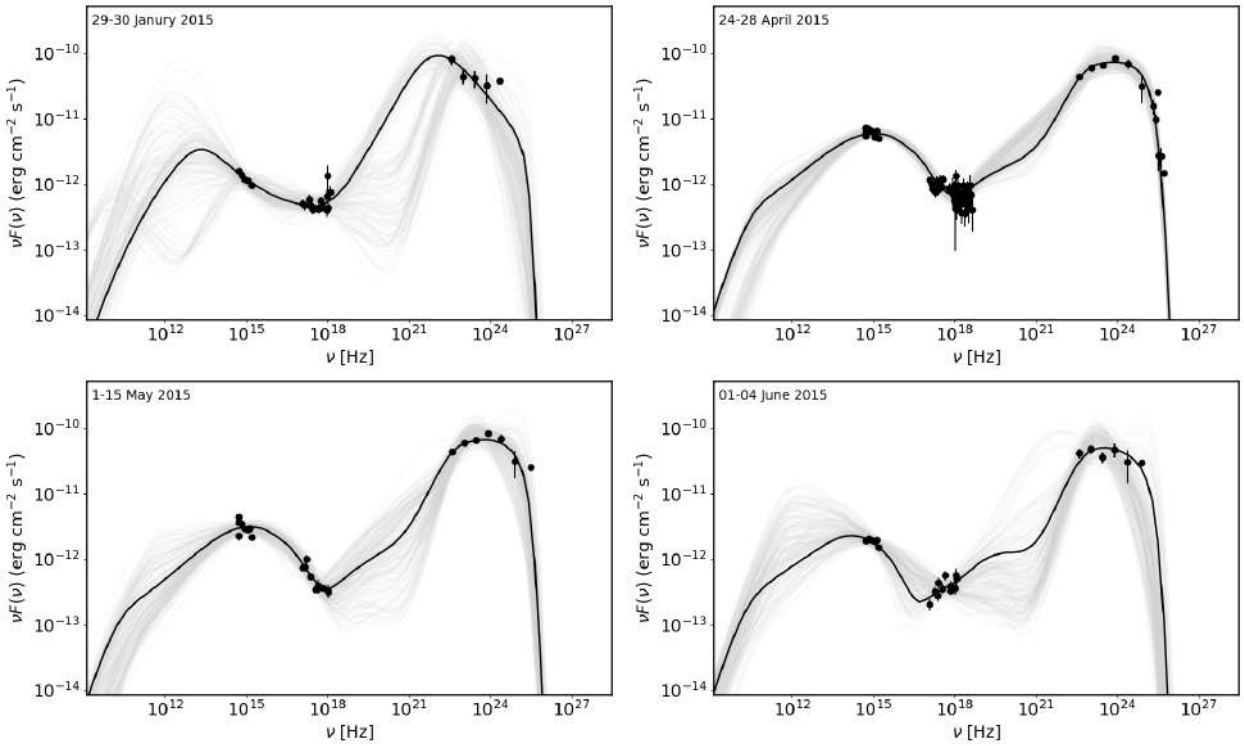

Figure 5.2: SED of PKS 1441+25 for the four different intervals selected from the multiwavelength light curve: 29-30 January 2015, 24-28 April 2015, 01-15 May 2015, and 01-04 June 2015. Black points show the contemporaneous multiwavelength data used in each fit. The solid black curve in each panel represents the best-fit one-zone EIC model obtained with the CNN-accelerated inference framework, while the grey curves correspond to random posterior realizations from the MultiNest sampling.

These conditions implies that the source emission is Compton-dominated, where the external radiation field efficiently boosts the inverse-Compton component without requiring either strong magnetic fields or extremely compact emission zones can explain the observed HE γ-ray data.

In the 1-4 June interval (Figure 5.2 right bottom panel), the overall SED shape remains similar but with X-ray data describing the increasing part of tye inverse Compton component (SSC). This is case the fit yields an increase in the bulk motion of the emitting region, with the Doppler factor rising to ~ 40. At the same time, the electron energy distribution shifts toward slightly lower cutoff energies ($\log \gamma_{\rm cut} \simeq 4.4$ versus $\log \gamma_{\rm cut} \simeq 5.0$). Despite this reduction, the higher Doppler boosting allows the inverse Compton scattering of the external photon fields to explain the HE γ-ray data. The magnetic field is low and comparable to the value estimated in modeling the SED in May, but the electron luminosity increases, suggesting that the enhanced emission is primarily driven by a larger number

of radiating electrons rather than changes in geometry or magnetization.

The changes in the SED are observed during the flaring periods. The SED during 29-30 January (Figure 5.2 left upper panel) episode shows a different set of parameters required to explain the SED. Here, the model requires a much more compact emitting region (with $\log R \approx 15$) and a significantly stronger magnetic field of $\log B \approx 0.8$. Such a configuration naturally shifts more power into the synchrotron component and can accommodate rapid variability. The Doppler factor remains high ~ 43, but the cutoff energy is lower and less well constrained due to the more limited X-ray coverage in this interval. This combination of compact size and enhanced magnetization distinguishes this SED modeling from all other periods.

The SED observed during 24-28 April SED when also VHE γ-ray emission were observed from PKS 1441+25 is shown in Figure 5.2 right upper panel. The emitting region size and magnetic field are similar to the quiescent state, but the Doppler factor increases to ~ 45, and the electron luminosity is slightly higher. The cutoff energy is well determined and close to $\log \gamma_{\rm cut} \approx 4.9$, producing a HE peak that extends also to VHE γ-ray band. Therefore in this period the enhanced boosting strengthens the HE component without substantial changes in the underlying magnetic or geometric conditions.

The multi-epoch modeling presented here is consistent with earlier modeling of PKS 1441+25, but it shows a more clear picture of how the jet conditions changes in different periods. A direct comparison between the parameters obtained here and those reported in previous modeling efforts is not possible because (i) different data sets were used, and *(ii)* the fits presented here rely on Bayesian nested sampling, whereas earlier studies typically employed local minimization procedures or even qualitative, by-eye adjustments. For example, [137] showed that during April the emission zone must have been located well outside the BLR so the 200 GeV can escape from the region which would be otherwise be absorbed by BLR photons. Their modeling required a relatively large emitting region and weak magnetic field, conditions similar with those

inferred from the modeling of SEDs in April, May, and June which yielded extended, low-B, Compton-dominated regions. Similarly, [99] also showed that the April flare was associated with a hardened electron distribution and increased Compton dominance, which was interpreted as either an increase in the bulk Lorentz factor or enhanced magnetic fields within an emission region already located beyond the BLR.

5.4 DISCUSSION

The multi-epoch modeling reveals clear differences in the physical conditions of the emission region across the 2015 activity periods of PKS 1441+25. In the current modeling approach the emission-region radius, R, inferred directly from the SED fits is linked with the the distance of the emitting zone from the central black hole. Importantly, we did not impose any prior assumption about the location of the emitting region; rather, the fits naturally converged to different values of R for each epoch, allowing to infer the dominant external radiation fields contributing to the EIC component as well as the possible location of the emission region.

For the three SEDs observed during April, May, and June, the modeling results in a large emission-region radii, with $\log R \sim 17$. Such sizes correspond to distances well beyond the radius of the BLR. For a disk luminosity of $L_{\rm d} = 2 \times 10^{45}$ erg s^{-1}, the BLR is expected to extend to $R_{\rm BLR} \simeq 10^{17}$ cm, after which the energy density of BLR photons drops rapidly. At these larger distances, the dominant external photon field becomes the infrared radiation from the dusty torus. The SEDs of April-June display spectral shapes that are fully consistent with this picture: the inverse-Compton peak is bright and smooth, without signatures of γ-ray attenuation, and the magnetic fields remain weak, placing the source in a Compton-dominated regime typical of emission occurring outside the BLR. These epochs therefore support a scenario in which the dissipation region is located beyond the BLR and interacts primarily with torus photons.

The SED during the flare in January differs from this pattern. In this epoch, the modeling shows a smaller emitting-region radius, implying a location

significantly closer to the central engine. At such distances—well inside 10^{17} cm-the energy density of external fields is dominated by direct accretion-disk radiation (mostly) and its reprocessed component from the BLR. In this case, the disk photon fields plays an important role in shaping the HE component, and the reduced distance naturally explains the spectral differences compared to the SEDs from the other periods. In this case, although the γ-ray flux increases, the spectrum remains soft and does not extend into the VHE regime—a behavior naturally expected if VHE photons are absorbed within the BLR, supporting a scenario in which the emission region is located inside the BLR. The January emission zone therefore appears to represent an earlier, upstream dissipation event occurring at a location where the disk and BLR contributions are non-negligible.

Together, these results suggest an evolution of the emitting region along the jet: a compact, magnetically stronger zone located closer to the black hole during the January event, followed by dissipation episodes occurring farther in April-June where the torus radiation field dominates. This interpretation is physically consistent with both the change in SED shapes and the systematic increase in R inferred from the modeling. The smooth transition across these epochs indicates that PKS 1441+25 did not undergo a change in the emission mechanism but rather a shift in the location of the dissipation region, naturally producing the observed differences in Compton dominance, spectral hardness, and variability properties.

This scenario is further supported by the jet energetics. The electron kinetic power, $L_{\rm e}$, shows a systematic increase for the SED obtained in January 2015 compared with the SEDs modeled for April-June. During the latter periods, $L_{\rm e}$ reaches values of order 10^{46} erg s^{-1}, while the magnetic power, computed as $L_{\rm B} = \pi c R_b^2 \Gamma^2 U_B$, remains almost an order of magnitude lower in these three states, showing a strongly particle-dominated jet once the emission zone moves beyond the BLR, consistent with the weak magnetic fields inferred for these epochs and suggesting that most of the radiative output is carried

by a high density of relativistic electrons rather than by magnetic energy. The January episode differs in this respect: the compact emission region and substantially stronger magnetic field yield a magnetic power comparable to the electron power, making the jet closer to equipartition during this early phase. Such elevated magnetization is naturally expected if dissipation occurs close to the black hole, where the jet is still undergoing collimation and accelerating. The transition from the moderately magnetized January state to the particle-dominated April-June states therefore shows not just a change in emitting-region location but also a redistribution of energy within the jet as it expands and interacts with different external radiation fields.

5.5 SUMMARY

In this work a multiwavelength study of PKS 1441+25 is presented combining *Fermi*-LAT γ-ray data, *SWIFT* XRT/UVOT and *NuSTAR* observations, and ground-based optical and infrared photometry, all uniformly processed and accessed through MMDC. The adaptive-binning analysis of the *Fermi*-LAT light curve shows that the source entered a prolonged high state starting around MJD 57000, during which it exhibited a major HE γ-ray flare in late January and a hard spectra in April when VHE emission from the source were observed. The X-ray, optical/UV, and IR bands show correlated brightening over the same interval, indicating that the entire jet emission zone underwent significant changes in this period.

Dividing the γ-ray light curve into intervals using Bayesian Block algorithm, SEDs from four intervals were selected and modeled within a one-zone EIC framework using novel CNN based method. This approach allowed to efficiently explore the parameter space and to derive posterior distributions for the physical parameters governing the emitting region. For the three SEDs obtained in April, May, and June, the modeling yields large emission-region radii, $\log R \sim 17$, weak magnetic fields, and electron kinetic powers exceeding the magnetic power by almost an order of magnitude. These conditions correspond to dissipation occurring well outside the BLR, where the energy density of

BLR photons has already declined and the infrared radiation from the dusty torus dominates the external photon field. The resulting SEDs are strongly Compton-dominated, with smooth high-energy components extending into the VHE band during the April interval, consistent with the detection of VHE γ-raysfrom PKS 1441+25 and with previous single-epoch modeling of the April flare.

The January flare displays a different set of physical conditions. In this epoch the fits resulted in a smaller emission region, $\log R \sim 15$, and a substantially stronger magnetic field, such that the magnetic and electron powers are closer to equipartition. At these smaller radii the dominant external fields are the direct accretion-disk radiation and its reprocessed component in the BLR. The soft HE spectrum and the absence of VHE emission are naturally explained if the emitting region is located inside the BLR, where γ-γ absorption suppresses the escape of the highest-energy photons. This is the most likely reason why, despite the January episode being significantly brighter in the γ-ray band than the later activity periods, no VHE photons were detected.

These results support a picture in which the 2015 activity of PKS 1441+25 is a results not only a change of the emission mechanism, but by a relocation and evolution of the dissipation region along the jet. The jet appears to transition from a compact, near-equipartition zone at distances with the BLR close to the central source, to an extended, particle-dominated region beyond the BLR, with the dominant external photon field changing from disk/BLR to torus radiation. This evolution naturally accounts for the observed differences in Compton dominance, spectral hardness, and variability, and provides a self-consistent explanation for the occurrence of VHE emission only during the April episode.

CONCLUSION

In this thesis, machine learning methods were applied to the statistical classification of blazar populations and the physical modeling of their broadband radiation. The main goal was to improve prediction accuracy, and to make the study of large blazar samples and time-resolved SEDs more practical. The obtained results show that machine learning can be used as a useful tool both for population studies and for the interpretation of multiwavelength emission.

The first chapter presented an introduction to blazars as well as the machine learning methods used in this thesis.

The second chapter addressed the classification of blazar candidates of uncertain type in the *Fermi*-LAT 4FGL-DR3 catalog. Using 18 γ-ray spectral and temporal features, gradient boosting models were trained to distinguish BL Lacs and FSRQs. The models reached strong performance, with ROC–AUC values of about 0.87–0.93. When applied to 1493 BCUs, they provided subclass predictions for about 1230 sources, reducing the unclassified fraction from about 40% to nearly 5%. This result is important because it makes the available blazar sample much more complete and more useful for population studies, source selection, and statistical studies of jet properties.

The third chapter presented the development of a fast machine learning framework for SED modeling. A CNN surrogate was built to reproduce one-zone SSC radiative calculations with high accuracy. The model successfully learned the mapping between physical parameters and the resulting synchrotron and inverse Compton components. The main advantage of this approach is the speed: the evaluation time was reduced from about 10–100 seconds for numerical calculations to about 10^{-2}–10^{-3} seconds. This speedup makes broad parameter searches and Bayesian inference much more practical, especially when many repeated model evaluations are needed. In this way, the surrogate model makes it possible to make studies that would otherwise be too computationally expensive.

In the fourth chapter, this framework was then applied to the time-resolved study of PKS 2155-304. A large sample of 253 multiwavelength SEDs was assembled and modeled in a systematic way within a one-zone SSC scenario. This made it possible to follow the physical evolution of the source across different activity states instead of studying only a few isolated epochs. The modeling showed that the variability is linked to changes in several physical parameters, especially the magnetic field B, electron luminosity L_e, maximum electron energy $\gamma_{\rm max}$, and Doppler factor δ. The results also showed that the electron spectrum becomes harder during γ-ray flares, while X-ray flares are connected with higher magnetization. In all studied states, the jet remained particle dominated, with $\eta_B \simeq 0.09$–0.17. Overall, the results suggest that the observed variability is mainly driven by changes in particle acceleration efficiency and in the level of magnetization in the emitting region.

In the fifth chapter, the origin of the multiwavelength emission from FSRQ PKS 1441+25 is studied using multi-epoch SEDs from the IR to the γ-ray band. The modeling was performed within a one-zone EIC scenario. The results indicate two clearly different emission states. During the January high-energy flare, the emission region was compact, with a size of about 10^{15} cm, and located within or close to the BLR. During the April–June period, including the VHE detection, the emitting region became much larger, about 10^{17} cm, and moved beyond the BLR. This change shifted the dominant seed photon field from the BLR to the dusty torus and strongly reduced $\gamma\gamma$ absorption, allowing photons above 100 GeV to escape. Therefore, the main conclusion is that the observed change in the emission is controlled mostly by the evolution of the dissipation region along the jet, rather than by a change of the basic radiation mechanism.

In conclusion, the results of this thesis show that machine learning can be used to study the physical properties of blazars and make large-scale computations practical, while keeping the analysis physically grounded.

BIBLIOGRAPHY

[1] R. D. Blandford and J. P. Ostriker, “Particle acceleration by astrophysical shocks.” *The Astrophysical Journal Letters*, vol. 221, pp. L29–L32, 1978.

[2] P. Padovani *et al.*, “Active galactic nuclei: what’s in a name?” *Astronomy & Astrophysics Review*, vol. 25, p. 2, 2017.

[3] D. Bégué *et al.*, “Modeling Blazar Broadband Emission with a Convolutional Neural Network. I. Synchrotron Self-Compton Model,” *The Astrophysical Journal*, vol. 963, p. 71, 2024.

[4] A. Mastichiadis and J. G. Kirk, “Self-consistent particle acceleration in active galactic nuclei.” *Astronomy & Astrophysics*, vol. 295, p. 613, 1995.

[5] C. M. Urry and P. Padovani, “Unified Schemes for Radio-Loud Active Galactic Nuclei,” *Publications of the Astronomical Society of the Pacific*, vol. 107, p. 803, 1995.

[6] V. Beckmann and C. R. Shrader, *Active Galactic Nuclei*, 2012.

[7] IceCube Collaboration *et al.*, “Multimessenger observations of a flaring blazar coincident with high-energy neutrino IceCube-170922A,” *Science*, vol. 361, p. eaat1378, 2018.

[8] IceCube Collaboration *et al.*, “Neutrino emission from the direction of the blazar TXS 0506+056 prior to the IceCube-170922A alert,” *Science*, vol. 361, pp. 147–151, 2018.

[9] P. Padovani *et al.*, “Dissecting the region around IceCube-170922A: the blazar TXS 0506+056 as the first cosmic neutrino source,” *Monthly Notices of the Royal Astronomical Society*, vol. 480, pp. 192–203, 2018.

[10] S. Abdollahi *et al.*, “Incremental Fermi Large Area Telescope Fourth Source Catalog,” *Astrophysical Journal Supplement Series*, vol. 260, p. 53, 2022.

[11] N. Sahakyan *et al.*, “A multimessenger study of the blazar PKS 0735+178: a new major neutrino source candidate,” *Monthly Notices of the Royal Astronomical Society*, vol. 519, pp. 1396–1408, 2023.

[12] G. Ghisellini, L. Maraschi, and A. Treves, “Inhomogeneous synchrotron-self-compton models and the problem of relativistic beaming of BL Lac objects.” *Astronomy & Astrophysics*, vol. 146, pp. 204–212, 1985.

[13] L. Maraschi, G. Ghisellini, and A. Celotti, “A Jet Model for the Gamma-Ray–emitting Blazar 3C 279,” *The*

Astrophysical Journal Letters, vol. 397, p. L5, 1992.

[14] S. D. Bloom and A. P. Marscher, "An Analysis of the Synchrotron Self-Compton Model for the Multi–Wave Band Spectra of Blazars," *The Astrophysical Journal*, vol. 461, p. 657, 1996.

[15] F. Tavecchio, L. Maraschi, and G. Ghisellini, "Constraints on the Physical Parameters of TeV Blazars," *The Astrophysical Journal*, vol. 509, pp. 608–619, 1998.

[16] C. D. Dermer, R. Schlickeiser, and A. Mastichiadis, "High-energy gamma radiation from extragalactic radio sources." *Astronomy & Astrophysics*, vol. 256, pp. L27–L30, 1992.

[17] C. D. Dermer and R. Schlickeiser, "On the Location of the Acceleration and Emission Sites in Gamma-Ray Blazars," *Astrophysical Journal Supplement Series*, vol. 90, p. 945, 1994.

[18] M. Sikora, M. C. Begelman, and M. J. Rees, "Comptonization of Diffuse Ambient Radiation by a Relativistic Jet: The Source of Gamma Rays from Blazars?" *The Astrophysical Journal*, vol. 421, p. 153, 1994.

[19] M. Błażejowski, M. Sikora, R. Moderski, and G. M. Madejski, "Comptonization of Infrared Radiation from Hot Dust by Relativistic Jets in Quasars," *The Astrophysical Journal*, vol. 545, pp. 107–116, 2000.

[20] C. D. Dermer, J. D. Finke, H. Krug, and M. Böttcher, "Gamma-Ray Studies of Blazars: Synchro-Compton Analysis of Flat Spectrum Radio Quasars," *The Astrophysical Journal*, vol. 692, pp. 32–46, 2009.

[21] G. Ghisellini and F. Tavecchio, "Canonical high-power blazars," *Monthly Notices of the Royal Astronomical Society*, vol. 397, pp. 985–1002, 2009.

[22] M. Sikora, Ł. Stawarz, R. Moderski, K. Nalewajko, and G. M. Madejski, "Constraining Emission Models of Luminous Blazar Sources," *The Astrophysical Journal*, vol. 704, pp. 38–50, 2009.

[23] K. Mannheim and P. L. Biermann, "Photomeson production in active galactic nuclei," *Astronomy & Astrophysics*, vol. 221, pp. 211–220, 1989.

[24] K. Mannheim, "The proton blazar," *Astronomy & Astrophysics*, vol. 269, pp. 67–76, 1993.

[25] A. Mücke and R. J. Protheroe, "A proton synchrotron blazar model for flaring in Markarian 501," *Astroparticle Physics*, vol. 15, pp. 121–136, 2001.

[26] M. Petropoulou and A. Mastichiadis, "Bethe-Heitler emission in BL Lacs: filling

the gap between X-rays and γ-rays," *Monthly Notices of the Royal Astronomical Society*, vol. 447, pp. 36–48, 2015.

[27] N. Sahakyan *et al.*, "Modeling Blazar Broadband Emission with Convolutional Neural Networks. III. Proton Synchrotron and Hybrid Models," *The Astrophysical Journal*, vol. 990, p. 222, 2025.

[28] A. A. Abdo *et al.*, "Fermi Large Area Telescope Observations of Markarian 421: The Missing Piece of its Spectral Energy Distribution," *The Astrophysical Journal*, vol. 736, p. 131, 2011.

[29] G. Harutyunyan, N. Sahakyan, and D. Bégué, "Modelling of the time-resolved spectral energy distribution of blazar OJ 287 from 2008 to 2023: a comprehensive multi-epoch study," *Monthly Notices of the Royal Astronomical Society*, vol. 540, pp. 582–593, 2025.

[30] N. Sahakyan *et al.*, "Markarian Multiwavelength Data Center (MMDC): A Tool for Retrieving and Modeling Multitemporal, Multiwavelength, and Multimessenger Data from Blazar Observations," *The Astronomical Journal*, vol. 168, p. 289, 2024.

[31] C. Bishop, *Neural networks for pattern recognition*. Oxford University Press, USA, 1995.

[32] T. Chen and C. Guestrin, "XGBoost: A Scalable Tree Boosting System," *arXiv e-prints*, p. arXiv:1603.02754, 2016.

[33] G. Ke *et al.*, "Lightgbm: A highly efficient gradient boosting decision tree," in *NIPS*, 2017.

[34] N. Sahakyan *et al.*, "Modeling Blazar Broadband Emission with Convolutional Neural Networks. II. External Compton Model," *The Astrophysical Journal*, vol. 971, p. 70, 2024.

[35] N. Gehrels *et al.*, "The Swift Gamma-Ray Burst Mission," *The Astrophysical Journal*, vol. 611, pp. 1005–1020, 2004.

[36] W. B. Atwood *et al.*, "The Large Area Telescope on the Fermi Gamma-Ray Space Telescope Mission," *The Astrophysical Journal*, vol. 697, pp. 1071–1102, 2009.

[37] S. Abdollahi *et al.*, "Fermi Large Area Telescope Fourth Source Catalog," *Astrophysical Journal Supplement Series*, vol. 247, p. 33, 2020.

[38] T. M. Mitchell, *Machine learning*. McGraw-hill New York, 1997, vol. 1, no. 9.

[39] J. K. Kim, K.-H. Kim, and S. Choi, *Supervised Learning*. Boston, MA: Springer US, 2009, pp. 1298–1303, doi: 10.1007/978-0-387-73003-5_302.

[40] K. O'Shea and R. Nash, "An Introduction to Convolutional Neural Networks," *arXiv e-prints*, p. arXiv:1511.08458, 2015.

[41] G. Chiaro, D. Salvetti, G. La Mura, M. Giroletti, D. J. Thompson, and D. Bastieri, "Blazar flaring patterns (B-FlaP) classifying blazar candidate of uncertain type in the third Fermi-LAT catalogue by artificial neural networks," *Monthly Notices of the Royal Astronomical Society*, vol. 462, pp. 3180–3195, 2016.

[42] D. Salvetti, G. Chiaro, G. La Mura, and D. J. Thompson, "3FGLzoo: classifying 3FGL unassociated Fermi-LAT γ-ray sources by artificial neural networks," *Monthly Notices of the Royal Astronomical Society*, vol. 470, pp. 1291–1297, 2017.

[43] B. Arsioli and P. Dedin, "Machine learning applied to multifrequency data in astrophysics: blazar classification," *Monthly Notices of the Royal Astronomical Society*, vol. 498, pp. 1750–1764, 2020.

[44] G. Chiaro, M. Kovacevic, and G. La Mura, "4FGLzoo. Classifying Fermi-LAT uncertain gamma-ray sources by machine learning analysis," *Journal of High Energy Astrophysics*, vol. 29, pp. 40–42, 2021.

[45] B. M. O. Fraga *et al.*, "Deep learning Blazar classification based on multifrequency spectral energy distribution data," *Monthly Notices of the Royal Astronomical Society*, vol. 505, pp. 1268–1279, 2021.

[46] A. Butter, T. Finke, F. Keil, M. Krämer, and S. Manconi, "Classification of Fermi-LAT blazars with Bayesian neural networks," *Journal of Cosmology and Astroparticle Physics*, vol. 2022, p. 023, 2022.

[47] M. Ajello *et al.*, "The Fourth Catalog of Active Galactic Nuclei Detected by the Fermi Large Area Telescope," *The Astrophysical Journal*, vol. 892, p. 105, 2020.

[48] T. Auld, M. Bridges, M. P. Hobson, and S. F. Gull, "Fast cosmological parameter estimation using neural networks," *Monthly Notices of the Royal Astronomical Society: Letters*, vol. 376, pp. L11–L15, 2007.

[49] S. Dieleman, K. W. Willett, and J. Dambre, "Rotation-invariant convolutional neural networks for galaxy morphology prediction," *Monthly Notices of the Royal Astronomical Society*, vol. 450, pp. 1441–1459, 2015.

[50] S. He *et al.*, "Learning to predict the cosmological structure formation," *Proceedings of the National Academy of Sciences*, vol. 116, pp. 13 825–13 832, 2019.

[51] Kovačević, M. , G. Chiaro, S. Cutini, and G. Tosti, "Optimizing neural network techniques in classifying Fermi-LAT gamma-ray sources," *Monthly Notices of the Royal Astronomical Society*, vol. 490, pp. 4770–4777, 2019.

[52] M. Kovačević, G. Chiaro, S. Cutini, and G. Tosti, "Classification of blazar

candidates of uncertain type from the Fermi LAT 8-yr source catalogue with an artificial neural network," *Monthly Notices of the Royal Astronomical Society*, vol. 493, pp. 1926–1935, 2020.

[53] J. Coronado-Blázquez, "Classification of Fermi-LAT unidentified gamma-ray sources using CATBOOST gradient boosting decision trees," *Monthly Notices of the Royal Astronomical Society*, vol. 515, pp. 1807–1814, 2022.

[54] A. Golob, M. Sawicki, A. D. Goulding, and J. Coupon, "Classifying stars, galaxies, and AGNs in CLAUDS + HSC-SSP using gradient boosted decision trees," *Monthly Notices of the Royal Astronomical Society*, vol. 503, pp. 4136–4146, 2021.

[55] X. Jin, Y. Zhang, J. Zhang, Y. Zhao, X.-b. Wu, and D. Fan, "Efficient selection of quasar candidates based on optical and infrared photometric data using machine learning," *Monthly Notices of the Royal Astronomical Society*, vol. 485, pp. 4539–4549, 2019.

[56] Z. Yi *et al.*, "An Efficient Spectral Selection of M Giants Using XGBoost," *The Astrophysical Journal*, vol. 887, p. 241, 2019.

[57] M. Ackermann *et al.*, "The Third Catalog of Active Galactic Nuclei Detected by the Fermi Large Area Telescope," *The Astrophysical Journal*, vol. 810, p. 14, 2015.

[58] M. Ajello *et al.*, "The Fourth Catalog of Active Galactic Nuclei Detected by the Fermi Large Area Telescope: Data Release 3," *Astrophysical Journal Supplement Series*, vol. 263, p. 24, 2022.

[59] A. Mücke, R. J. Protheroe, R. Engel, J. P. Rachen, and T. Stanev, "BL Lac objects in the synchrotron proton blazar model," *Astroparticle Physics*, vol. 18, pp. 593–613, 2003.

[60] M. Böttcher, A. Reimer, K. Sweeney, and A. Prakash, "Leptonic and Hadronic Modeling of Fermi-detected Blazars," *The Astrophysical Journal*, vol. 768, p. 54, 2013.

[61] S. Gasparyan, D. Bégué, and N. Sahakyan, "Time-dependent lepto-hadronic modelling of the emission from blazar jets with SOPRANO: the case of TXS 0506 + 056, 3HSP J095507.9 + 355101, and 3C 279," *Monthly Notices of the Royal Astronomical Society*, vol. 509, pp. 2102–2121, 2022.

[62] V. Zabalza, "naima: a python package for inference of relativistic particle energy distributions from observed nonthermal spectra," *Proc. of International Cosmic Ray Conference 2015*, p. 922, 2015.

[63] A. Tramacere, P. Giommi, M. Perri, F. Verrecchia, and G. Tosti, "Swift observations of the very intense flaring activity of Mrk 421 during 2006. I. Phenomenological picture of electron acceleration and predictions for MeV/GeV

emission," *Astronomy & Astrophysics*, vol. 501, pp. 879–898, 2009.

[64] A. Tramacere, E. Massaro, and A. M. Taylor, "Stochastic Acceleration and the Evolution of Spectral Distributions in Synchro-Self-Compton Sources: A Self-consistent Modeling of Blazars' Flares," *The Astrophysical Journal*, vol. 739, p. 66, 2011.

[65] A. Tramacere, "JetSeT: Numerical modeling and SED fitting tool for relativistic jets," Astrophysics Source Code Library, record ascl:2009.001, p. ascl:2009.001, 2020.

[66] C. Nigro, J. Sitarek, P. Gliwny, D. Sanchez, A. Tramacere, and M. Craig, "agnpy: An open-source python package modelling the radiative processes of jetted active galactic nuclei," *Astronomy & Astrophysics*, vol. 660, p. A18, 2022.

[67] S. Gao, M. Pohl, and W. Winter, "On the Direct Correlation between Gamma-Rays and PeV Neutrinos from Blazars," *The Astrophysical Journal*, vol. 843, p. 109, 2017.

[68] M. Cerruti, A. Zech, C. Boisson, and S. Inoue, "A hadronic origin for ultra-high-frequency-peaked BL Lac objects," *Monthly Notices of the Royal Astronomical Society*, vol. 448, pp. 910–927, 2015.

[69] S. I. Stathopoulos, M. Petropoulou, G. Vasilopoulos, and A. Mastichiadis, "LeHaMoC: a versatile time-dependent lepto-hadronic modeling code for high-energy astrophysical sources," *arXiv e-prints*, p. arXiv:2308.06174, 2023.

[70] H. Abe *et al.*, "Multimessenger Characterization of Markarian 501 during Historically Low X-Ray and γ-Ray Activity," *Astrophysical Journal Supplement Series*, vol. 266, p. 37, 2023.

[71] E. Sobacchi and Y. E. Lyubarsky, "On the magnetization and the radiative efficiency of BL Lac jets," *Monthly Notices of the Royal Astronomical Society*, vol. 484, pp. 1192–1201, 2019.

[72] F. Tavecchio and E. Sobacchi, "Anisotropic electron populations in BL Lac jets: consequences for the observed emission," *Monthly Notices of the Royal Astronomical Society*, vol. 491, pp. 2198–2204, 2020.

[73] S. L. Odell, "Radiation force on a relativistic plasma and the Eddington limit," *The Astrophysical Journal Letters*, vol. 243, pp. L147–L149, 1981.

[74] T. Vuillaume, G. Henri, and P.-O. Petrucci, "Variation of bulk Lorentz factor in AGN jets due to Compton rocket in a complex photon field," *Astronomy & Astrophysics*, vol. 581, p. A18, 2015.

[75] M. Böttcher and M. G. Baring, "Multi-wavelength Variability Signatures of Relativistic Shocks in Blazar Jets," *The Astrophysical Journal*, vol. 887, p. 133,

2019.

[76] Z.-Y. Yan, J. Yang, X.-H. Zhao, Y.-Z. Meng, and B.-B. Zhang, “One Fits All: A Unified Synchrotron Model Explains GRBs with FRED-Shaped Pulses,” *arXiv e-prints*, p. arXiv:2308.00772, 2023.

[77] J. M. Burgess, “ronswanson: Building Table Models for 3ML,” *The Journal of Open Source Software*, vol. 8, p. 4969, 2023.

[78] J. G. Kirk, A. W. Guthmann, Y. A. Gallant, and A. Achterberg, “Particle Acceleration at Ultrarelativistic Shocks: An Eigenfunction Method,” *The Astrophysical Journal*, vol. 542, pp. 235–242, 2000.

[79] L. Sironi and A. Spitkovsky, “Particle Acceleration in Relativistic Magnetized Collisionless Electron-Ion Shocks,” *The Astrophysical Journal*, vol. 726, p. 75, 2011.

[80] D. A. Uzdensky, “Relativistic non-thermal particle acceleration in two-dimensional collisionless magnetic reconnection,” *Journal of Plasma Physics*, vol. 88, p. 905880114, 2022.

[81] M. D. McKay, R. J. Beckman, and W. J. Conover, “A comparison of three methods for selecting values of input variables in the analysis of output from a computer code,” *Technometrics*, vol. 42, pp. 55–61, 2000.

[82] F. A. Viana, “A tutorial on latin hypercube design of experiments,” *Quality and reliability engineering international*, vol. 32, pp. 1975–1985, 2016.

[83] C. Kamath, “Intelligent sampling for surrogate modeling, hyperparameter optimization, and data analysis,” *Machine Learning with Applications*, vol. 9, p. 100373, 2022.

[84] A. Keivani *et al.*, “A Multimessenger Picture of the Flaring Blazar TXS 0506+056: Implications for High-energy Neutrino Emission and Cosmic-Ray Acceleration,” *The Astrophysical Journal*, vol. 864, p. 84, 2018.

[85] S. I. Stathopoulos, M. Petropoulou, P. Giommi, G. Vasilopoulos, P. Padovani, and A. Mastichiadis, “High-energy neutrinos from X-rays flares of blazars frequently observed by the Swift X-ray Telescope,” *Monthly Notices of the Royal Astronomical Society*, vol. 510, pp. 4063–4079, 2022.

[86] F. Feroz, M. P. Hobson, and M. Bridges, “MULTINEST: an efficient and robust Bayesian inference tool for cosmology and particle physics,” *Monthly Notices of the Royal Astronomical Society*, vol. 398, pp. 1601–1614, 2009.

[87] MAGIC Collaboration *et al.*, “Broadband characterisation of the very intense TeV flares of the blazar 1ES 1959+650 in 2016,” *Astronomy & Astrophysics*, vol. 638, p. A14, 2020.

[88] A. Domínguez *et al.*, "Extragalactic background light inferred from AEGIS galaxy-SED-type fractions," *Monthly Notices of the Royal Astronomical Society*, vol. 410, pp. 2556–2578, 2011.

[89] G. Vianello *et al.*, "The Multi-Mission Maximum Likelihood framework (3ML)," *ArXiv e-prints*, 2015.

[90] O. M. Boersma and J. van Leeuwen, "DeepGlow: An efficient neural network emulator of physical afterglow models for gamma-ray bursts and gravitational-wave events," *Publications of the Astronomical Society of Australia*, vol. 40, p. e030, 2023.

[91] S. Bowyer, J. Brodie, J. T. Clarke, and J. P. Henry, "Optical observations of the BL Lacertae object PKS 2155-304 and implications regarding the X-ray absorption feature at 600-700 eV." *The Astrophysical Journal Letters*, vol. 278, pp. L103–L107, 1984.

[92] J. Kataoka *et al.*, "Variability Pattern and the Spectral Evolution of the BL Lacertae Object PKS 2155-304," *The Astrophysical Journal*, vol. 528, pp. 243–253, 2000.

[93] F. Aharonian *et al.*, "An Exceptional Very High Energy Gamma-Ray Flare of PKS 2155-304," *The Astrophysical Journal Letters*, vol. 664, pp. L71–L74, 2007.

[94] D. Tripathi *et al.*, "Firmamento: A Multimessenger Astronomy Tool for Citizen and Professional Scientists," *The Astronomical Journal*, vol. 167, p. 116, 2024.

[95] N. Sahakyan *et al.*, "Modeling blazar broadband emission with convolutional neural networks. iii. proton synchrotron and hybrid models," *The Astrophysical Journal*, vol. 990, p. 222, 2025.

[96] B. Lott, L. Escande, S. Larsson, and J. Ballet, "An adaptive-binning method for generating constant-uncertainty/constant-significance light curves with Fermi-LAT data," *Astronomy & Astrophysics*, vol. 544, p. A6, 2012.

[97] B. Rani, B. Lott, T. P. Krichbaum, L. Fuhrmann, and J. A. Zensus, "Constraining the location of rapid gamma-ray flares in the flat spectrum radio quasar 3C 273," *Astronomy & Astrophysics*, vol. 557, p. A71, 2013.

[98] R. J. Britto, E. Bottacini, B. Lott, S. Razzaque, and S. Buson, "Fermi-LAT Observations of the 2014 May-July Outburst from 3C 454.3," *The Astrophysical Journal*, vol. 830, p. 162, 2016.

[99] N. Sahakyan and S. Gasparyan, "High energy gamma-ray emission from PKS 1441+25," *Monthly Notices of the Royal Astronomical Society*, vol. 470, pp. 2861–2869, 2017.

[100] D. Zargaryan, S. Gasparyan, V. Baghmanyan, and N. Sahakyan, “Comparing 3C 120 jet emission at small and large scales,” *Astronomy & Astrophysics*, vol. 608, p. A37, 2017.

[101] V. Baghmanyan, S. Gasparyan, and N. Sahakyan, “Rapid Gamma-Ray Variability of NGC 1275,” *The Astrophysical Journal*, vol. 848, p. 111, 2017.

[102] S. Gasparyan, N. Sahakyan, V. Baghmanyan, and D. Zargaryan, “On the Multiwavelength Emission from CTA 102,” *The Astrophysical Journal*, vol. 863, p. 114, 2018.

[103] N. Sahakyan, V. Baghmanyan, and D. Zargaryan, “Fermi-LAT observation of nonblazar AGNs,” *Astronomy & Astrophysics*, vol. 614, p. A6, 2018.

[104] N. Sahakyan, “Modelling the broad-band emission of 3C 454.3,” *Monthly Notices of the Royal Astronomical Society*, vol. 504, pp. 5074–5086, 2021.

[105] N. Sahakyan, D. Israyelyan, G. Harutyunyan, S. Gasparyan, V. Vardanyan, and M. Khachatryan, “Modelling the time variable spectral energy distribution of the blazar CTA 102 from 2008 to 2022,” *Monthly Notices of the Royal Astronomical Society*, vol. 517, pp. 2757–2768, 2022.

[106] N. Sahakyan and P. Giommi, “A 13-yr-long broad-band view of BL Lac,” *Monthly Notices of the Royal Astronomical Society*, vol. 513, pp. 4645–4656, 2022.

[107] F. Aharonian *et al.*, “Simultaneous Observations of PKS 2155-304 with HESS, Fermi, RXTE, and Atom: Spectral Energy Distributions and Variability in a Low State,” *The Astrophysical Journal Letters*, vol. 696, pp. L150–L155, 2009.

[108] F. A. Harrison *et al.*, “The Nuclear Spectroscopic Telescope Array (NuSTAR) High-energy X-Ray Mission,” *The Astrophysical Journal*, vol. 770, p. 103, 2013.

[109] P. Giommi *et al.*, “X-ray spectra, light curves and SEDs of blazars frequently observed by Swift,” *Monthly Notices of the Royal Astronomical Society*, vol. 507, pp. 5690–5702, 2021.

[110] K. A. Arnaud, “XSPEC: The First Ten Years,” in *Astronomical Data Analysis Software and Systems V*, ser. Astronomical Society of the Pacific Conference Series, G. H. Jacoby and J. Barnes, Eds., vol. 101, Jan. 1996, p. 17.

[111] R. Middei *et al.*, “The first hard X-ray spectral catalogue of Blazars observed by NuSTAR,” *Monthly Notices of the Royal Astronomical Society*, vol. 514, pp. 3179–3190, 2022.

[112] W. Cash, “Parameter estimation in astronomy through application of the likelihood ratio.” *The Astrophysical Journal*, vol. 228, pp. 939–947, 1979.

[113] C. S. Kochanek *et al.*, "The All-Sky Automated Survey for Supernovae (ASAS-SN) Light Curve Server v1.0," *Publications of the Astronomical Society of the Pacific*, vol. 129, p. 104502, 2017.

[114] A. Mainzer *et al.*, "Preliminary Results from NEOWISE: An Enhancement to the Wide-field Infrared Survey Explorer for Solar System Science," *The Astrophysical Journal*, vol. 731, p. 53, 2011.

[115] E. Bonning *et al.*, "SMARTS Optical and Infrared Monitoring of 12 Gamma-Ray Bright Blazars," *The Astrophysical Journal*, vol. 756, p. 13, 2012.

[116] H. Abdalla *et al.*, "Simultaneous observations of the blazar PKS 2155-304 from ultra-violet to TeV energies," *Astronomy & Astrophysics*, vol. 639, p. A42, 2020.

[117] B. Schleicher *et al.*, "Fractional Variability—A Tool to Study Blazar Variability," *Galaxies*, vol. 7, p. 62, 2019.

[118] S. Gasparyan, D. Bégué, and N. Sahakyan, "Time-dependent lepto-hadronic modelling of the emission from blazar jets with SOPRANO: the case of TXS 0506 + 056, 3HSP J095507.9 + 355101, and 3C 279," *Monthly Notices of the Royal Astronomical Society*, vol. 509, pp. 2102–2121, 2022.

[119] M. Cerruti, W. Benbow, X. Chen, J. P. Dumm, L. F. Fortson, and K. Shahinyan, "Luminous and high-frequency peaked blazars: the origin of the γ-ray emission from PKS 1424+240," *Astronomy & Astrophysics*, vol. 606, p. A68, 2017.

[120] G. M. Madejski *et al.*, "First NuSTAR Observations of the BL Lac-type Blazar PKS 2155-304: Constraints on the Jet Content and Distribution of Radiating Particles," *The Astrophysical Journal*, vol. 831, p. 142, 2016.

[121] J. Aleksić *et al.*, "High zenith angle observations of PKS 2155-304 with the MAGIC-I telescope," *Astronomy & Astrophysics*, vol. 544, p. A75, 2012.

[122] N. Sahakyan, D. Bégué, P. Giommi, H. Dereli-Bégué, and A. Pe'er, "Impact of Spectral Coverage on Parameter recovery in Blazar Modeling," *arXiv e-prints*, p. arXiv:2511.20336, 2025.

[123] A. R. Bell, "The acceleration of cosmic rays in shock fronts - I." *Monthly Notices of the Royal Astronomical Society*, vol. 182, pp. 147–156, 1978.

[124] R. Blandford and D. Eichler, "Particle acceleration at astrophysical shocks: A theory of cosmic ray origin," *Physics Reports*, vol. 154, pp. 1–75, 1987.

[125] J. G. Kirk and P. Schneider, "On the Acceleration of Charged Particles at Relativistic Shock Fronts," *The Astrophysical Journal*, vol. 315, p. 425, 1987.

[126] D. C. Ellison, F. C. Jones, and S. P. Reynolds, "First-Order Fermi Particle

Acceleration by Relativistic Shocks," *The Astrophysical Journal*, vol. 360, p. 702, 1990.

[127] J. Bednarz and M. Ostrowski, "Energy Spectra of Cosmic Rays Accelerated at Ultrarelativistic Shock Waves," *Physical Review Letters*, vol. 80, pp. 3911–3914, 1998.

[128] D. C. Ellison and G. P. Double, "Diffusive shock acceleration in unmodified relativistic, oblique shocks," *Astroparticle Physics*, vol. 22, pp. 323–338, 2004.

[129] D. Giannios, "Reconnection-driven plasmoids in blazars: fast flares on a slow envelope," *Monthly Notices of the Royal Astronomical Society*, vol. 431, pp. 355–363, 2013.

[130] M. Lyutikov and D. Uzdensky, "Dynamics of Relativistic Reconnection," *The Astrophysical Journal*, vol. 589, pp. 893–901, 2003.

[131] Y. E. Lyubarsky, "On the relativistic magnetic reconnection," *Monthly Notices of the Royal Astronomical Society*, vol. 358, pp. 113–119, 2005.

[132] D. Giannios, D. A. Uzdensky, and M. C. Begelman, "Fast TeV variability in blazars: jets in a jet," *Monthly Notices of the Royal Astronomical Society*, vol. 395, pp. L29–L33, 2009.

[133] M. Petropoulou, D. Giannios, and L. Sironi, "Blazar flares powered by plasmoids in relativistic reconnection," *Monthly Notices of the Royal Astronomical Society*, vol. 462, pp. 3325–3343, 2016.

[134] R. S. Nemmen, M. Georganopoulos, S. Guiriec, E. T. Meyer, N. Gehrels, and R. M. Sambruna, "A Universal Scaling for the Energetics of Relativistic Jets from Black Hole Systems," *Science*, vol. 338, p. 1445, 2012.

[135] G. Ghisellini, F. Tavecchio, L. Maraschi, A. Celotti, and T. Sbarrato, "The power of relativistic jets is larger than the luminosity of their accretion disks," *Nature*, vol. 515, pp. 376–378, 2014.

[136] M. L. Ahnen *et al.*, "Very High Energy γ-Rays from the Universe's Middle Age: Detection of the z = 0.940 Blazar PKS 1441+25 with MAGIC," *The Astrophysical Journal Letters*, vol. 815, p. L23, 2015.

[137] A. U. Abeysekara *et al.*, "Gamma-Rays from the Quasar PKS 1441+25: Story of an Escape," *The Astrophysical Journal Letters*, vol. 815, p. L22, 2015.

[138] J. R. Mattox *et al.*, "The Likelihood Analysis of EGRET Data," *The Astrophysical Journal*, vol. 461, p. 396, 1996.

[139] P. W. A. Roming *et al.*, "The Swift Ultra-Violet/Optical Telescope," *Space Science*

Reviews, vol. 120, pp. 95–142, 2005.

[140] T. S. Poole *et al.*, "Photometric calibration of the Swift ultraviolet/optical telescope," *Monthly Notices of the Royal Astronomical Society*, vol. 383, pp. 627–645, 2008.

[141] E. C. Bellm *et al.*, "The Zwicky Transient Facility: System Overview, Performance, and First Results," *Publications of the Astronomical Society of the Pacific*, vol. 131, p. 018002, 2019.

[142] N. Kaiser *et al.*, "Pan-STARRS: A Large Synoptic Survey Telescope Array," in *Survey and Other Telescope Technologies and Discoveries*, ser. Society of Photo-Optical Instrumentation Engineers (SPIE) Conference Series, J. A. Tyson and S. Wolff, Eds., vol. 4836, Dec. 2002, pp. 154–164, doi: 10.1117/12.457365.

[143] P. Giommi, N. Sahakyan, D. Israyelyan, and M. Manvelyan, "The Remarkable Predictive Power of Infrared Data of Blazars," *The Astrophysical Journal*, vol. 963, p. 48, 2024.

[144] N. I. Shakura and R. A. Sunyaev, "Reprint of 1973A&A....24..337S. Black holes in binary systems. Observational appearance." *Astronomy & Astrophysics*, vol. 500, pp. 33–51, 1973.